Contact Point and Object Position from Force/Torque and Position Sensors for Grasps with a Dextrous Robotic Hand

Dipl.-Ing. Steffen Haidacher, M.S.
Deutsches Zentrum für Luft- und Raumfahrt
Institut für Robotik und Mechatronik

Technische Universität München
Lehrstuhl für Realzeit-Computersysteme

Deutsches Zentrum für Luft- und Raumfahrt
Institut für Robotik und Mechatronik

Contact Point and Object Position from Force/Torque and Position Sensors for Grasps with a Dextrous Robotic Hand

Dipl.-Ing.Univ. Steffen Haidacher, M.S.

Vollständiger Abdruck der von der Fakultät für Elektrotechnik und Informationstechnik der Technischen Universität München zur Erlangung des akademischen Grades eines

Doktor-Ingenieurs (Dr.-Ing.)

genehmigten Dissertation.

Vorsitzender:	Univ.-Prof. Dr.-Ing./Univ. Tokio Martin Buss
Prüfer der Dissertation:	
	1. Hon.-Prof. Dr.-Ing. Gerd Hirzinger
	2. Univ.-Prof. Dr.-Ing. Georg Färber

Die Dissertation wurde am 21.1.2004 bei der Technischen Universität München eingereicht und durch die Fakultät für Elektrotechnik und Informationstechnik am 25.6.2004 angenommen.

Acknowledgment

This thesis summarizes some of the results of my work as research associate at the Institute of Robotics and Mechatronics at the German Aerospace Center (DLR) in Oberpfaffenhofen near Munich. I would like to thank all people, advisors, colleagues, students and friends, who supported me during the last four and a half years and helped to make this research successful.

In particular I want to thank Prof. Dr.-Ing Gerd Hirzinger for providing me with the unique opportunity to work at his institute. His laboratory supplies both, best qualified personnel and all required technical equipment for a fruitful, sophisticated research. I was always granted freedom and support for my work. I also want to express my appreciation for Prof. Dr.-Ing Georg Färber for his advise and guidance during the composition of this thesis. He also enabled me to participate in most interesting discussions about ongoing research at his institute.

I would like to thank my fellow researchers, whom I had the great opportunity to discuss various matters of research with. Those discussions served to enlarge my scientific horizon and also helped to develop, implement and experimentally evaluate the algorithms presented in this thesis. In particular I want to thank Udo Frese, for sharing his insight into Kalman filters and statistical methods and for critically proofreading this thesis. I also want to thank both people, I had the pleasure to share an office and precious ideas with, Wolfgang Sepp and Martin Hörmann. I further like to acknowledge the scientific and technical guidance of Dr. Max Fischer.

For the possibility to perform experiments with DLR Hand II and for the technical assistance hereby I would like to say thank you to Markus Grebenstein, Klaus Jöhl and Dr. Jörg Butterfaß. For providing me with models of objects by laser scan I would like to thank Tim Bodenmüller. I also want to thank all those people who poof-read this thesis.

Last but not least I want to thank my parents who promoted my ongoing education and helped to overcome any obstacle. A special, warm thank you is for Sylvia, who encouraged and supported me especially during the last months of long and late work to finish the writing.

Steffen Haidacher Weßling, December 2003

Contents

List of Figures

List of Tables

List of Symbols

Symbols are ordered by their context and location of first appearance (number of chapter in braces).

General Symbols

n	number of fingers in the hand	(2.2.2)
i, j	indices for selected fingers, $i, j \in [1, n]$	(2.2.2)
$r; s; t;$ $a; b; c$	general variables	(2.2.3)

Coordinate Frames and Transformations

$S^{(f,i)}$	coordinate frame fixed to the reference in finger tip i	(2.2.2)
$S^{(w)}$	world reference frame	(2.2.2)
$S^{(o)}$	coordinate frame fixed to a grasped object	(2.2.2)
$S^{(fc,i)}$	moving coordinate frame at contact of finger tip i	(2.2.2)
$S^{(oc,i)}$	moving coordinate frame at contact of object with finger i	(2.2.2)
$S^{(t)}$	coordinate frame attached to the finger tip sensor	(3.2.1)
$S^{(j,s)}$	coordinate frame at the joint sensor in joint s	(3.2.1)
$S^{(v)}_{r,k}$	2D coordinate system in vertex r of facet k	(4.1.1)
$\boldsymbol{T}^{(f,i)}_{(w)}$	homogeneous transform from $S^{(f,i)}$ of finger i to $S^{(w)}$	(2.2.2)
$\boldsymbol{T}^{(fc,i)}_{(f,i)}$	homogeneous transform from $S^{(fc,i)}$ of finger i to $S^{(f,i)}$	(2.2.2)
$\boldsymbol{R}^{(fc,i)}_{(f,i)}$	rotation from $S^{(fc,i)}$ of finger i to $S^{(f,i)}$	(3.2.1)
$\vec{t}^{\,(fc,i)}_{(f,i)}$	translation from $S^{(fc,i)}$ of finger i to $S^{(f,i)}$	(3.2.1)
$\boldsymbol{T}^{(oc,i)}_{(o)}$	homogeneous transform from $S^{(oc,i)}$ of object contact i to $S^{(o)}$	(2.2.2)
$\boldsymbol{T}^{(oc,i)}_{(fc,i)}$	homogeneous transform between $S^{(oc,i)}$ and $S^{(fc,i)}$ at contact i	(2.2.2)
$\boldsymbol{T}^{(fc)}_{(t)}$	homogeneous transform from $S^{(fc)}$ to $S^{(t)}$	(3.2.1)
$\boldsymbol{R}^{(fc)}_{(t)}$	rotation from $S^{(fc)}$ to $S^{(t)}$	(3.2.1)
$\vec{t}^{\,(fc)}_{(t)}$	translation from $S^{(fc)}$ to $S^{(t)}$	(3.2.1)

$\boldsymbol{T}_{(t)}^{(f)}$	homogeneous transform from $S^{(f)}$ to $S^{(t)}$	(3.2.1)
$\boldsymbol{T}_{(j,s)}^{(f)}$	homogeneous transform from $S^{(f)}$ to $S^{(j,s)}$	(3.2.1)
$\boldsymbol{T}_{(o)}^{(w)}$	homogeneous transformation from $S^{(w)}$ to $S^{(o)}$	(4.2.3)
$\boldsymbol{R}_{(o)}^{(w)}$	rotation from $S^{(w)}$ to $S^{(o)}$	(4.2.3)
$\vec{t}_{(o)}^{(w)}$	translation from $S^{(w)}$ to $S^{(o)}$	(4.2.3)

Symbols used in General Model of Contact

$\vec{x}_{f,i}$	position of the reference, usually tip, of finger i	(2.2.2)
$\vec{\varrho}_{f,i}$	orientation of finger tip i	(2.2.2)
$\vec{\theta}_i$	joint angles of finger i	(2.2.2)
$\vec{f}_{x,i}(\vec{\theta}_i)$	kinematic description of the position of finger i	(2.2.2)
$\vec{g}_{\varrho,i}(\vec{\theta}_i)$	kinematic description of the orientation of finger i	(2.2.2)
$\delta\vec{\theta}_i$	infinitesimal joint motion of finger i	(2.2.2)
$\delta\vec{x}_{f,i}$	infinitesimal change in position at finger tip i	(2.2.2)
$\delta\vec{\varrho}_{f,i}$	infinitesimal change in orientation at finger tip i	(2.2.2)
$\dot{\vec{\theta}}_i$	joint velocity of finger i	(2.2.2)
$\dot{\vec{x}}_{f,i}$	translational velocity of finger tip i	(2.2.2)
$\dot{\vec{\varrho}}_{f,i}$	rotational velocity of finger tip i	(2.2.2)
$\boldsymbol{J}_{x,i}$	Jacobian between $\vec{\theta}_i$ and tip position $\vec{x}_{f,i}$ of finger i	(2.2.2)
$\boldsymbol{J}_{\varrho,i}$	Jacobian between $\vec{\theta}_i$ and tip orientation $\vec{\varrho}_{f,i}$ of finger i	(2.2.2)
$\vec{\nu}_{f,i}$	generalized velocity of finger i	(2.2.2)
$\boldsymbol{J}_{f,i}$	generalized Jacobian of finger i	(2.2.2)
$\vec{f}_{fc,i}(\vec{u}_{f,i})$	surface description of the finger tip i	(2.2.2)
$\vec{f}_{oc,i}(\vec{u}_{o,i})$	surface description of the object at finger tip i	(2.2.2)
$\vec{u}_{f,i}$	parameter vector of the surface of finger i	(2.2.2)
$\vec{u}_{o,i}$	parameter vector of the surface of the object at finger i	(2.2.2)
$\vec{x}_{fc,i}$	contact between finger i and object at finger i	(2.2.2)
$\vec{x}_{oc,i}$	contact between finger i and object at object	(2.2.2)
$\vec{n}_{fc,i}$	surface normal at $\vec{x}_{fc,i}$ as seen from finger i	(2.2.2)
$\vec{n}_{oc,i}$	surface normal at $\vec{x}_{oc,i}$ as seen from the object	(2.2.2)
$\vec{e}_{x,\diamond,i}$	basis vector of $S_{\diamond,i}$ with $\diamond \in \{fc, oc\}$	(2.2.2)
$\vec{e}_{y,\diamond,i}$	basis vector of $S_{\diamond,i}$ with $\diamond \in \{fc, oc\}$	(2.2.2)
$\vec{e}_{z,\diamond,i}$	basis vector of $S_{\diamond,i}$ with $\diamond \in \{fc, oc\}$	(2.2.2)
$O^{(\diamond)}$	origin of the contact system $S_{\diamond,i}$	(2.2.2)
ψ_i	angle of torsion around $\vec{e}_{z,\diamond}$ between $\vec{e}_{x,fc,i}$ and $\vec{e}_{x,oc,i}$	(2.2.2)
$\vec{\nu}_{c,i}$	generalized velocity of contact point at finger i	(2.2.2)
$\vec{\nu}_o$	generalized velocity of object	(2.2.2)

$\boldsymbol{J}_{c,i}$	generalized contact Jacobian at finger i	(2.2.2)
$\vec{u}_i$	parameters of contact at finger i	(2.2.2)
$\beta_2(\boldsymbol{T}_{(A)}^{(B)})$	adjoint transformation for general. velocities from B to A	(2.2.2)
$*$	Hodge operator, vector cross product in matrix form	(2.2.2)

Symbols used in Contact Detection

$\vec{f}_c$	contact force at the contact point $\vec{x}_c$	(3.2)
τ_c	contact torque at the contact point $\vec{x}_c$	(3.2)
r	number of joints in a robot	(3.2)
s	index of one particular joint	(3.2)
τ_s	joint torque at the joint s	(3.2)
$\vec{f}_t$	force measured at a finger tip sensor	(3.2)
$\vec{\tau}_t$	torque measured at a finger tip sensor	(3.2)
$\vec{\tau}_f$	vector of all joint torques	(3.2)
$\vec{y}$	vector of measurements	(3.2.1)
$\hat{\vec{y}}$	vector of expected measurements	(3.2.1)
ς	merit function for intrinsic contact point detection	(3.2.1)
$\boldsymbol{C}_\varsigma$	measurement covariance of $\vec{y}$	(3.2.1)
$\boldsymbol{J}_{u,i}(\vec{u}_i)$	contact joint Jacobian of finger i	(3.1.1)
$\dot{\vec{u}}_i$	contact joint velocity of finger i	(3.1.1)
$v_{x,i}; v_{y,i};$ $v_{z,i}; \omega_{x,i};$ $\omega_{y,i}; \omega_{z,i}$	components of $\vec{\nu}_{c,i}$	(3.1.1)
g	number of contact constraints	(3.1.1)
$\vec{\nu}_{c,h}$	stacked hand contact velocity	(3.1.2)
$\vec{\theta}_h$	stacked hand joint angles	(3.1.2)
$\dot{\vec{\theta}}_h$	stacked hand joint velocities	(3.1.2)
$\vec{u}_{f,h}$	stacked hand contact joint angles	(3.1.2)
$\boldsymbol{J}_{f,h}$	combined hand Jacobian	(3.1.2)
$\boldsymbol{J}_{c,h}$	combined hand contact Jacobian	(3.1.2)
$\Delta\vec{\nu}_{f,h}$	relative finger tip velocity	(3.1.2)
$\tilde{\vec{v}}_{c,h}$	constrained contact velocity	(3.1.2)
$\tilde{\boldsymbol{J}}_{c,h}$	constrained contact Jacobian	(3.1.2)
$\Gamma(\vec{u}_{f,h})$	mapping from $\mathcal{C}$ to $\mathcal{F}$	(3.1.3)
$\mathcal{C}$	space of reduced contact velocities $\tilde{\vec{v}}_{c,h}$	(3.1.3)
$\mathcal{F}$	space of relative finger velocities $\Delta\vec{v}_{f,h}$	(3.1.3)
$\mathcal{R}$	range space of Γ	(3.1.3)
$\mathcal{L}$	left null space of Γ	(3.1.3)

$\tilde{\boldsymbol{J}}^{+}_{c,h}$	left pseudo-inverse of $\tilde{\boldsymbol{J}}_{c,h}$	(3.1.3)
$\hat{\vec{u}}_{f,h}$	estimate for $\vec{u}_{f,h}$	(3.1.3)
$\hat{\vec{\nu}}_{c,h}$	estimate for $\vec{\tilde{\nu}}_{c,h}$	(3.1.3)
$\vec{\eta}_{f,h}$	error vector in estimate of $\hat{\vec{u}}_{f,h}$	(3.1.3)
ξ_1	scalar error in estimate for one measurement	(3.1.3)
ξ_m	scalar error in estimate for m measurements	(3.1.3)
$\boldsymbol{Q}$	set of vectors	(3.1.3)
$\vec{q}$	vector of set $\boldsymbol{Q}$	(3.1.3)
$\hat{\vec{u}}_{f,h}(t)$	extrapolated estimate in observer	(3.1.4)
χ	merit function for information filter	(3.1.4)
$\boldsymbol{C}_m$	measurement covariance matrix	(3.1.4)
$\boldsymbol{C}_s$	system covariance matrix	(3.1.4)
$\boldsymbol{C}_z$	state covariance matrix	(3.1.4)
$\boldsymbol{S}$	selection matrix	(3.1.4)
$\boldsymbol{M}_{f,i}$	metric matrix of the finger tip i	(3.1.4)
$\boldsymbol{K}_{f,i}$	curvature matrix of the finger tip i	(3.1.4)

Symbols used in Detection of Object Pose

m	total number of facets in model object	(4.1.1)
k, l	indices for selected facets; $k, l \in [1, m]$	(4.1.1)
$\vec{x}^{(o)}_{1,k}$; $\vec{x}^{(o)}_{2,k}$; $\vec{x}^{(o)}_{3,k}$	first, second and third vertex of selected facet k	(4.1.1)
$\vec{p}_{oc,k}$	oriented point of contact at facet k	(4.1.1)
$\vec{x}_{oc,k}$	reference position of facet k	(4.1.1)
$\vec{n}_{oc,k}$	surface normal of facet k	(4.1.1)
$d^{(o)}_{oc,k}$	distance of facet k to $S^{(o)}$	(4.1.1)
$\vec{x}$	arbitrary point	(4.1.1)
$\mathcal{F}_{oc}$	set of size n of estimated oriented points	(4.1.1)
$e\vec{p}^{(o)}_{r,k}$	direction of edge r of facet k	(4.1.1)
$e\vec{n}^{(o)}_{r,k}$	normal vector to $e\vec{p}^{(o)}_{r,k}$	(4.1.1)
$l_{r,k}$	length of edge r of facet k	(4.1.1)
$\vec{p}_{fc,i}$	measured oriented point of contact at finger i	(4.1.2)
$\vec{x}_{fc,i}$	measured contact point at finger i	(4.1.2)
$\vec{n}_{fc,i}$	measured contact normal at finger i	(4.1.2)
$d^{(w)}_{fc,i}$	distance of the $\vec{x}_{fc,i}$ to $S^{(w)}$	(4.1.2)

$\mathcal{F}_{fc}$	set of size n of measured oriented points	(4.1.2)
$\Delta_{fc,ij}$	rel. distance between $\vec{p}_{fc,i}$ and $\vec{p}_{fc,j}$	(4.2.1)
$\alpha_{fc,ij}$	rel. angle between $\vec{p}_{fc,i}$ and $\vec{p}_{fc,j}$	(4.2.1)
Ω_{fc}	orientation of sorted measured oriented points	(4.2.1)
ε	number of bytes to store a value in memory	(4.2.2)
F_1	1D list of data of m facets	(4.2.2)
P_2	1D list of $1/2(m^2+m)$ geom. facet relations	(4.2.2)
$\Delta_{min,oc,kl}$	min. distance between two facets k and l	(4.2.2)
$\Delta_{max,oc,kl}$	min. distance between two facets k and l	(4.2.2)
$\alpha_{oc,kl}$	relative angle between facets k and l	(4.2.2)
H_2	3D hash table of facet pairs	(4.2.2)
$\diamond$	element of set $\{\Delta_{min,oc}, \Delta_{max,oc}, \alpha_{oc}\}$	(4.2.2)
$p_\diamond$	number of bins for H_2 on axis $\diamond$	(4.2.2)
$q_\diamond$	width on dimension $\diamond$ of a bin of H_2	(4.2.2)
$Max_\diamond$	maximum of $\diamond$ over all facet pairs	(4.2.2)
$Min_\diamond$	minimum of $\diamond$ over all facet pairs	(4.2.2)
$t_1(\Delta_{max,kl})$	maximum coordinate to a bin of H_2	(4.2.2)
$t_2(\Delta_{min,kl})$	minimum coordinate to a bin of H_2	(4.2.2)
$t_3(\alpha_{kl})$	angle coordinate to a bin of H_2	(4.2.2)
$A_{2,ij}$	lists of admissible facet pairs	(4.2.2)
$R_{1,i}$	list of admissible facets for finger i	(4.2.2)
$\sigma_\diamond$	measurement uncertainty	(4.2.2)
T_n	tree storing possible facet combinations	(4.2.2)
k_1; k_2; ... k_n	indices for selected facets; $k_1, k_2, ...k_n \in [1, m]$	(4.2.2)
$\vec{h}$	valid hypotheses for facets	(4.2.2)
$\bar{A}_{2,ij}(k,l)$	array of bools for admissible facets (k,l)	(4.2.2)
$\chi^2_a(\vec{\theta}, \vec{t}, \vec{h}_a)$	merit function for test of the pairing a of a hypothesis $\vec{h}_a$	(4.2.3)
$\chi^2(\vec{\theta}, \vec{t}, \vec{h})$	merit function for test of all pairings of a hypothesis $\vec{h}$	(4.2.3)
$\chi^2_{a,1}, \chi^2_{a,2}, \chi^2_{a,3}$	partial merit functions	(4.2.3)
$\boldsymbol{W}_1$, W_2, W_3	weights on individual terms of χ^2	(4.2.3)
$(\lambda_{r,k}, \kappa_{r,k})$	2D corner coordinates of $\vec{x}^{(w)}_{fc,i}$	(4.2.3)
P	probability of obtaining a measurement $\mathcal{F}_{fc}$	(4.2.4)
$\tilde{P}$	likelihood of obtaining a measurement $\mathcal{F}_{fc}$	(4.4.1)
d	cumulative facet distance	(4.4.1)

Abstract

In the last few years, numerous complex dextrous robotic hands have been developed. They are now employed as manipulators in larger robotic systems in various fields of activity as for example *tele-operation* and *service robotics*. So far, research on these robotic hands was solely occupied with isolated laboratory systems. Only recently, triggered by the increasing capabilities of the hardware, real world tasks have been implemented. In doing so, it was found that most algorithms for planning and smooth control of robotic grasping require more information than was generally available from actual measurements: The exact point of contact between an object to be grasped and the surface of a finger, and the position of the object.

Due to the lack of small but nevertheless high resolution tactile sensors, the contact point is not directly measurable in the vast majority of robotic grippers. The information can nevertheless be retrieved, using and interpreting other sensors. Two new approaches to this interpretation are presented in this work. The first method evaluates position sensors. It exploits kinematic velocity constraints imposed on the motion of fingers and an object through rigid or quasi-rigid contact. It is able to obtain the contact points on the surface of the finger and the relative motion between the fingers and the object. The second method estimates the position of contact and the respective forces at this point from the force / torque measurements available at a finger.

Based on the contact information, this work strives to determine the position of the object itself: The thesis at hand proposes an optimised algorithm to compare the derived information about the point of contact with a geometric model of the object. Thereby, the object can be located. This is especially required if other, e.g. visual information, is either not available or unreliable as may be the case due to obstruction of vision by other objects or infeasible lighting conditions. This algorithm implements a “blind man’s” approach to grasping.

The proposed methods are evaluated in computer simulations and experimentally verified using the DLR Hand II.

Chapter 1

Introduction

More than one and a half centuries ago, science fiction authors created the vision of machines that readily help men as their personal assistants at work and at home, like a human servant would do. At the same time, this idea also pushed engineers, who ambitiously worked to make these robots reality. For twenty years now, in the technical world of industry, these visions have come true: Specialised machines are performing tedious jobs rendering manual labour easier. The widespread visions of robots assisting in every day's life, however, poses more problems, which have challenged researchers:

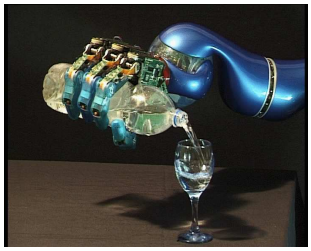

Figure 1.1: Robot butler

In contrast to industrial machines, a robot that is intended to act in a normal human environment cannot be specially prepared for the requirements of one single task nor is it desirable to adjust the workspace of the robot to its particular needs. Instead, it is expected that the robot is flexible enough to adjust to the actual requirements of a task. Obviously, man can work in its environment very well: most objects here have either been particularly designed for convenient use, or man has developed special skills for their use in its evolution. Therefore, it is not surprising that, in order to develop a universal robot, the abilities of humans have been imitated by anthropomorphic designs (e.g., figure 1.1). Just to mention a few of these recently developed capabilities: For maneuvering in general environments, robot bodies were equipped with legs [LGP02]. For performing actions, arms and hands were built [HSA+02, BGLH01] and for robot-human interaction, artificial faces were studied [BS99]. Even complete humanoids were developed [Hon03].

Through the development of sophisticated, anthropomorphic robotic hardware, on the way to a visionary robot servant, more applications became possible. By the way the robot is commanded, these real world tasks can be divided into two

groups. On one hand, anthropomorphic robots can be intuitively *tele-operated*: A human operator uses the robot to extend his capabilities or to reach for places such as hazardous environments which were previously not suitable for direct human deployment. In this mode, anthropomorphic or partially anthropomorphic robots are already in practical use. On the other hand, an anthropomorphic robot can be operated *autonomously*. The robot receives colloquial orders. It autonomously decomposes these orders to individual tasks and afterwards fulfills the desired work without any further human intervention. This, so far, is still a promising topic of intense research and only few commercially usable applications of simple complexity have made their way to market, for example machines that independently clean railway platforms or cut grass.

Figure 1.2: X-ray image of a human hand

Leaving the large field of anthropomorphic robots, this thesis concentrates on a specific subsystem of particular interest, the hand. Generally speaking, the duty of humanoid robots is to explore or manipulate the environment. Man himself uses his hand (e.g., figure 1.2) for this aim, which in most cases seems to be an appropriate tool. The human hand is, after the face, that region of the body which is most sensitive. It can perfectly be used to examine objects of interest. Besides, with its 27 bones and 20 muscles it is able to perform complex motions and is therefore well adapted to subtly manipulate objects. It is hence no surprise that in their desire to construct an anthropomorphic robot, researchers particularly directed their interest to the development of so called “dextrous robotic hands”. For robots, these hands are the most flexible tools to interact with the human environment, just as man does.

1.1 Motivation

In recent years, those robotic grippers were improved from early parallel jaw grippers and special tools (e.g., figure 1.3) to highly complex, sensitive, anthropomorphic hands (e.g., figure 1.4). This development significantly increased the capabilities of the grippers. The door was opened for applications beyond well prepared setups of industrial applications or laboratories.

The improvement in robotic hands also allowed increasingly complex applications to be addressed. Two important tasks of robotic hands are the exploration and manipulation of the environment. Methodical approaches were developed for both. Exploration, on the one hand, usually consists of a motion along the surface

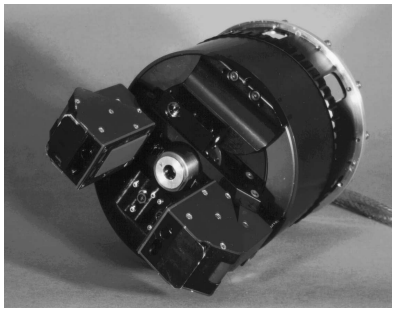

Figure 1.3: Parallel jaw gripper at DLR

Figure 1.4: Highly sophisticated gripper: DLR Hand II

of the object, during which particular information, such as its geometry, coarseness and stiffness, is collected. On the other hand, manipulation of an object first requires to pick the object up and hold, hence grasp it. Technically, grasping an object requires to exert forces on an object while the grasping forces at the points of contact have to be balanced. This necessity can particularly be seen in delicate grasps such as that of a wet soap. Afterwards, in order to manipulate and hence move an object in the hand, appropriate motions of the fingers have to be determined. The knowledge of contact points and orientation of the surface is necessary for proper execution. The most important information in algorithms for robotic exploration and manipulation are hence the geometric properties of the contact between the fingers and the object. In most cases, this is the location of the contact and the direction orthogonal to the contact surface, the surface normal.

When performing simplified experiments, actual determination of these so called *contact parameters* (see figure 1.5) can be avoided by a special preparation of the experiment or heuristic assumptions. Yet, for more complex experiments or in real world applications, objects usually have to be grasped in a previously unknown position. Thus, a particular preparation is impractical.

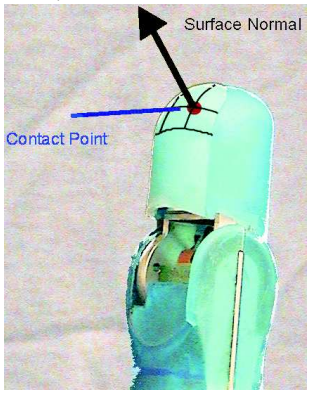

Figure 1.5: Contact point and surface normal

One remedy to this problem is the use of tactile sensors. However, these sensors are not yet available in appropriate dimensions while still having reasonable resolution. Also, most of those sensors are still experimental and not reliable enough for long time applications. They require additional instrumentation at the robotic hand which increases the effort for design and assembly of a hand of reasonable size and weight. Further, problems with tactile sensors occur at highly bent surfaces as for example the finger tip. The majority of available tactile sen-

sors have been designed for only moderately curved surfaces. In most cases, thus, another way to determine the contact parameters is desirable.

Further, when grasping an object, not only the geometric contact parameters are required but also the exact position of the object. This is particularly the case, when other a-priori information about the object such as the object's shape or its weight distribution is to be taken into account in the course of its handling.

In laboratory experiments, localisation can be avoided by setting the object onto a pre-determined position. In complex setups this is obviously not reasonable. The position of the object then has to be determined by means of computer vision. This, however, has its own drawbacks: During grasping, objects may shift or be obstructed from vision particularly in the last phase. Exact relative calibration between the camera system and the grasping system is required in order to relate the object position from vision to the issued motion commands for the fingers. Also, environment conditions such as lighting may disturb localisation by vision. All this may be a significant source of error in the detection of the object's true position. Thus, another localisation method using different sensors can assist vision in the late phase of grasping immediately after contacting the object. This method can verify and improve the localisation from vision.

1.2 Goals of this Work

This work addresses both mentioned problems, first the determination of contact parameters and second the localisation of an object by hand perceptions.

At first, for the indirect determination of the contact parameters, two methods are proposed, which use common sensors in robotic hands in a new way: A first algorithm computes the contact points of the fingers from the constrained motion of multiple fingers when they cooperatively grasp and move an object: The fingers have to maintain stable contact and are hence restricted in their mobility. The possible motions of the fingers depend on the points of contact. Consequently, from measured motions of the fingers, the point of contact can be estimated. This algorithm requires velocity sensors, or where those are not available position sensors may be used and the numerical derivative has to be computed. Those sensors are required for basic motion control of a robot and are thus always available. This algorithm is hence particularly applicable for simple grippers. The method requires multiple fingers in contact with an object. For the application of the algorithm, the object has to move during examination. The joint position sensors, used to determine the contact parameters, are not directly correlated with the location of the event, namely the contact between finger and object. Hence, this method of sensation is called *exteroceptive*, in contrast to *proprioceptive* sensations, that are colocated with the place of the perception, e.g., tactile sensing.

For delicate control, in most hands force/torque sensors are present. With these sensors, this thesis also proposes an algorithm to determine the location of contact along with the forces and torques acting at that point. The number of required sensors depends on the assumption in what directions forces and torques can be applied at the contact. Unlike the first method, this algorithm works on individual fingers. It is thus usable in the initial stage of grasping, when all fingers are moved separately to the surface of the object. In contrast to other work, this proposal does not require any particular sensor positioning and can be adjusted to different models of contact and is thus more widely usable. The determination of the contact parameters through the evaluation of force/torque sensors is called *intrinsic* in literature, in contrast to a direct measurement through tactile sensors.

When the geometry of the finger tip is known from design, which is usually the case, with the position of contact also the surface normal can be derived. Hence, both algorithms deliver point of contact and surface normal as results.

To tackle the problem of object localisation, this work also presents an algorithm to compare contact parameters obtained from either a tactile measurement or algorithms as proposed above to a given object model. This allows quick determination of the object's position. The proposed method enables a robust transition of an object localisation from external sensors to a localisation from sensors included in the hand: First, the object is globally located by computer vision. After contacting the object, its position can be determined from those position or force/torque sensors which are also employed for control of the hand. Hence no relative calibration errors occur. This algorithm is comparable to a human, which can still grasp an object although concentrating on other things and hence have only a general idea of its position. Global localisation is done by vision, human or machine, respectively. Local information about an object's position is obtained by the tactile human sense or the algorithm presented here.

As an experiment for the algorithms presented here, the DLR Hand II will grasp an unknown object: The object is given to the hand, which will slowly close. After all fingers have made contact, the object is moved in the hand with all fingers and the contact points can be determined using the proposed algorithm. The location of the object is determined using the methods of the thesis at hand and a three-dimensional model obtained from a laser range scanner. The evolution of the contact point is also observed during the motion of the object.

1.3 Summary of the Proposed Algorithms

The technical ideas for the location of contact between the fingers and an object are twofold. First, when two objects touch each other, this contact imposes constraints on their relative motion. Mathematical models of contact have been

established and can be used to describe these constraints of motion. A hand with several fingers contacts an object in several locations simultaneously. The motion of all fingers can be detected using position sensors usually available in robotic hands. Observing several directions of motion constitutes an over-determined system of equations. Using a least squares approach allows those contact points at the fingers to be found that best match the measurements of motion and the constraints of mobility through contact. Instead of directly using least squares methods, also an information filter, dual to a Kalman Filter, is proposed.

The location of contact can also be determined from a measurement of forces and torques. Forces and torques applied at the contact point can be related to those forces and torques measured in sensors. Physical models of the transmission of forces and torques at the contact exist. The relation between transmitted and measured forces/torques can be formulated in so called measurement equations and evaluated in a least squares approach to determine the point of contact.

Also, when several fingers contact an object, the above computed locations of contact and the inherently obtained normals to the fingers' surfaces can be compared to a geometrical model of the surface of an object. Numerous possibilities to describe the surface are available. An approximation with polygons will be chosen later. An efficient method to select those polygons where the fingers possibly contact is developed. Using a least squares approach, the location of the object can be found that best matches these isolated surface patches.

1.4 Organisation of this Work

This work is organised as follows:

Chapter 2 is divided into two main sections: In section 2.1, the reader is introduced to representative developments in robotic hands and sensors. A short overview of complete applications and the algorithmic components of these applications is presented. Also, some fundamental research about the theory of contact and grasping is revisited. Finally, work related to the ideas pursued here, detection of the contact point and location of the object, is reviewed. In section 2.2 some methodical background is explained, which is required for the understanding of the technical chapters of this thesis.

Chapter 3 is also divided into two sections, each of them introducing one algorithm to detect the point of contact at the finger surface. In section 3.1, a method is introduced to detect the point of contact from the kinematically constrained motion of fingers in touch with an object. This section concludes with a numerical analysis of the algorithm. In section 3.2, an algorithm is proposed to detect the position of contact on the finger tip's surface from force/torque measurements. An extensive discussion and numerical results follow.

In chapter 4, a way is developed to tactilely determine the position of an object. The approach can be interpreted as maximum likelihood estimate. Hence, a statistical analysis and further numerical examination is performed.

In chapter 5, the experimental setup of the DLR Hand II is introduced. The practical performance of the previously presented algorithms is verified using this hand.

Chapter 6 summarises the results of this work and shows ideas of further research.

Chapter 2

State of the Art

As an introduction to the authors own work presented in subsequent chapters, this chapter guides the reader through the basics of manipulation with a dextrous robotic hand. In the first part, in section 2.1, a general overview of existing work is given. The second part, section 2.2, introduces in detail some technical background from literature, which is required for the understanding of theory presented in later chapters.

In order to familiarise the reader with the achievements of research on the design of dextrous robotic hands, major developments in this area are introduced in section 2.1.1. Since this thesis is based on intelligent interpretation of sensor measurements, section 2.1.2 briefly reviews commonly used sensors in robotic hands. With the given hardware, a large number of possible applications for robotic hands were studied. Some of them already reached maturity for commercial applications, some of them are still experimental. Along with the applications, sub-algorithms for their implementation evolved. These sub-algorithms need data, for example the location of a grasped object, the point of contact between a finger and a grasped object and the surface normal at the contact point, which this thesis delivers from standard sensors by new algorithms. In order to point out this necessity, some representative highlights of applications and algorithms are revisited in section 2.1.3. For a thorough understanding of the physics during grasping, models were developed which describe the observed phenomena. At first, when one object touches another, a so-called contact occurs. Individual contacts between two objects were examined. Section 2.1.4 revisits some major models of contact which are able to mathematically describe most of the observations encountered during robotic grasping. After an understanding of individual contacts was achieved, the interaction of multiple contacts with several fingers and possibly the palm of the gripper was studied. Here, two areas of research evolved. On the one hand the position of the individual contact points at the object were studied. These contact points determine, whether an object can stably be grasped

or escapes the gripper like a bar of wet soap. On the other hand, the geometry of the hand during grasping was studied. The posture of the hand has effects on the number, location and type of contact points and is hence also of importance for the stability of this grasp. Both points are described in section 2.1.5. This work was motivated by the need to determine the contact parameters, e.g. point of contact and surface normal, from methods other than tactile. A review of work done either to obtain only these parameters or more generally to explore an object is given in section 2.1.6. Several applications for robotic hands, which will be revisited, are model-based. Hence, the model has to be related to reality during grasping by localising the object before picking it up. Section 2.1.7 reviews developments concerning the localisation of objects by means of pure vision, pure tactile sensing and exploratory procedures with different sensors.

The later proposed algorithm for the detection of contact parameters based on kinematic constraints, is founded on a particular mathematical description of contact, which also allows motion of this point of contact along the contacting surfaces. This description will be explained in detail in section 2.2.2. Next to the determination of contact parameters, another concern of this work is the model-based localisation of an object. In order to choose a suitable mathematical model for general objects, section 2.2.3 examines common object formulations.

2.1 Review of Related Research

2.1.1 Survey of Robotic Grippers and Hands

For most developments of robotic hands, the human hand was used as prototype, which was imitated, sometimes more, sometimes less. The human hand obviously has five fingers, one of which, the thumb, can oppose the others. In general, each finger has four joints, three of which can be moved voluntarily: The finger can be moved forward and sideways in the lowest finger joint and curled in a coupled motion of middle and upper joint. Also, in order to adjust the hand pose to the size of the object, the palm can fold such that the little finger moves inwards towards the thumb. In general, objects can be grasped with only three fingers. With two fingers, the object may easily rotate around the axis formed by the two. A fourth finger allows a stronger grasp, in addition to which it adds dexterity, i.e. the ability to move the object in the hand. A general need for five fingers is not given as can be seen from those people that have lost one finger. Nevertheless a fifth finger also adds strength to a grasp and is used in special situations, e.g. playing the piano.

Now, in order to spotlight the development of robotic grippers, which are the hardware platform for the ideas of this thesis, the current section shortly reviews major designs and, where applicable, examines their suitability for real-world

experiments or even commercial use. From the standpoint of application, most robotic grippers can be associated with one of two major areas of application, according to Butterfaß[But99]: hand prostheses and technical grippers.

For prostheses, researchers agree [KLC+01, CMM+01] that the design goals are low energy consumption, sufficient strength, light weight, size, low operational noise, reliability, appearance, price, easy and safe use and possibly also modularity to cope with different user desires. Most robotic hand designers claim that use of the respective hand as prosthesis is also feasible. Only some developments, however, were focused on the fulfillment of these requirements and can thus truly be regarded as prosthesis. A few products which use robotic technology are commercially available.

On the other hand, an abundance of designs for technical hands has already been created. Surveys of hands for technical applications are given in [LV02, Shi96, OSC00]. Although there are numerous different design issues, nevertheless two main concepts can be observed. As a sub-division to Butterfaß' classification, Lotti and Vasura [LV02] partition technical robotic hands with respect to their degree of integration: Numerous hands have been developed, which they call "modular", meaning that all actuators and most control circuitry are contained in the fingers or the palm of the hand itself. In contrast to this concept, in some grippers bulky components have been moved into or even beyond a forearm of the manipulating robot. The size of "modular" hands is usually larger than that of the human counterpart. However, since these grippers are self contained, they are easily portable to different robot arms. In the "non-modular" case, the dimensions of the hand itself can be kept small. As trade off, this hand is bound to the one arm it was originally designed for. Within these two groups, hands can further be distinguished by other design concepts. Hands vary in the number of fingers. Most recently constructed hands have 4 or 5 fingers. Some earlier examples were usually provided with 3 fingers. Also, the number of actively controllable degrees of freedom is characteristic for individual robotic hands. Another criterion of a robotic hand is its actuation, usually one of either electrical, pneumatic or hydraulic. Also hands vary in their size and weight. Finally, the degree of anthropomorphism describes the design of the hand. Some manipulators imitate the kinematics and appearance of a human hand. A goal, competing with anthropomorphism, is the dexterity of the hand, the ability to manipulate objects. A large distinction can be made with respect to a general real-world usability of the hands. This was not a goal in all of the designs. Hand designs partially concentrated on particular issues such as shape, velocity, strength or robustness and neglected other design goals. Thus, they may be very suitable for certain real-world tasks, but, they may fail in others.

The leading, commercially-available prosthetic hand is probably produced by Otto Bock [Ott03a] (see figure 2.1). It has five fingers, but only one degree of

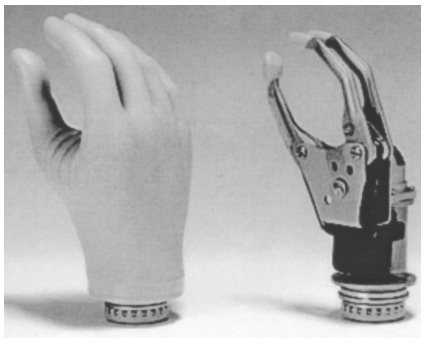

Figure 2.1: The Otto Bock^{tm} Hand [Ott03b]

Figure 2.2: The Karlsruhe Fluid Hand [Flu03, SPB01a]

freedom that opens and closes the hand to perform a fixed, mechanically-defined grasp. It is a very lightweight design of only $460g$.

The Southampton Hand [KLC+01], despite its larger complexity compared to the Otto Bock prosthesis, was thoroughly designed according to above design goals. Different approaches were tested before the final design. Thus, this hand exists in several versions. Amongst these versions, the number of fingers varies from three to six. Some versions have two, four or six actuated degrees of freedom, all of which are electrically driven. The weight of this hand is $964\mathrm{g}$. In contrast to most versions of Otto Bock prostheses, this hand is equipped with simple sensors: position encoders and motor current resolvers. Also, real-world experiments have been performed to use electromyograms for obtaining control commands.

A "wearable artificial hand" is described by Carozza et al. [CMM+01]. The main concern of this hand development is to be able to perform natural looking grasps and have humanoid appearance. One guideline for this hand is to decrease the required grasping forces by increasing the dexterity and the number of degrees of freedom. This development has three fingers with a total of six active degrees of freedom, which is more than usual for plain prostheses such as the Otto Bock Hand. Its weight is not reported. Studies about sensors have also been performed: In its prototypic version it contains position and true force sensors instead of motor current resolvers as with the Southampton Hand.

A novel approach of actuation has been examined in the Karlsruhe Fluidic Hand [SPB01b, SPB01a] (see figure 2.2). In order to avoid confusion, it is noted that at present there exist three hands termed Karlsruhe Hand: Two more hands are described later. The Karlsruhe Fluidic Hand is moved by new fluidic actuators that are inflated like balloons. This way, they exert forces on the finger skeleton. The

design of these actuators allows small size and low weight making it expedient for use in prosthetics. The Fluidic Hand has five fingers with 2 degrees of freedom each. The wrist has three degrees of freedom. The authors claim that their design is 50% less heavy than standard prostheses. For this hand, a synthetic skin exists rendering the appearance anthropomorphic.

As mentioned, the Otto Bock hand is commercially available. Also application tests with patients were performed with the Southampton hand and the Fluidic Hand. No tests have yet been reported with the "wearable artificial hand". The tested hands seem suitable for real-world applications, although the fluidic design may not be strong enough for all requirements.

Figure 2.3: The Barrett Hand [Bar03b, Bar03a]

Figure 2.4: The Salisbury Hand [Sal03, MS86]

As Butterfaß [But99] distinguishes hands with respect to their application, the second group of artificial hands is formed by the technical grippers. Following the further partitioning of Lotti and Vasura in terms of the structural design of the hand, amongst the group of "modular" hands is one of the earliest dextrous robotic hands, developed in 1983: the Salisbury hand, aka. Stanford/JPL hand [MS86] (see figure 2.4). This hand has three fingers and is electrically actuated. Its finger size is comparable to the human hand although the whole setup which includes a separate, non-anthropomorphic two degree-of-freedom robot as a wrist is larger. Compared to nowadays hands, its applicability to general real-world scenarios is low because it can only perform grasps with its finger tip. Nevertheless it was commercially available to robotic researchers and is used in several laboratories.

The developments at DLR, Hand I [BHKL98, LMBH98, But99] and the most recent Hand II [BGLH01, HBF$^+$03] (see figure 1.4) belong to the most sophisticated "modular" hands today. Both hands have four fingers with 3 actuated degrees of freedom each. A fourth, distal joint follows the motion of the third joint passively. DLR Hand II features an additional active degree of freedom in the palm. The palm can thus be adjusted to the desired type of grasp. Both hands

are electrically actuated. DLR Hand II can apply a force of about $30\mathrm{N}$ at the finger tip. This value is high compared to other designs. Despite this strength, the design of Hand II did not have to compromise in dynamic performance because joint velocities of up to $360^\circ/\mathrm{s}$ are possible. The hand geometry has been designed to be fairly anthropomorphic while the size is about 1.5 times the size of an average human hand. The weight of DLR Hand II is as low as $1.8\mathrm{kg}$. Both DLR Hands are highly sensitive: They are equipped with torque sensors at each joint and force/torque resolvers at the finger tip. Hand I also contains tactile sensors. Due to its "modularity", low weight, strength, the high number of degrees of freedom and its sensory equipment DLR Hand II is a well suited tool for researchers to examine general, complex applications in real-world scenarios.

With the HIT/DLR Hand [Liu03], a similar design concept as in the DLR Hand II is pursued. This concept, however, strives to reduce the complexity of the system and hence reduce cost as well as size and increase robustness compared to its precedent. As development is still ongoing, final data on the performance of this hand is not yet available.

Another recent development of a modular hand is the GiFu Hand [KSS01]. This gripper provides five fingers and an articulated palm. It has 3 degrees of freedom in each of the regular fingers and four degrees of freedom in the thumb. It is driven by electrical motors. The actuation is described to have a bandwidth as fast as $8 - 13\mathrm{Hz}$, which is relatively high. In contrast to DLR Hand II, its size is comparable to that of the human hand. Its weight of $1.4\mathrm{kg}$ is similar to that of the DLR Hand II. The trade-off for small size and high joint velocity, however, seems to be the low maximum force of only $1.1\mathrm{N}$ at the fingertip and $8.8\mathrm{N}$ at the thumb. Hence, in general real-world tasks, this hand may be too weak.

The Barret Hand [Bar03a] (see figure 2.3) is a simple gripper with three fingers and in total four active degrees of freedom. The joint between distal and proximal link of each finger contains a clutch, which opens at a certain torque level. Thus, the links are coupled under no or little load but decoupled on high loads, realising a passive degree of freedom. This allows robust grasps, which envelope an object to hold it. Its weight is reported to be $1.18\mathrm{kg}$. A particular design issue in this hand was robustness. Although the small number of controllable degrees of freedom limits the use of this hand to grasps with the whole hand, it is a commercially available technical dextrous robotic hand, which is also robust enough for industrial use.

As can be seen, the designs of the "modular" hands try to optimise the competing aims of velocity versus strength versus size and the aims of sensitivity versus robustness with different focus and result. These competing aims can be relaxed somewhat using a "non-modular" design. Hence, more researchers followed this design concept. One of the advantages of a "non-modular" design is that weight and size of actuators is not critical, and so most designs have approximately the

size of a human hand and the weight is not optimised. Hence weight is not reported any more within the following comparison.

The second classical development from 1984 in this review, the Utah / MIT Hand [JWKB84] (see figure 2.5), belongs to the "non-modular" hands. It has four fingers with 16 degrees of freedom. It is pneumatically actuated. The actuators are located on the robotic arm, which carries the hand. The force is transmitted through tendons. Provisions have to be taken against a change in tendon tension by a change in the robot configuration. In contrast to the other early design, Salisbury hand, this hand is able to perform grasps with all parts of the finger. In order to execute experiments in real-world scenarios, at least some mobility of the robot is required. However, the complete equipment of the Utah/MIT hand is fairly bulky. Hence, the construction of a mobile robot equipped with an arm carrying this hand is not feasible, limiting its use for general experiments. Nevertheless it was commercially available to researchers.

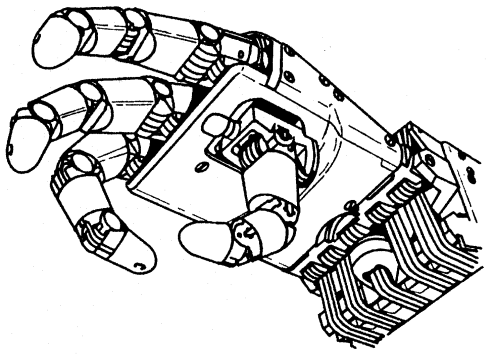

Figure 2.5: The Utah/MIT Hand [But99, JWKB84]

Figure 2.6: The NASA Robonaut Hand [NAS03, LD99]

The following two other early grippers are remarkable for their mechanical design. The University of Bologna (UB) Hand [BFV91] has three fingers with four degrees of freedom each and three degrees of freedom in the thumb. For the first time the wrist has been taken into particular consideration during design. The wrist has two degrees of freedom, which allow rolling in the forearm and bending of the wrist itself. The actuation is located in a particularly designed forearm. The size of the hand is comparable to the human hand. In version II this hand is equipped with intrinsic tactile sensors that measure contact forces remotely instead of local tactile impressions (see section 2.1.6). It is capable of performing grasps with the whole hand as well as with the finger tips. It is thus appropriate for real-world tasks. Its dynamical range and maximum force,

however, have not been reported.

The Belgrade/USC Hand [BTZ90] is the first well known gripper with five fingers. Only the thumb can be moved independently in two degrees of freedom. Each of the other fingers shares common actuation with a second finger. Both commonly-actuated fingers are decoupled by a rocker arm in order to allow one finger to continue closure while the other one is already in contact with an object. The hand may grasp objects with a weight up to $2.3\mathrm{kg}$. Its sensory equipment contains positioning sensors and force sensing at the finger tips. Similar to the "modular" Barrett Hand, this hand is only usable for enveloping grasps. In real-world experiments, researchers may have problems implementing all desired tasks with this hand, as manipulation in the hand is not possible.

The DIST Hand [CC98] has four fingers. With four degrees of freedom in each finger, this gripper has more degrees of freedom than its natural counterpart. It is electrically actuated. Forces are transmitted through tendons from a separate actuation box, which has to be mounted on a carrying robot. As an exception to the above stated disregard of weight as design aim, the weight of the DIST Hand including actuation is about $1\mathrm{kg}$. The torque of each motor is $200\mathrm{Nmm}$. As a design goal, only standard mechanical parts were used as far as possible. This hand is suitable to perform finger-tip and whole hand grasps. Due to its small size it is particularly suitable for mobile real-world applications even though the maximum grasping force is fairly low.

The LMS Hand [GZAL01] also has four fingers with four degrees of freedom each. It is moved electrically and its size is comparable to the human hand. It has position encoders at the actuator and at the joint. Joint torque can be computed indirectly by evaluating the elasticity of the tendons for power transmission. Its anthropomorphy is relatively high.

Two popular robotic hands have been solely designed for extra-vehicular space applications. The NASA Hand [LD99] (see figure 2.6) is designed as the limb of a space robot called Robonaut, which will assist human astronauts outside the protective shell of a space craft. The NASA Hand contains 5 fingers with a total of 14 degrees of freedom. Two degrees of freedom move the wrist. Thumb, pointer and middle finger have three degrees of freedom, ring and little finger one degree and the palm also one degree. Together with DLR Hand II, to the author's knowledge, these hands are the only hands with an additional active degree of freedom to reconfigure the palm allowing different positions of the fingers' base joints. The actuation of the Robonaut Hand is located in a specially designed forearm. The anthropomorphy of this hand is exceptionally high. Although designed for space, this hand is also very suitable for general real-world tasks.

The other hand designed for space operation is the SSL Hand [ACF02]. This hand has four fingers. Pairs of two fingers are located on two sides of a cubic wrist. The kinematics of this hand was optimised for the completion of tasks according

to the Extra-Vehicular Tools and Equipment reference Book of NASA. Up to now it is only manually operated through tendons. This hand is non-anthropomorphic but adjusted for its particular purpose in space.

A non-anthropomorphic design, which the developers claim is optimised for use in tele-manipulation, is presented by Jia et al. [JCX01]. It has three fingers. The thumb has three degrees of freedom, the other fingers have two degrees of freedom. In order to save weight, a single motor moves the individual degrees of freedom consecutively. Clutches are used to switch between separate joints. The motor and clutches are placed in a cylindrical actuation box also serving as a wrist. The low degree of anthropomorphism may limit this hand to particular tele-operational tasks.

Two hands, which trade anthropomorphy against the ability to manipulate objects in hand even better than man, are the Karlsruhe Hand II and the TU-München Hand [FW98, Woe95]. Both hands have four fingers that are arranged with a spacing of 90^o around a common centre. This arrangement allows very high dexterity for finger tip manipulation: Objects can easily be rotated and moved in the hand by moving individual fingers and regrasping. However, imitating humanoid grasping literally is not possible due to this non-anthropomorphic design. Hence, tasks which require an anthropomorphic execution in a humanoid environment are difficult to complete. The Karlsruhe Hand II is electrically actuated while the TU-München Hand is a good example for a hydraulic gripper. The Karlsruhe Hand II is equipped with pressure sensors for contact detection, position encoders and laser triangulation sensors. The TU-München Hand has its sensors located in the hydraulic actuation system. Thus no sensor components are necessary in the hand, rendering the design fairly small.

Finally, an interesting study of hand kinematics is described in [FTAD00] as TUAT/Karlsruhe Hand which is different from the previously mentioned Karlsruhe Hand II. This hand has five fingers with four degrees of freedom for each finger and one degree at the thumb. All degrees of freedom are actuated by a single motor. Research in robotic hands also triggered approaches by private experimenters with low budgets as presented in [Dio03], who built an impressive robotic hand from standard components.

Summarising this review, a wide variety of dextrous robotic grippers, both for prosthetic use and for humanoid robots, is already available to researchers, and some even to commercial applications. Beyond simple laboratory experiments, the wide range of hands nowadays allows usage in complex scenarios requiring more sophisticated control schemes and extended sensor information.

2.1.2 Common Sensors in Robotic Hands

Sensors in robot hands greatly enhance their capability to perform delicate tasks. However, each sensor requires additional hardware, which in most cases increases the cost and size of the hand and also decreases its robustness. Therefore, in constructing hands, most researchers also invested in the design of new sensors, which optimise these competing aims. This work proposes new methods to interpret already available sensor measurements to obtain more information in order to avoid new, specialised sensors. To allow an insight this section will revisit the general sensory equipment of robotic hands.

In general, there are up to four groups of sensors available in robotic hands:

- Position sensors are mostly required for position control of robotic hands. They are usually applied either directly at the motor shaft or even in the motor as *motor-side sensors*. Additionally, to be able to compensate for elasticities in the drive train, position sensors are sometimes also mounted directly to the joints of a robot as *load-side sensors*.

- Force and torque sensors are used to allow compliant control of a robotic hand and get information about the contact of the fingers with the environment. These sensors are usually implemented at the joint axis or within the structure of the finger. Further, some robotic hands are equipped with additional force/torque sensors at the finger tip which allow sensitive manipulation.

- Tactile and pressure sensors are mounted to the surface of the finger or palm. These sensors are fairly complex and are thus a topic of intense research. As these sensors are used to delicately detect small forces and the respective point of action, it is desired that theses sensors have a high spatial density and a high measurement resolution. Nevertheless, as also large grasping forces are possible when handling heavy objects, or hard impacts may occur when contacting an object, they also need to be robust. In order to allow the detection of multiple contacts on one sensor, the sensor is sometimes divided in several elements called taxels. Obviously, the spatial density requires a huge amount of wiring and evaluation hardware. Force/torque sensors may substitute tactile sensors by use of appropriate evaluation algorithms. Physically, between force/torque and tactile sensors, the borderline can be drawn similar to the corresponding senses in the human hand. In the receptors of the muscles of the fingers, man can feel strong forces required for motion and grasping. Detection of fine forces, of their variation or their point of action, however, relies on the tactile senses of the skin.

- Additionally, in robotic hands, operational sensors are required, that for example monitor the temperature of circuitry or stop the finger, when its limit of motion is reached. These sensors usually are standard components and are neglected in this survey.

In contrast to the classification of sensors by the quantity they measure, a measurement itself can be characterised with respect to the location of the sensor relative to the measured event. *Proprioceptive* measurements respond to stimuli within the system the sensor belongs to. For example the position of a motor can be estimated from its position resolvers or the force for an action can be felt in the muscle counteracting that force. In contrast, *exteroceptive* measurements render information about a different system. For example the ear receives stimuli from the outside. As will be shown in a later chapter of this thesis, position sensors from the actuation system can also be used to estimate the location of contact at the finger surface. The sensor, however, is not in the skin but in the actuation and is hence part of a different system. This perception is hence exteroceptive. Exteroceptive measurements can be used to obtain additional information without increasing instrumentation effort.

A recent overview of sensors in grippers can be found in [BM02, But99]. Organised by the quantity the sensors measure, their physical principles are briefly reviewed.

Position sensors have been built in several different principles: Motor encoders count the passing of one or several marked positions during motor rotation. Hall effect sensors [CMM+01, BFV91, BGLH01] measure the direction of the magnetic flux in the motor and hence allow the computation of the position of the rotor. Conductive plastics or potentiometers [BGLH01] react to their position-dependent change in ohmic resistance. Optical sensors [BHKL98] measure the location of light transmission through an encoder disc with a spiral slot.

Force/Torque sensors are mainly built in three different physical principles: in most designs a strain gauge is applied to a beam of defined elasticity in the structure of the mechanics. This strain gauge [CMM+01, BGLH01, HBF+03] has an output, proportional to the force or torque applied to the beam. Further, the elasticity in the hand's structure can be computed by pairs of position sensors [GZAL01]. Third, the power required for actuation can be measured as motor current [KLC+01, MS86] or hydraulic pressure [Woe95].

Due to the difficult optimisation of the competing aims resolution, cost, size and robustness, tactile sensors have been closely adapted to the particular needs of the respective researchers. A common classification is hence difficult. An overview of developments can be found in [LN99, But99, NL89]. More detailed than above, a discussion of technical considerations for tactile sensors is given in [MJ90]. Some famous early sensors are described in [Oka90, Fea90a]. The au-

thors of the first publication uses optical sensors to detect the displacement of a shell around the fingers, which is suspended with springs. The author of the latter employs a capacitive grid, a method also used in plenty of later designs. Modern sensors are based on a wide variety of physical principles which can roughly be divided into electrical, mechanical and optical effects. First, the change of the three basic electrical values resistance [LMH95], capacitance [JWR97, CJL98] and inductance [BM02, NL89] is used. The active material is built in a sandwich package of two electrodes and one separating material. This group is the largest amongst tactile sensors. Second, mechanical vibrations in piezo elements [JWR97] are exploited. Third, optical retardation of light transmission [JWKB84] in fibres may be used. Besides the physical principles of measurement, also the acquisition of measurements differs. Numerous designs reduced the number of sensor elements without reducing the spatial resolution by using a grid of sensors whose integral value is measured [BHKL98] or single pressure sensors [FW98]. As a trade off, this method can detect only single touches.

Concluding this section, it can be stated that a wide variety of sensors for robotic hands is available. However, providing a robotic hand with sensors is always a trade between increased sensitivity and robustness, size and cost. Hence, algorithms for efficient use of available sensors are desirable and motivated this work.

2.1.3 Applications of Robotic Hands and their Algorithms

In previous sections, a vision of humanoid robots or robots with partial anthropomorphic capabilities being used in real world applications was created. This section shows the structure of possible applications and reviews some scenarios in which robots were actually applied. Some of the required algorithms are pointed out. These algorithms need sensory information for which this thesis proposes new methods.

Applications of Robotic Hands

For a fully equipped robot with the ability to move by means of a vehicle or legs and having at least one arm and hand, two general fields of application can be identified:

In a *tele-operation* scenario, a human operator directly commands the motions of the robot. Tele-operated robots act as an extended arm of a human operator. They can be used in cases where the direct presence may not be possible. These situations occur in dangerous scenarios: in environmentally-polluted areas, fire fighting and disaster handling. Particularly equipped robots assisted in numerous kinds of rescue missions for example at Ground Zero in New York City [Mur02].

Secondly, tele-operated robots may scale up or down the motions and forces of the human operator. This is useful, on the one hand, when very precise motions have to be performed as in the assembly of electronic circuitry or handling of biological material [SW01] or on the other hand, when heavy goods have to be manipulated. This was for example required during the installation of an airlock, a door, to the International Space Station. Third, tele-operated robots may be used also in scenarios where particular knowledge is required and the expert cannot be present in person. This kind of tele-operation has been tested in the medical environment, here using particular medical tools rather than a robotic hand. For the control of the spatial motion of a tele-operated robot by a mobile platform or legs and for the operation of the arms, appropriate input devices are available, e.g. two joysticks with three dimensions each or one six-dimensional input device, called *spacemouse*. Other experimenters directly track the motion of the operator's wrist. In order to control the robotic hand, in most cases a cyberglove similar to [Cyb03] will be used. This glove measures the finger position of the human hand. Using appropriate transformations, the motion of the robotic hand can be commanded. In tele-operation, the application of a dextrous robotic gripper avoids the specialisation to certain tools for a particular task or a particularly prepared environment.

The second field of application of robots equipped with dextrous robotic grippers is their *autonomous operation*. In this field, also called *service robotics*, the robot first acquires particular skills in a job dependent training. Later, the robot may use these skills to perform certain tasks autonomously upon command but without further human interaction. As a vision, this type of robot will assist elderly, bodily-challenged or sick people with their regular work. Because the environment for these tasks was originally designed for humans and a large scale adaption will usually not be accepted, the robot has to be able to interact with it as man does. This requires a humanoid design of the robot, in particular of its hand. Experiments on autonomous operation are published in [BFH+03a, PJT+02].

While tele-operation has already reached the state of limited commercial application, truly autonomous robots are still topic of intense research. Only appliances with limited autonomy have made their way to market, such as robots which cut grass or sweep the bottom of swimming-pools. Nevertheless this field is driven by promising visions.

Algorithms for Planing and Control of Grasping with a Robotic Hand

Regardless of the type of task a robot performs, the algorithms used for grasping and manipulation are similar. It was already pointed out earlier that for the control of hands some information is critically required: the position of the object relative to the hand and the point of contact between a grasped object and the surface of

the finger. This fact will be explicitly shown for selected algorithms.

Surveys of algorithms for dextrous manipulation are given in [BK00, Shi96, OSC00]. Okamura [OSC00] identifies the following fields of work: Dextrous grasp and motion planing, dynamics and control, manipulation versus exploration.

The field of grasp and motion planing contains, amongst others, all research related to the choice of how and where individual fingers should touch an object as well as to the determination of the forces which the fingers exert at these points. The key issue here is to synthesise new or analyse given contact locations, so called grasps, which allow an object to be held without squeezing it out of the hand like for example a bar of wet soap. Thereby, particular problems occur, as the forces exerted at the contact point obviously have to be directed towards the object. They can only push not pull. Also a slippage of the finger may occur depending upon how these forces are exerted, e.g. very flat with respect to the surface such that the friction between the finger and the object no longer holds. Technically this problem is addressed for example in [HSB99], where contact locations are found as a solution to a constrained minimisation problem of contact forces. In [HTL99] grasping force constraints are solved as a linear matrix inequality problem. Borst and Fischer [BFH99] examine the weakest point in a complex hull of contact forces. Wang et al. [LW98] determine stability of a grasp using a ray-shooting algorithm in the convex hull of contact forces. Svinin [SUK99] determines the quality of a grasp by its ability to return to its original configuration after an external disturbance. Rather than the position of the finger skeleton, which would be directly controllable and measurable from the finger joints, all these algorithms deliver the desirable positions of contact on the object or their counterparts on the finger surfaces. When performing the grasp in reality, the actual obtainment of these positions thus has to be explicitly monitored and requires particular sensor evaluation. Related to the synthesis of a stable grasp is the computation of proper grasping forces. In [BS97, Sch01] the problem of optimal grasping forces is converted into a problem of minimising a matrix equation. Trinkle [HTL99] extends his approach of linear matrix inequalities to the determination of optimal grasping forces. As the grasping forces act on the point of contact, again this information is required.

For the field of control, only a few representative topics are mentioned. Research is concerned with the driving of individual fingers as well as the coordination of several fingers of a hand. When manipulation is desired, sometimes re-grasp operations, called finger gaiting, are required to move an object in hand without having to deposit and re-grasp it. Also, the monitoring and correction of planned grasps has to be performed. Hereby, knowledge about the point of contact is required in order to stay in touch appropriately with the grasped object. Also, as active manipulation and repositioning of objects is one of the main intentions of grasp, the position of an object has to be determined during closed loop control.

Liu [LH99] describes Cartesian control for individual robotic fingers. Arimoto [DA99] develops hybrid force/torque control for combined control of grasping forces and finger position. Salisbury [MS86] pioneers a coordination scheme for several fingers. Schlegl [SB98, Sch01] proposes a hybrid discrete-continuous control setup allowing for individual fingers to break contact in order to re-grasp. In [SHB+99, Hai98] a method to compensate for a mismatch between grasp planing and real-world is proposed.

Finally, research about exploration is so closely related to the detection of the point of contact such that both are reviewed uniformly in section 2.1.6.

This section pointed out applications of robots equipped with mechanical hands, and highlighted some of the algorithms used for hand operation. All of these algorithms require the position of the contact point, some of them additionally need the location of the object.

2.1.4 Physical Models of Contact

In order to implement robotic grasping, a thorough understanding of the physical principles of contact is required. Generally, an object in free space can move along three translational directions and rotate around three axes. The motion thus has in total six degrees of freedom. In the remainder of this section, we consider quasi-steady-state conditions, i.e. there is no considerable acceleration.

Two bodies in contact cannot penetrate each other. When they slide one on top of the other, friction may occur. Physically, contact can be defined:

Definition 1 *By contact the relative motion of two bodies touching each other is obstructed completely in some directions. In other directions the motion is subject to friction forces, and in the remaining directions it stays completely free.*

When a finger tip touches an object, the direction orthogonal to the surface is obstructed. The finger cannot move into the object. Sliding sideways is possible, however, frictional forces counteract this motion. Rolling along the surface is not inhibited, because in practice the rolling friction is negligibly small in this context. Each completely obstructed direction of motion corresponds to a direction in which a force or torque can be applied. By actuating the robot in that particular direction, these forces and torques can be freely set. In the example, no restrictions apply on how hard the finger can press onto the object, provided the object itself can withstand this force. In the completely free directions, no forces can be applied. A single finger in the example cannot rotate the object as each movement of the finger would only cause a rolling motion along the object. Between the two cases are those directions that are subject to frictional forces. These forces are limited by physical friction constraints. Up to three independent directions of

force and three axes of torques are thus possible at most. The actual number depends on the properties of the two surfaces in contact. These properties are termed contact model. The research on contact is first of all concerned about the model of contact which is characterised by its free, frictional and obstructed degrees of freedom. Also, as some degrees of freedom are not obstructed, the evolution of the contact is considered when relative motion occurs between two objects. Second, physical models for the deformation of contacting objects and derivations of the contact friction phenomena are examined.

Contact as Constraint to Motion

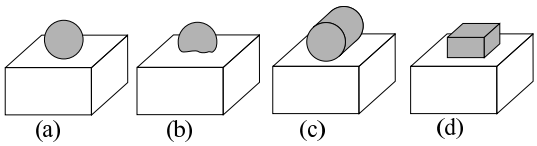

Figure 2.7: Standard contact types

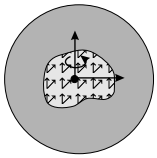

Figure 2.8: Contact centroid

The first recent examination of contact in the field of robotic hands has been performed by Salisbury [MS86]. He regards fingers and objects as rigid bodies such that the interacting parts do not deform or penetrate each other due to contact. He introduces eight different types of object-finger contacts. Physically, these types of contact differ in the shape of the contact area and in the consideration or disregard of friction. All of them are represented by a lumped point of interaction restricting motions and admitting forces.

- *Point contact* with and without friction are the most important contact models. These types restrict plain relative translations between the two bodies in contact in all three spatial directions or only in the direction of the common surface normal, respectively. This contact is depicted as a hard sphere on a hard surface in figure 2.7 (a).

- He also describes *soft finger contact* inherently including friction as model admitting only rolling on the surface. Translational motions are inhibited as well as a torsion around the common normal direction. This contact is widely used and is depicted in figure 2.7 (b): A soft sphere contacts a rigid plane.

- The *line contact* (see figure 2.7 (c)) is proposed with and without friction. With friction, it allows only rolling around its axis; without friction it in-

hibits translation along the direction of the normal to the plane and rotations are allowed around the normal and the axis parallel to the line of contact.

- The *planar contact* (see figure 2.7 (d)) is introduced also with and without friction. In the frictional case, the planar contact is totally fixed; in the frictionless case it allows translations along the plane and the rotation around the normal to the plane.

It is common to all of these models that only geometrically first order aspects are taken into account, i.e. are concerned only about local tangent planes and neglect curvature effects. Salisbury also introduces the property of unisense force limitations. This property requires that forces at a contact between two bodies can only be pushing, not pulling and that tangential forces, if present in the model, have to lie within the Coulomb friction cone.

Salisbury modeled the physics of contact by constraints of motion and forces at an isolated contact point, despite an obvious contact area in soft finger, line and planar contact. An extension to the soft finger contact is presented by Bicchi [Bic90, BSB93]. He introduces so called equivalent sets of forces. These equivalent forces cause the same large scale effects as the locally distributed forces in a soft finger contact. The point of action of these forces is termed *contact centroid*. At this point, the equivalent force is directed into the object and the moment is parallel to the surface normal at that point. Bicchi derives properties of the contact centroid proving that all real contact points lie in a convex region around the modeled contact centroid. The contact centroid of a possible contact patch between a soft sphere and a plane is depicted in figure 2.8.

While the previous researchers concentrated on the geometric properties of a contact which impede motions and admit forces, Montana [Mon88, Mon95] regards the contrary. Depending on the model of contact, similar to the above, he describes the admissible motions of the two rigid objects in contact as sliding or rolling on each other. This is called the kinematics of contact. He regards the contact as an additional joint which adds up to five degrees of freedom, according to the type of contact. This joint is passive, i.e. is not actuated. Since parts of the work presented here mostly rely on Montana's methods, subsection 2.2.2 revisits his work in detail. His methodology is valid for any geometry of objects and hence in contrast to the above it is not strictly limited to the approximation of objects by geometrical first order tangent planes. The phenomena of deformation and generation of friction forces are not considered in his work

Similarly, Rimon and Burdick concentrate on the possibility of an object to move under contact. They introduce a configuration-space approach to uniformly describe motions and forces in space [RB95a, RB95b, RB98a]. In this description, any object position is represented by its translation and orientation in space, the so

called configuration. The union of all possible configurations forms the configuration space in which an object resides. So far, the object may take all configurations in this space. However, fingers of a hand are also described by their configuration. They are regarded as obstacles to the body resulting in the obstacle space. The intersection of object configuration space and obstacle space represents the free space of the object. In this representation, forces are represented as cotangent vectors. Although less intuitive on first sight, this representation allows consistent description of some phenomena of contact with a single approach. At first, Rimon and Burdick [RB95a] represent contact as a constraint on the possible velocities of an object. They term this "first order constraint of motion" in one particular direction in configuration space. Being concerned with velocities rather than geometrical tangent planes to an object, "first order" in this term refers to the time domain instead of the spatial properties as before. In terms of physical interactions between object and finger so far, this methodology is still equivalent to the model of point contact without friction. However, paying attention to the fact, that "contact is not an infinitesimal notion but a local one" [RB98a], the contact description is extended in the consequence [RB95b] to second order acceleration effects in the time domain. They show how the velocity has to change in order to move along a surface. This inherently extends the description of contact also to respect second order curvature effects in the spatial domain. This is advantageous for cases of a relative motion between two contacted bodies where the curvature of the surface is important as for example in some concave contacts. This has not been regarded in the geometrically first order models of Salisbury and Bicchi. Montana , however, also regards curvature on objects and examines admissible velocities. In the spatial domain his approach is hence second order. Nevertheless he is only concerned about velocities and hence his method is only first order in time.

In different complexity, all of the above models describe contact as the impedance or admittance of motions. However, during contact, deformation of the contacting surfaces can also be observed which produces forces opposing this motion. This not only generates those forces impeding a motion but also generates friction forces.

Contact as Cause for Forces

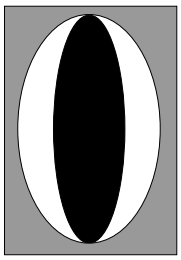

Figure 2.9: The Mason paradox

To model force phenomena, Rimon and Burdick [RB98b] extend their contact description to the generation of forces. They present the Mason paradox showing that a rigid body model is an insufficient description of phenomena in some cases. The argument in the paradox is shown in an example: two rigid frictionless ellipses with identical centre of symmetry, common major and minor axes and the same radius on the major axis, are located one inside the other and differ only in the radius of the minor axis (see figure 2.9). Thus, they touch each other at both intersections of the major axes with the ellipses. Obviously, there is only the one way depicted, to fit the black ellipse into the hole formed by the second ellipse. Hence the inner black ellipse cannot move inside the outer gray. This configuration, however, cannot produce forces tangential to the ellipses at the contact points at the top and the bottom of the black ellipse. It is of no importance whether friction is assumed or not, as no normal forces are present when the inner ellipse is moved strictly horizontally. In order to impede a motion in this direction, forces would be physically necessary. This contradiction indicates an imperfect model of contact, assumed so far. Thus Rimon and Burdick introduce several elastic deformation contact models:

- The *Gesley's Model* still considers rigid bodies and lumped contact properties but also allows an overlap. The overlap causes a force which depends on the minimal distance to separate the objects and its rate of change as damping. This is not a linear spring model since the separation distance usually does not depend linearly on the displacement between the two bodies in contact.

- The *Hertz Model* is also a lumped parameter spring model, however, without damping. This approach relates material properties to the lumped spring constant. This spring constant then relates an applied force to a displacement through an exponential relationship.

- The *Inelastic Damping Model* is an extension of Gesley's Model to also include damping orthogonal to the direction of penetration. This is amongst others of importance for cases where a body is rolling on a plane and thus not changing its penetration which results in zero damping force in Gesley's Model.

Xydas and Kao [XK99] examine the Hertz Model and state that the underlying relation between material and model parameters is only valid for linear elastic material. In the development of robotic fingers and in the quest to develop as good

as possible artificial skin, nonlinear materials are often used. Thus an extended *Nonlinear Elastic Model* is developed which in a special case includes the Hertz Model.

Howard and Kumar [HK93, HK95] propose a very accurate *dynamic frictional soft finger model*. They develop a description of the kinematics of deformation of both contacting surfaces as a function of position in the contact area. Forces in the contact area are represented as distributed forces at small elements of the contact region. The relation between the displacement of the object and the resulting forces at the surface elements is linked to influence functions. These are represented through material properties. Because of the computational burden of this very accurate model, they propose to use a coarse grid for the representation of surface elements. In the limit case this results in a lumped parameter model. For global examinations, they propose to approximate the distributed contact by one single centroid and use the full model only locally for examinations at the contact itself. On the other hand, in [HK95], they also present a method to relate lumped elasticity parameters from the Hertzian Model to a curvature dependent contact stiffness matrix. The latter relates forces and displacements at the contact.

The contact models introduced in the last two subsections describe the mobility of two objects in contact and the resulting forces from contact. Considering the goals of this work and examining the contact models proposed by researchers, the most suitable contact model seems to be Bicchi's description of two rigid bodies in soft finger contact at the contact centroid from [Bic90, BSB93]. This model is simple and yet accurate enough.

2.1.5 Grasp as Interaction of Multiple Contacts

In the strive for humanoid robots, one of the driving forces for the development of a robotic hand is the requirement to be able to pick up and firmly hold general objects.

Definition 2 *The power of a robotic hand to seize an object and hold it in position is called grasp.*

A grasp can be seen as the interaction of several contacts as introduced in the previous section. The location of these contacts determines whether a grasp can stably and securely hold an object. When these contact locations are not diligently chosen, the object may be squeezed out of the hand by the own grasping forces or may be moved out by external disturbing forces.

Further, the shape of the hand and the type of contact between fingers and object is important for the robustness of the grasp against external disturbances and misplaced contact points. Competing with the robustness of grasp is the ability to

manipulate an object in hand: The more robust a grasp is, the more firm is also the hold on an object. But as a direct consequence, the possibilities to reorient or move the object without putting it down decreases.

The technical chapters of this thesis only work with one or several contacts alone and are interested in neither of these two aspects of a grasp. Nevertheless, grasps are basic for robotic hand applications. Thus, both aspects of a grasp, i.e. the location of its contacts and the posture of the hand, are reviewed here for the interested reader. Surveys on the general topic of grasping can be obtained in [BK00, Shi96, OSC00].

Conditions for a Stable Grasp

In order to securely fix an object, two methods exist. First, the object can be retained by a number of passive contact points that are fixed in position but obstruct all possible motions of the object. For the two-dimensional case, figure 2.10 (b) shows a sample apparatus. The fixed beams touch the object and are not necessarily connected to it. The beams may be pre-loaded in order to exert a constant force on the object. The object can neither move up nor down. It is fixed. Second, an object can be held by actively-controlled contact forces. On the one hand, these forces balance out all external disturbances and hence fix the object. On the other hand, finger forces also press the fingers onto the object. These forces are called *grasping* or *internal forces* as they cannot been observed from the outside of the object, provided the object is rigid and does not deform. With two surfaces in contact, according to Coulomb's friction law, the maximum possible frictional force is proportional to the force acting normal to the surface in contact: $f_{\parallel} = \mu f_{\perp}$. Thus internal forces guarantee safe contact with sufficient friction. A setup which actively holds an object is depicted in figure 2.10 (a).

In planar or spatial setups, these two cases differ by the number of required contacts for a stable grasp. Both cases may use any contact model, with or without friction. The ability to hold an object is called *closure*. The passive case is called *form closure*, as it is retained due to the form of an external apparatus, whereas the active case is named *force closure*, due to the applied finger forces. In most (e.g. [Bic95]), but unfortunately not all literature this illustrative nomenclature is used. Thus, it will be applied throughout this thesis. A formal definition follows as research is reviewed that describes conditions for the stability of a grasp.

In [MS86], Salisbury proposes stability definitions of a grasp: He states that in order to immobilise a body one of two conditions has to be fulfilled: Either the intersection of all those free motions of the object's centre of gravity is zero, which are not already inhibited by the individual contacts alone. Or the set of the sums of all forces, which may be transmitted through the individual contacts, span the whole force / torque space $\Re^6$. Differing from the convention in this thesis,

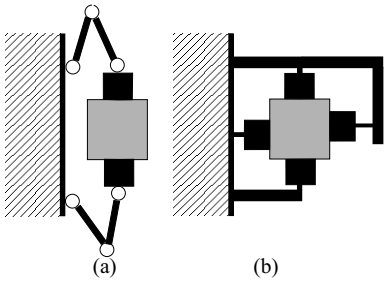

Figure 2.10: Schematic of *force-* and *form-closure*

he defines force closure as the ability to immobilise an object with controlled forces plus known external forces. This is the case when an object lies on the open hollow hand and gravity presses the object against the palm. In contrast, he defines form closure as the ability of a grasp to hold an object without the help of external forces. It was found that the minimum number of fingers necessary to immobilise an object is 3 when using point contact with friction and is 6 for point contact without friction. These numbers, however, hold only for the case of the contact which also allows pulling. Form closure in Salisbury's terminology can be achieved with a minimum of 7 frictionless point contacts, when unilaterality of the contact is respected.

Concentrating on the case termed force closure in this work, Mishra, Schwartz and Sharir [MSS87] also give a similar definition for stability in frictionless grasp stating that a grasp is said to be "force/torque closure if and only if any arbitrary external force/torque acting on the object [..] can be balanced by pressing the finger tips against this object at the selected grip points". They concentrate their examination on the required amount of contacts. A minimum number of fingers required to fulfill this requirement is found to be 7 in the spatial and 4 in the planar case. In contrast to Salisbury, they also examine exceptional surfaces which cannot stably be held by any number of fingers in the frictionless case. These surfaces contain all rotational bodies: no kind of grasp can resist rotation around their axis.

In contrast, Mattikalli and Khoshla [MK92] regard form closure. They geometrically describe directions of motion which are obstructed by contacts. This way redundant constraints can be identified.

Bicchi [Bic95] finally defines force and form closure in a clear way, as it is mostly used in later literature. Concretising the illustrative definition given above, he establishes form closure in the following manner:

Definition 3 *" A set of contact constraints is defined to be form closure if, for all object motions, at least one contact constraint is violated."*

These contact constraints are equivalent to the obstruction of motion through con-

tact as introduced in the previous section. Bicchi also revisits a form closure test and proposes *partial form closure*, when only some directions of motion are obstructed. An algorithm to determine directions of free motion is presented. The latter is mostly necessary for workpiece fixation. He also defines force closure as:

Definition 4 *"A grasp is defined to be force closure if, for any external wrench acting on the object, there exists an internal contact force such that all friction constraints are fulfilled."*

In this context, "internal" refers to forces at the individual contact points rather than to the internal, grasping forces. This definition is also extended to partial force closure. Bicchi additionally presents a test for force closure.

In contrast to the strict definitions of stability as given by the last cited researchers, Cutkosky [Cut89] develops general characteristics to describe a grasp. He identifies the effective compliance of the grasped object with respect to the hand, the connectivity, namely how many parameters are needed to specify the position and orientation of an object with respect to the hand, force and form closure, grasp isotropy as the ability of the fingers to accurately apply forces and moments to the object, internal forces, manipulability as the ability to impart arbitrary motions to the object, resistance to slipping and stability as the grasp returning to its initial configuration after being disturbed.

More recently, but not following the common manner of definitions, the following two groups also examine stability.

Trinkle, Farahat and Stiller [TFS95, TFS94] introduce the notion of "stability cells" to the first and second order. These stability cells reside in the configuration space. The configuration space approach by Rimon and Burdick to uniformly describe the phenomena of contact has already been revisited in section 2.1.4. For first and second order stability cells, any perturbation of an object away from its equilibrium increases its potential energy in first and second order respectively. A first order stable object corresponds to a marble in a cone, a second order stable object to a marble in a flat bowl. They also distinguish between active and passive stability cells. In the first, a grasp is controlled by joint torque, in the latter the grasp is independent of it. This notion is more feasible for trajectory planing of a partially grasped object in order not to loose grip on it than for general stability examinations.

Following their work already presented in section 2.1.4, Rimon and Burdick [RB96] introduce notions of first and second order form and force closure for the frictionless case. They consider first and second order free motions of an object in configuration space with respect to the grasping fingers in obstacle space. The free motions are the union of those motions in configuration space that move along the obstacle surface and those motions braking away from the obstacle. In first order motions, the actual velocity is directed tangential to or away from the

obstacle surface. In second order motions the path is directed along the curvature of or away from the obstacle surface. Although noted in the abstract configuration space, those motions represent the motions tangential to or along the curvature of all fingers' surfaces plus those motions which break at least one contact. Rimon and Burdick define first and second order form-closure as the absence of first and second order free motions. They also prove that, in the frictionless case, the common notion of force closure is equivalent to first order form closure. According to their definition a grasp is said to be second order force closure if it is first order force closure and if also the derivatives of the free motions only cause accelerations along the surface of the obstacle. Only their first order notion is extended to frictional contacts.

The previously reviewed work is concerned only about the stability of a grasp. Closely related to the stability is the existence of *internal forces* which occur in force closure grasps as squeezing forces on an object.

Salisbury [MS86] proposes an approach called grip transform to compute the forces and velocities of the object when forces and velocities are imposed at the individual contact points. The method produces a matrix similar to the Jacobian of a robotic manipulator. This grip transform matrix has a nullspace. Those contact forces that lie within this nullspace are identified as *internal forces*. Their basis vectors are the orthogonal basis vectors of the nullspace. No physical interpretation can hence been given to the basis vectors of this internal forces.

Yoshikawa and Nagai [YN90] also introduce a decomposition of contact forces into internal forces and manipulation forces acting on the object. This examination is done in the spatial case for only a three fingered grasp. Their decomposition can be physically interpreted in contrast to the plain orthogonal decomposition presented by Salisbury.

Finally, Bicchi [Bic93, Bic94] examines force decomposition into manipulation and internal forces when not all contacts can be controlled independently. This is for example the case when the body also contacts multiple links of a finger or the palm. For the computation of manipulation forces, a weighted pseudo-inverse is used. The internal forces are partitioned in actively-controllable and passive preloading forces. For the controllable internal forces, a matrix is determined which projects motions in the joint space of the fingers through the Cartesian contact space to the space of internal forces. When the mapping from joint space to the Cartesian contact space has a nullspace, non-controllable internal forces do exist.

This subsection revisited popular definitions of grasp stability and also examined the phenomenon of internal grasping forces which press on an object without external effect.

Grasp as Particular Posture of the Hand

Grasps are not only distinguished by their abilities to hold or manipulate an object. They also differ by the posture of the hand and as a result of the posture in the number and types of contacts (see section 2.1.4). Most researchers agree on

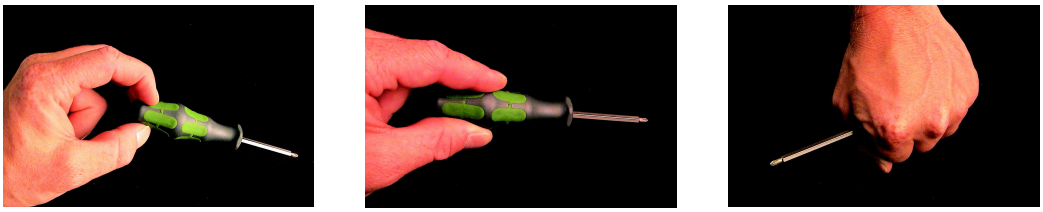

(a) precision grasp (b) pinch grasp (c) power grasp

Figure 2.11: Major types of grasp

a rough partitioning of grasps in *precision grasps* and *power grasps*. Both grasps are depicted in figure 2.11 (a) and (c). *Precision grasps* use only one contact per finger, which is normally a point contact or soft finger contact. These grasps can easily reorient and move the object within the hand, but with even small uncontrolled external disturbances or misplaced contact points they are likely to lose an object. The contact forces needed to firmly hold an object are large. On the other hand, *power grasps*, or as they are often called *enveloping grasps*, have multiple contacts at the fingers or even at the palm, enveloping an object. The large number of contacts causes a loss of controllability of individual contacts. Therefore the occurring contact types largely differ. No particular, single type can be identified. The power grasp exhibits almost no possibility of in-hand manipulation, but as a direct result, it is much more robust than its counterpart. There are numerous kinds of grasps borrowing from the advantages but also from the disadvantages of both extremes such as a *pinch grasp* (see figure 2.11 (b)) which aligns the distal links of a robotic gripper with the surface of an object and thus makes line contact with the grasped item.

Reviewing literature, Cutkosky [Cut89] studies the grasp of machinists in a batch manufacturing task. He classifies the findings into stability-based power grasps and dexterity-based precision grasps. The first group is again partitioned by the requirement of clamping into prehensile and non-prehensile grasps and then subdivided by the shape of the object into grasps for thin (*lateral pinch grasp*), long (*prismatic power grasp*) and compact (*circular power grasp*) objects. The latter group is divided only into *circular* and *prismatic precision grasps*. The grasps are chosen according to the object shape put also on the task to be performed.

An overview of the different kinds of grasps can be found in [SPB01b]. The authors describe a *lateral grasp* similar to a pinch grasp where the thumb's distal

link is parallel to the surface of a thin object and is opposed by the supporting side of the medial link of the pointer finger. They also describe a *hook grasp* which humans use to carry a bag.

In this section, definitions of stability of a grasp were reviewed from literature. The main concept is that a stable grasp impedes the motion of an object either passively in a form closure grasp or actively by applying forces in a force closure grasp. Internal forces are identified as those forces that squeeze an object into the hand. Special hand postures define the robustness and dexterity of a grasp.

2.1.6 Detection of Contact and Geometric Object Exploration

One of the main parts of this work is concerned with finding the point and normal on the surface of a finger when it is in touch with an object. This problem proves to be similar to the problems of object exploration. The latter is a systematic and repetitive determination of these contact properties. Klatzky [KL90] studied those exploration strategies with human subjects. This section consequently reviews methods from both fields. In general, there exist several methods of detection of contact. It is most obvious to exploit tactile sensors (see section 2.1.2). These, however, are still rare even in modern hands (see section 2.1.1). Thus, other methods have been developed. *Intrinsic* methods use a six-dimensional force/torque sensor mounted in the finger, geometric methods use exploratory motions along the object and interpolate its surface.

The intrinsic methods were the first to be found. For the case of point contact with or without friction and no contact torques, Salisbury [MS86] relates the measurements of a force/torque sensor to the unknown contact force. This relation depends on the location of contact. In closed form, the contact point can be determined. With line and planar contact, this method fails due to the larger number of admissible contact forces/torques. Salisbury proposes the use of multiple successive measurements with the same principle. Bicchi extends Salisbury's development to the case of soft finger contact. As point of contact, he introduces the contact centroid (see 2.1.4) in [Bic90, BSB93]. Salisbury and Bicchi both present closed form solutions for particular contact models, eventually with multiple measurements. An adaption to special contact models is not provided. Instead of using a tip sensor, a method using joint position and torque measurements of several fingers is proposed by Funahashi [MF93]. The contact location is determined by disturbing the grasp infinitesimally and using Salisbury's grasp matrix given in [MS86] (see section 2.1.5). A simple geometric heuristic for detection of the contact normal during a multi-fingered grasp is used in [SHB+99].

In contrast to the previously presented static detection that only requires measurement of one single contact, also exploratory motions are possible. These increase the amount of information by taking multiple measurements. Also, curva-

ture may be detected this way. In a series of articles Kaneko, Tanie et al. [KT90, KMT92] propose sliding as probing strategy called *self-posture-changeability*. The probing uses both compliantly-controlled and position-controlled joints. They approximate the link of the robot that makes contact with an object as line. This leads to the determination of the contact point as the intersection of the link lines in the different positions of two samples. Grupen and Huber [GH93] extend the work of Tanie with a position correction term for a spherical geometry in the finger tip. For the two-dimensional case, motion along the surface of an object is also used here to additionally confirm a position estimate. Muto [MS93] proposes a principle of using force measurements similarly to Salisbury's and Bicchi's proposal. He uses a formalism known as motor algebra. In order to increase robustness during motion velocity measurements are also respected. For application in tele-operation, Dupont et al. [DDH00, DSMH99] introduce a method to estimate general parameters of a tool-object contact as its position or the radius of a simple object from individual measurements of the robot's position through contact constraints. Dutré, Bruyninckx et al. [DBDD97] propose a Kalman filter to track the contact points between a grasped peg and a gripper from velocity and force measurements while moving it over a planar surface.

A lot of researchers also used tactile sensors to explore the object. Although not directly in the focus of this thesis that strives to replace tactile sensors by intelligent evaluation of other sensors, some of the methodology in tactile sensing is nevertheless of interest. Maekawa, Tanie et al. [MTK95, ZMT96] study the detection of surface as normal and curvature at the contact with tactile sensors from rolling. They describe the problem as an iterative solution of a matrix equation. In [CRZ96] the previous ideas are applied to quadric surfaces. Bicchi [BMP99] proposes object exploration by non-holonomic rolling and surface approximation by variation calculus. Passive exploration is introduced by Erdmann [Erd98] where the motion of the object is caused by uncontrolled sliding of the object. Caselli et al. [CMZC96, CMZ95] obtain tactile contact information systematically and use it to build up a volumetric object model as *enveloping polyhedral model* or *contact only polyhedral model*. Cutkosky et al. [OC99, OTC97, OCT$^+$00] extract surface features like edges with a tactile sensor and by the observation of the motion of the fingertip centre, the latter in the context of enhanced tele-operation. Charlebois et al. [CGP99, CGP96] use tactile sensors during exploratory motions to estimate local curvature and shape of an object.

This section presented a wide variety of methods to detect surface parameters like the contact point, the normal and the curvature when fingers touch an object. Intrinsic measurements have been proposed as general means, also special geometric exploration may be used. Tactile sensors are applied to obtain more general information about the surface than with the first two methods.

2.1.7 Methods of Object Localisation

For proper grasping, the object position is required. This can be done by either locating any object in a scene regardless of its appearance or by finding a particular object previously modeled. The latter approach inherently also contains the recognition of objects. This, however, is beyond the scope of this work. The position of an object can be obtained from both, vision like sensors or contact sensors. The main difference between both sensors is first of all the density of information which is much higher in optical sensors [GL84]. Further, the optical sensors mostly are installed external to the hand. Thus they can measure contact-less but require a calibrated relation to the position of the hand. Also, obstruction of the view by other objects or the hand itself may occur during vision. Contact sensors, however, can be applied locally and thus cannot be obstructed, but, on the other hand, are not able to spot an object before contact is made. They are firmly connected to the hand. Calibration of their relative position can thus be done by design and is fairly robust because of the small levers between the sensor and the hand. The robustness is also increased, as there usually are multiple, spatially-separate contact sensors available in robotic grippers. Use of this redundant information decreases the influence of individual calibration errors. Additionally, control and localisation relies on the the same sensory information. Calibration errors may thus cancel out. Despite the difference in the modality of sensing, the algorithms that extract the position of an object from measured data are similar. In both cases, the algorithms rely on a number of sampled points on the surface of the object. Hence, when describing these algorithms in the consequence,"look" and "visual" can be seen interchangeable with "feel" and "tactile".

Methods of localisation can be parted into two groups as suggested by De Geeter et al. in [GBSD96]. These systems mainly use two strategies in order to localise an object and then manipulate it: *look-then-move (feel-then-grasp)* systems determine the position of the object before starting a motion. Two examples of this strategies have been presented in [FBH+01, BFH+03a]: In the first example, a robot is programmed to catch a thrown ball. The ball is tracked, and the arm is commanded, after which an absolute position for the catching location is determined. In the second example, a door handle is pushed and a soda can is picked up from a table after locating each item respectively. On the other hand *visual servoing (feel-during-grasping, tactile servoing)* systems constantly adjust their motion from a continuous stream of location information. In [BFH+03a, BMG00], two examples of *visual servoing* are presented. Here a Jacobian matrix is used to describe the motion of the robot in the camera image when its joints move. This way, directions of velocity instead of positions are commanded to the robot. Malis [Mal02] uses a similar classification of location and subsequent control into *model-based visual servoing* and *model-free visual servoing* respectively. With

the term “model”, Malis describes knowledge about the absolute position of the camera with respect to a reference whereas model-free servoing again acts incrementally. Finally, combined approaches have been presented [HPS+00].

An example of object localisation by vision is presented by Magnor [Mag02]. He uses a Cany edge detector to spot objects in the image of a standard camera. The edge images are convolved with learned object outlines. The best fitting match can be chosen from this convolution. Blais et al. [BBEC01] use laser scanners combined with a camera. They employ triangulation of multiple laser scan points on a predefined marker attached to the object to locate the object. This is resolves lighting conditions of pure camera systems. In [JL00], Jogan and Leonardis determine the position of a moving panoramic camera by finding the location of the recent image in the eigenspace of learned images. A similar approach is taken by Leonardis and Bischoff [LB96]. De Geeter [GBSD96] uses ultrasonic and infrared sensors for application in nuclear environments. The ultrasonic sensors measure the distance of a point on an object. The infrared sensor detects edges of an object by their calibrated change of reflection when a scan of an object is performed. A constrained Kalman filter is used to track the edges during motion.

A combined approach of vision and several in-hand sensor systems mainly for the use with the Barrett-Hand [Bar03a] (see section 2.1.1) is proposed by Allen et al. [AMOL99, AMOL97].

Amongst the plain tactile methods of object localisation and recognition, an early approach of “feel-then-grasp” is given by Fearing [Fea90b]. Three appropriately chosen contact features from a Linear Straight Homogeneous Generalised Cylinder (LSHGC) description of objects are used to estimate the position of the object. Caselli [CMZC96] examines objects described by *enveloping polyhedral models* (EPM) built up during tactile exploration. The objects are first recognised from a predefined set by match of dimensional features and then implicitly located. In the “tactile-servoing” group, Maekawa [MTK95] implicitly locates an unknown object and guides it along a desired trajectory using tactile feedback. The approach taken by Jia and Erdmann [JE98, JE99] observes an object in motion for position estimation using a Kalman Filter to locate its centre of gravity. Grimson and Lozano-Pérez [GL84] compare a polyhedral model of an object to sparse tactile data. This method tries to find a matching position of the object that aligns measurements and suitable polygons of the model. Suitability is determined through the existence of a translation and rotation for all measurement / polygon pairs. In order not to test all possible permutations of model polygons a search tree is put up and branches are pruned that do not match certain criteria of rigidity of the grasped object. The location and orientation of the object is computed analytically from a minimum amount of, i.e. two and three respectively, measurement / polygon pairs. Measurement errors are reduced by taking the average of several clustered solutions using different pairs. A similar approach by Faugeras

and Hebert [FH86] is mainly intended for visually-based sensing. Points, lines and planes are matched against a model consisting of the same primitives. Some criteria of rigidity are used to sort out infeasible combinations of primitives: Sequentially, each measurement is assigned a possible feature on the model. In the following only those parts of the object are examined that comply with the relative position between object and model defined by the previous matches. In another approach, Stein and Medioni [SM92b, SM92a] describe objects by surface features, in particular curves obtained on edges and splashes obtained on smooth portions. The latter can again be mapped onto curves in space. These publications are originally targeted to visual object recognition. An interesting approach is taken, however, to predetermine structural properties of the surface features and use these properties to define a proprietary code for the respective feature. The respective code is used as key to a hash table with the feature itself as content. In order to increase robustness, each feature is entered several times with slight variation of structural properties and hence a variation in code. Matching features are retrieved from the hash table and verified by point match where rigidity is not assumed.

This section revisited methods of object localisation using both, visual and contact information. The problems of visual object localisation addressed in literature lie in the distance between the sensor and the object and hence in problems like obstruction and calibration, tactile determination of position suffers from the sparsity of data and the adequate representation of the object for this sparse data. Some research has been presented that systematically compares features of a model with detected features during contact.

2.2 Technical Background

This section introduces the notion of technical terms as used in this work. It also revisits some general technical background that is the basis of the following technical chapters.

2.2.1 General Terminology Used in this Work

The following terminology and use of symbols is adopted for the remainder of this thesis. A comprehensive list of symbols, required in later chapters, is given in a table in the beginning. Matrices $\boldsymbol{M}$ are type-set in bold, vectors $\vec{x}$ and vector valued functions $\vec{f}(u)$ are marked by a vector arrow. The symbol $\diamond$ refers to one single index not specified or to an element of a list of indices. Coordinate systems are referred to by $S^{(\diamond)}$ with $(\diamond)$ being the name, referred to in the naming of other coordinate related quantities $\vec{x}^{(\diamond)}$. Subscripts $x_{1,c,ik}$ from left to right first

determine the location in the related vector, here first element, type of variable as c, here for *contact*, and give further parameters ik, here at finger i in contact with facet k.

2.2.2 General Model of Contact

In this section, first some general kinematic definitions are given. For a wider review see [Yos90]. Subsequently, the motion of a body on the surface of another body is described, a key issue in manipulation. This reviews work done by Montana [Mon88, Mon95]. He examines the contact of two general bodies under several different motion constraints. In the context of this work, these bodies in contact are the tips of n robot fingers and an object to be manipulated. Montana's approach is used to describe mathematically the motion of the fingers on the object.

Kinematics of a Robotic Finger

At any point of a finger i, a reference coordinate frame $S^{(f,i)}$ can be attached. Using standard robotic methods, the position $\vec{x}_{f,i}$ and orientation $\vec{\varrho}_{f,i}$ of this reference relative to a general world frame $S^{(w)}$ depend on the kinematic setup and the joint angles $\vec{\theta}_i$ according to

$$\begin{aligned} \vec{x}_{f,i} &= \vec{f}_{f,i}(\vec{\theta}_i) \\ \vec{\varrho}_{f,i} &= \vec{g}_{f,i}(\vec{\theta}_i). \end{aligned} \tag{2.1}$$

The orientation can be represented in any angular representation as roll-pitch-yaw or Euler angles. In the context of this work, the particular representation is irrelevant. Taking the derivatives of (2.1) describes the relation between infinitesimal displacements in $d\vec{\theta}_i$ on the one hand and $d\vec{x}_{f,i}$ and $d\vec{\varrho}_{f,i}$ respectively. Similarly, the velocities of the joints $\dot{\vec{\theta}}_i$ on the one hand and the translational $\dot{\vec{x}}_{f,i}$ and rotational velocity $\dot{\vec{\varrho}}_{f,i}$ of the finger tip are related. The relationship is given as

$$\begin{aligned} \boldsymbol{J}_{x,i} &= d\vec{f}_{f,i}/d\vec{\theta}_i \\ \boldsymbol{J}_{\varrho,i} &= d\vec{g}_{f,i}/d\vec{\theta}_i \\ \dot{\vec{x}}_{f,i} &= d\vec{f}_{f,i}/d\vec{\theta}_i \cdot d\vec{\theta}_i/dt = \boldsymbol{J}_{x,i}(\vec{\theta}_i)\dot{\vec{\theta}}_i \\ \dot{\vec{\varrho}}_{f,i} &= d\vec{g}_{f,i}/d\vec{\theta}_i \cdot d\vec{\theta}_i/dt = \boldsymbol{J}_{\varrho,i}(\vec{\theta}_i)\dot{\vec{\theta}}_i. \end{aligned} \tag{2.2}$$

The matrices $\boldsymbol{J}_{x,i}$ and $\boldsymbol{J}_{\varrho,i}$ are referred to as *(translational) Jacobian* and *rotational Jacobian*. A schematic of the finger and frames is shown in figure 2.12. For a uniform representation of translation and rotation, several possibilities can

be found in literature. One of them is the representation as screws [MLS94] with a translation along and a rotation around a defined screw axis. Other researchers represent translation and rotation as *homogeneous transforms*. These transforms $\boldsymbol{T}_{(B)}^{(A)}$ are 4×4 matrices containing a standard rotation matrix $\boldsymbol{R}_{(B)}^{(A)}$ from system $S^{(A)}$ to system $S^{(B)}$ in the upper left corner and the vector of translation $\vec{t}_{(B)}^{(A)}$ from $S^{(A)}$ to $S^{(B)}$ in the rightmost column as in

$$\boldsymbol{T}_{(B)}^{(A)} = \begin{pmatrix} \boldsymbol{R}_{(B)}^{(A)} & \vec{t}_{(B)}^{(A)} \\ (0,0,0) & 1 \end{pmatrix}. \tag{2.3}$$

In this work, for positions, homogeneous transforms are used. For the ease of notion, in subsequent formulas the transformation of *points* $\vec{x}$ by notion of $\boldsymbol{T}\vec{x}$ is equivalent to $\left[\begin{smallmatrix} 1 & 0 & 0 & 0 \\ 0 & 1 & 0 & 0 \\ 0 & 0 & 1 & 0 \end{smallmatrix}\right] \boldsymbol{T} \left[\vec{x}^T, 1\right]^T$. For transformations of *vectors* the explicit notion is used, however, in order to avoid ambiguities. The position of the finger reference frame $S^{(f,i)}$ is hence described as

$$\boldsymbol{T}_{(w)}^{(f,i)} = \begin{pmatrix} \boldsymbol{R}_{(w)}^{(f,i)}(\vec{\varrho}_{f,i}) & \vec{x}_{f,i} \\ (0,0,0) & 1 \end{pmatrix}. \tag{2.4}$$

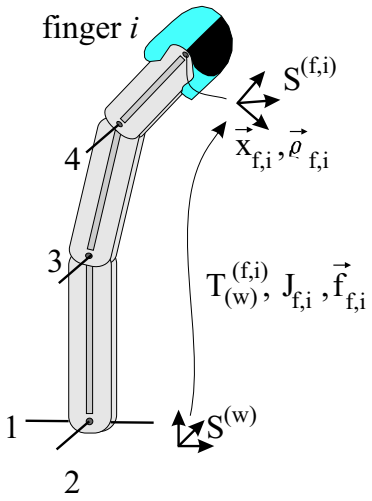

Figure 2.12: Kinematics of a finger

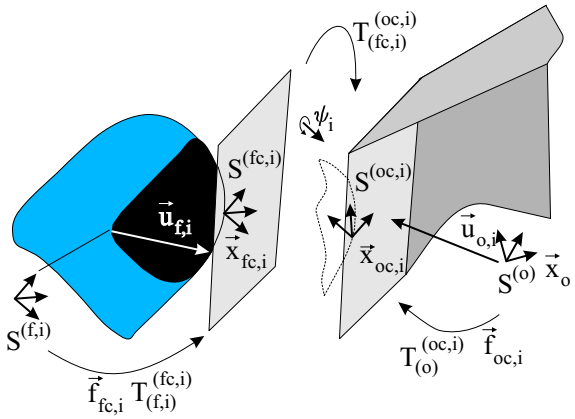

Figure 2.13: Contact kinematics

On the other hand, so called *generalised velocities* as proposed by [MS86] are used: A six-dimensional vector is obtained by combining the translational velocity $\dot{\vec{x}}_{f,i}$ and rotational velocity $\dot{\vec{\varrho}}_{f,i}$ in one vector $\vec{\nu}_i = \left[\dot{\vec{x}}_{f,i}, \dot{\vec{\varrho}}_{f,i}\right]^T$. In the same way, a *generalised finger Jacobian* can be constructed as $\boldsymbol{J}_{f,i} = \begin{bmatrix} \boldsymbol{J}_{x,i} \\ \boldsymbol{J}_{\varrho,i} \end{bmatrix}$.

Coordinate Frames of Contact

In order to describe contact between a finger i and an object, two rigid or quasi-rigid bodies are assumed. These bodies make contact in one distinct point. If the bodies are only quasi-rigid, a representative contact point has to be chosen. If two bodies, however, touch each other at multiple points, e.g. when one of them is concave, each contact has to be treated separately.

For each individual contact, following the methodology of [Mon88, Bro90, Mon95], a reference frame $S^{(o)}$ in the object is defined. This may be located in the object's barycentre. Another reference frame $S^{(f,i)}$ at the finger has already been defined above. This reference frame is usually located in the centre of the finger tip. For both, the fingertip i and the object, a surface description is required. This description is given as a function $\vec{f}_{fc,i}(\vec{u}_{f,i})$ and $\vec{f}_{oc,i}(\vec{u}_{o,i})$ mapping the parameters $\vec{u}_\diamond$ of a two-dimensional parameter-space $I\!R^2$ to the three-dimensional coordinates of the surface in $I\!R^3$. Both functions are defined in their respective base systems $S^{(f,i)}$ and $S^{(o)}$ and parameterised orthogonally by $\vec{u}_{f,i}$ and $\vec{u}_{o,i}$, respectively. The contact between finger i and the object is made at $\vec{x}_{fc,i}$, as seen from the reference point within the finger i, and $\vec{x}_{oc,i}$, as seen from the object's reference point. The vectors $\vec{x}_{fc,i}$ and $\vec{x}_{oc,i}$ refer to the same point in space, only seen from different reference positions. At this point, two *contact frames* $S^{(fc,i)}$ and $S^{(oc,i)}$ can be defined. A schematic of these coordinate systems is shown in figure 2.13. It is to be noted that two surfaces in contact share a common tangential plane. The vectors perpendicular to either surface, and hence orthogonal to the common tangential plane are referred to as *surface normals*. At the point of contact the two normals of both surfaces are anti-parallel, pointing towards the outside of the respective surface. These surface normals are termed $\vec{n}_{fc,i}$ and $\vec{n}_{oc,i}$, respectively. For the contact frames, the basis vector $\vec{e}_{z,\diamond}, \diamond \in \{fc, oc\}$, of the z–axis is defined to be parallel to the respective surface normal. Hence the remaining basis vectors $\vec{e}_{x,\diamond}$ and $\vec{e}_{y,\diamond}$ along the x–and y–axis of $S^{(fc,i)}$ and $S^{(oc,i)}$ span the tangential plane of the surface. They point into the direction corresponding to the first and second parameter $u_{1,\diamond}$ and $u_{2,\diamond}$ and are defined as the partial derivative of the respective surface function $\vec{f}_\diamond$ with respect to the two parameters $u_{1,\diamond}$ and $u_{2,\diamond}$. Hence the contact frames are defined as

$$O^{(\diamond)} = \vec{x}_\diamond = \vec{f}_\diamond(\vec{u}_\diamond) \tag{2.5}$$

$$\begin{aligned}
\vec{e}_{x,\diamond}(\vec{u}_\diamond) &= \frac{\partial \vec{f}_\diamond}{\partial u_{1,\diamond}} / \parallel \frac{\partial \vec{f}_\diamond}{\partial u_{1,\diamond}} \parallel, \\
\vec{e}_{y,\diamond}(\vec{u}_\diamond) &= \frac{\partial \vec{f}_\diamond}{\partial u_{2,\diamond}} / \parallel \frac{\partial \vec{f}_\diamond}{\partial u_{2,\diamond}} \parallel, \\
\vec{e}_{z,\diamond}(\vec{u}_\diamond) &= \vec{e}_{x,\diamond}(\vec{u}_\diamond) \times \vec{e}_{y,\diamond}(\vec{u}_\diamond).
\end{aligned} \tag{2.6}$$

Using equation (2.6), two homogeneous transforms $\boldsymbol{T}_{(f,i)}^{(fc,i)}$ and $\boldsymbol{T}_{(o)}^{(oc,i)}$ from the contact systems $S^{(fc,i)}$ and $S^{(oc,i)}$ to their respective basis systems $S^{(f,i)}$ and $S^{(o)}$ can be defined. These transforms depend on the point of contact, thus on the parameters $\vec{u}_{f,i}$ and $\vec{u}_{o,i}$. These parameters are therefore termed *contact parameters*. A third transform $\boldsymbol{T}_{(fc,i)}^{(oc,i)}$ relates both contact systems $S^{(oc,i)}$ and $S^{(fc,i)}$. By definition, both frames span the common tangential plane at the contact by their $x-$ and $y-$ axes. Hence, this transform depends on the torsion angle ψ_i around the common surface normal measured between the respective x–axes, $\vec{e}_{x,fc,i}$ and $\vec{e}_{x,oc,i}$. The transforms are defined as

$$\begin{aligned}
\boldsymbol{T}_{(f,i)}^{(fc,i)} &= \begin{bmatrix} \vec{e}_{x,fc,i}(\vec{u}_{f,i}) & \vec{e}_{y,fc,i}(\vec{u}_{f,i}) & \vec{e}_{z,fc,i}(\vec{u}_{f,i}) & \vec{f}_{fc,i}(\vec{u}_{f,i}) \\ 0 & 0 & 0 & 1 \end{bmatrix} \\
\boldsymbol{T}_{(o)}^{(oc,i)} &= \begin{bmatrix} \vec{e}_{x,oc,i}(\vec{u}_{o,i}) & \vec{e}_{y,oc,i}(\vec{u}_{o,i}) & \vec{e}_{z,oc,i}(\vec{u}_{o,i}) & \vec{f}_{oc,i}(\vec{u}_{o,i}) \\ 0 & 0 & 0 & 1 \end{bmatrix} \\
\boldsymbol{T}_{(fc,i)}^{(oc,i)} &= \begin{bmatrix} \cos(\psi_i) & -\sin(\psi_i) & 0 & 0 \\ -\sin(\psi_i) & -\cos(\psi_i) & 0 & 0 \\ 0 & 0 & -1 & 0 \\ 0 & 0 & 0 & 1 \end{bmatrix}
\end{aligned} \tag{2.7}$$

The position of the object in coordinates of $S^{(w)}$ can be described as

$$\vec{x}_o^{(w)} = T_{(w)}^{(f,i)} T_{(f,i)}^{(fc,i)} T_{(fc,i)}^{(oc,i)} T_{(oc,i)}^{(o)} [0,0,0,1]^T. \tag{2.8}$$

Kinematics of Contact

The model of contact is feasible for describing stationary relations between two bodies. For a further kinematic investigation of contact, also the generalised velocities $\vec{\nu}_{f,i}$ of the finger i, of the contact point $\vec{\nu}_{c,i}$ and the object $\vec{\nu}_o$ have to be related. At each individual finger i, the generalised velocity $\vec{\nu}_o$ of the object, hence of $S^{(o)}$ with respect to $S^{(w)}$, can be expressed as sum of the velocity of the finger tip $\vec{\nu}_{f,i}$ and the contact velocity $\vec{\nu}_{c,i}$ between finger and object reference point across the contact. This velocity is given in coordinates of $S^{(w)}$ as in

$$\vec{\nu}_o^{(w)} = \vec{\nu}_{f,i}^{(w)} + \beta_2 \left(\boldsymbol{T}_{(w)}^{(f,i)}(\vec{\theta}_i) \boldsymbol{T}_{(f,i)}^{(fc,i)}(\vec{u}_i) \right) \vec{\nu}_{c,i}^{(fc,i)} \tag{2.9}$$

with

$$\begin{aligned}
\vec{u}_i &= [\vec{u}_{f,i}, \psi_i, \vec{u}_{o,i}]^T \\
\beta_2 &: \begin{bmatrix} \boldsymbol{R} & \vec{d} \\ 0 & 1 \end{bmatrix} \rightarrow \begin{bmatrix} \boldsymbol{R} & (*\vec{d})\boldsymbol{R} \\ 0 & \boldsymbol{R} \end{bmatrix} \\
* &: \begin{bmatrix} x \\ y \\ z \end{bmatrix} \rightarrow \begin{bmatrix} 0 & -z & y \\ z & 0 & -x \\ -y & x & 0 \end{bmatrix}
\end{aligned} .$$

In analogy to the Jacobian $\boldsymbol{J}_{f,i}$ of equation (2.2), a contact Jacobian $\boldsymbol{J}_{c,i}$ is defined as

$$\boldsymbol{J}_{c,i}(\vec{\theta}_i, \vec{u}_i) = \beta_2 \left(\boldsymbol{T}^{(f,i)}_{(w)}(\vec{\theta}_i) \boldsymbol{T}^{(fc,i)}_{(f,i)}(\vec{u}_i) \right) \tag{2.10}$$

such that

$$\vec{\nu}^{(w)}_o = \boldsymbol{J}_{f,i}(\vec{\theta}_i)\dot{\vec{\theta}}_i + \boldsymbol{J}_{c,i}(\vec{\theta}_i, \vec{u}_i)\vec{\nu}^{(fc,i)}_{c,i} \tag{2.11}$$

This contact Jacobian transforms velocities from the respective contact frame $S^{(fc,i)}$ to $S^{(w)}$. The vector $\vec{u}_i$ contains the parameters describing the state of the contact, i.e. the contact parameters of either side and the torsion angle between the two contact systems. The adjoint transformation $\beta_2(\boldsymbol{T}^A_B)$ performs a change of coordinates for generalised velocities from system A to system B. It is the inverse of the function γ_2 defined by Montana. The Hodge operator $*$ represents the vector cross product in matrix form as $(*\vec{d})\vec{x} = \vec{d} \times \vec{x}$.

2.2.3 Surface Models of Three-Dimensional Objects

In a later chapter, this work will propose to locate a known, previously modeled object. This is done by comparison of information about the contact points of the finger at the object and a model of the object's surface, briefly called object model. As we have seen from section 2.1.2, measurements from the hand can be obtained either directly by tactile sensors or using algorithms as presented in chapter 3. Usually, from touch only the contact point $\vec{x}_c$ and the corresponding orientation $\vec{n}_c$ of the surface is known. In [JH98] this is termed *oriented point* $\vec{p} = (\vec{x}_c, \vec{n}_c)$. To evaluate these measured oriented points efficiently and compare them to the object model, a reasonable model only has to contain information about possible oriented points on its surface. Also, no global information is required, as the object is only examined locally by contact. This is in contrast to image processing and graphics algorithms that can use more global information about items and hence require more complex models. Here, some major methods to model two dimensional surfaces are revisited.

Cloud of Points

One possibility to specify an object is a cloud of points obtained from sampling over its surface. These data do not contain any information about the interconnection between points nor about the topology, hence the interior or exterior of an object. It consequently is also irrespective of surface normals. This model, however, is the direct output of devices as space scanners, for example the DLR scanner [Sup02], triangulation algorithms in image processing or even exploration

of the surface by a robotic gripper (see sec. 2.1.6). An example of a cloud of points as obtained by DLR's laser scanner is shown in figure 2.14.

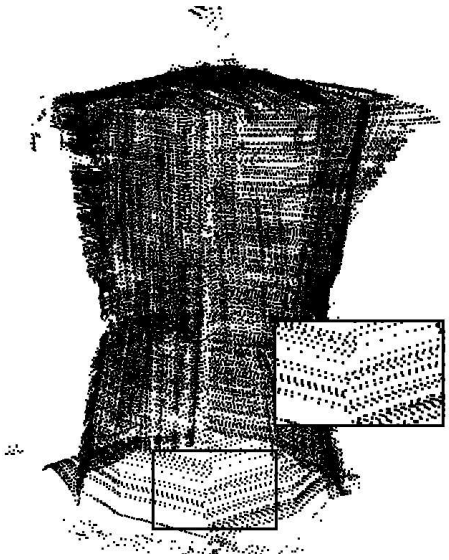

Figure 2.14: Cloud of points of a mocca maker

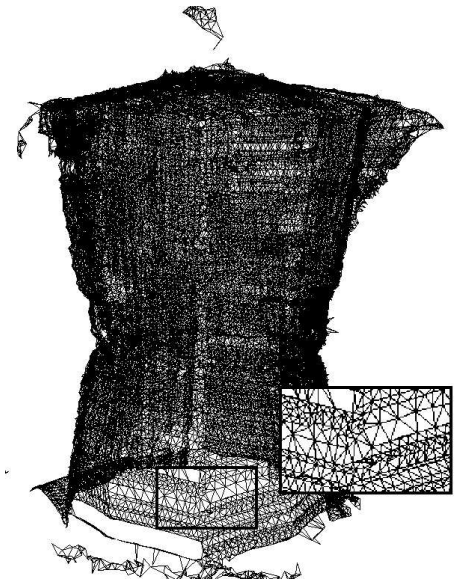

Figure 2.15: Triangulated view of a mocca maker

Polygonal Surfaces

Also, a given surface can be approximated by a set of polygons. The basis of this method has been pursued for decades now and is also known as "winged-edge" description [Bau75]. On the one hand, the polygons can be obtained from design programs and CAD-systems. Originally, this software describes objects as volume models and intersection of three dimensional geometric primitives. Using the export functionality of the programs, the surface can be sampled and polygons can be constructed. On the other hand, clouds of points from input devices can also be approximated by polygons. This format of description is also used for example by software as OpenGL and OpenInventor.

The polygon is represented by its vertices $\vec{x}_s$ and edges, the first being ordered in a right hand sense. This way the surface normal is defined pointing outwards of the object orthogonal to the polygon. Often, triangles are used as polygonal primitives. The model obtained by a polygonal representation is local in its nature and linearly approximates the object. It may be provided for the whole object or only for a parts. The surface normals are also contained in the description, however, the curvature of the object is disregarded. For general items this description

is thus non-smooth at the edges of each polygon. The previous example from figure 2.14 has been triangulated and is shown in figure 2.15. For mesh processing and optimisation, a number of algorithms exist, e.g. to adjust sampling at places where higher resolution is required like at edges, and reduce sampling at almost planar spots [AMD02].

Bézier, Splines, NURBS, Subdivision

When information about curvature is also desirable or a continuous surface is required modeling can be done using interpolating algorithms [She02]. These descriptions approximate or interpolate a surface given by a cloud of points using these points as control points. The idea is to represent the surface as a sum of basis functions at the control points.

In Bézier algorithms, each basis function corresponds to one control point. Each point influences the whole surface.

Splines are a generalisation of Bézier surfaces. They also use knot points, which divide a surface into independent Bézier surfaces. The basis functions influence only a limited region of the surface. An extension of splines are non-uniform rational B-splines (NURBS), which use generalised basis functions.

A further generalisation of splines is known as subdivision [ZS$^+$00]. Here a surface consisting of control points is subdivided into smaller segments resulting in a smoother surface. The technique is equivalent to refinement of a spline surface. This is mostly used in graphical animation and movies, as only the much sparser initial control points have to be animated but a smooth object can be rendered. With object models as presented here, continuous, differentiable surfaces can be obtained.

Implicit Surfaces

Finally, an object's surface can be represented as the iso-surface of value r of a describing function $F(x, y, z)$ as $F(x, y, z) - r = 0$. This is analogous to describing a circle in 2 dimensions by the implicit function $x^2 + y^2 - r^2 = 0$. A combination of simple surfaces, e.g. spheres, can be used to construct more complex objects [OM00]. This technique is mostly used in computer simulation and to visualise deformable material.

Chapter 3

Determination of Finger Contact Point

When grasping an object with a robotic gripper, as has been explained in chapter 1.2, the exact contact position between a finger and the object is required. This contact position can be expressed as a three-dimensional point in the common reference system $S^{(w)}$ or relative to the finger tip position $S^{(f,i)}$ as a two-dimensional point on the surface of the finger (see chapter 2.2.2). In the first case, the contact point also locates the surface of the grasped object and hence allows more sensitive grasping and manipulation (see chapter 2.1.3). In the second case, knowledge

Figure 3.1: Chalk marks after touching an object

of the contact point on the surface description of the finger allows the determination of the contact normal. Additional contact parameters such as curvature can be obtained by exploration schemes. Knowledge about the surface features allows more sophisticated object handling, e.g. rolling or intentional sliding.

An a-posteriori method of determining the contact point on the surface of the finger tip is depicted in figure 3.1. Before grasping an object, its surface was rubbed with white chalk. After grasping, the chalk marks represent the position

of contact and can be measured. For different sensor instrumentations in robotic grippers, this chapter presents two methods to determine the point of contact online during grasping. On the one hand, in simple grippers sometimes the only available sensors are position resolvers. For those cases, section 3.1 proposes an algorithm to determine the contact point from position and velocity measurements. For cases where a second approach is desired or more sophisticated hands with sensitive force/torque sensors are being used, in section 3.2 these sensors are used in an optimisation method to estimate the contact point and forces acting at this position.

3.1 Contact Positions From Kinematic Constraints

One of the most vital pieces of information for grasping with robotic hands is the point of contact, as seen above. In numerous robotic hands, however, direct determination through tactile measurements or indirect computation by grasping force/torque evaluation is not possible due to the lack of good enough sensors. For those cases, this section presents an algorithm to determine the position of contact between fingers and object on the finger surface using position and velocity measurements of the finger joints. In cases where no velocity sensors are present, the numerical derivative of the position can be computed giving an approximation of the actual joint velocity. Position sensors are widely available and always used in robotic grippers for position control (see section 2.1.2). The concept to be presented here borrows from an observation when multiple fingers simultaneously grasp an object. Depending on the type of contact, the motion of the object determines the motion of the individual fingers (see figure 3.2). The fingers can only

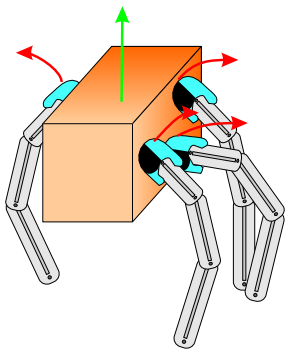

Figure 3.2: Combined motion of object and fingers

slide or roll along the surface of the object in order to maintain the constraints imposed upon them for a stable contact. On both surfaces, object and fingers, this

motion causes a rolling or sliding path. The trajectory of motion along the tip's surfaces is determined by the initial contact position and the motion of the object. This promotes the idea of first evaluating the combined motion of the fingers and then reconstructing the motion of the object and the initial position of the contact point of the individual fingers. Other researchers also examined the use of non-tactile and non force/torque sensors for the computation of the contact point (see chapter 2.1.6). To the author's knowledge, the algorithm presented here is the only one that does not require particular exploratory motions or a specialised setup and can be used in full generality for any type of contact on the fly. As a basis for the algorithm developed here a contact model describing motion between two bodies in contact is needed. This model has been introduced in section 2.2.2. The model will be reinterpreted for this new concept in section 3.1.1. This interpretation is then evaluated in an optimisation procedure in section 3.1.3. The parameters of the minimisation are the desired contact positions on the surface of the fingertip. In scenarios with a continuous stream of measurements, the parameters can also be observed. This observation is presented in section 3.1.4. This section is concluded with numerical examinations and simulation runs performed with both algorithms presented in sections 3.1.5 and 3.1.6.

3.1.1 Interpretation of the Kinematics of Contact

In chapter 2.2.2 a general kinematic model of contact was introduced. As was presented in equation (2.11), the velocity of an object in contact with a finger, can be expressed as sum of two velocity components. Those two components form two serial kinematic chains as depicted in figure 3.4. In the first chain,

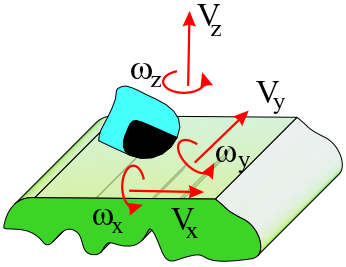

Figure 3.3: Components of contact velocity $\vec{\nu}_c = [\vec{v}_c^T; \vec{\omega}_c^T]^T$

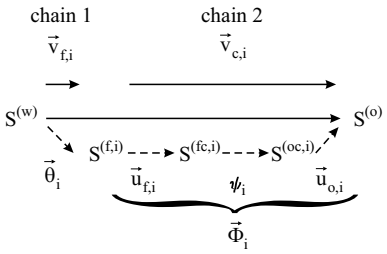

Figure 3.4: Kinematic chains

the generalised velocity $\vec{\nu}_{f,i}^{(w)}$ of the reference point of finger i is computed and expressed in $S^{(w)}$. In the second chain, the contact velocity $\vec{\nu}_{c,i}$ relates the two systems $S^{(f,i)}$ and $S^{(o)}$. This second chain consists of three subchains linking $S^{(f,i)}$ with $S^{(fc,i)}$, $S^{(fc,i)}$ with $S^{(oc,i)}$ and $S^{(oc,i)}$ with $S^{(o)}$. The first chain is controlled

by the two kinematic functions $\vec{f}_{x,i}(\vec{\theta}_i)$ and $\vec{f}_{\varrho,i}(\vec{\theta}_i)$ of the reference point $\vec{x}_{f,i}$ of finger i, the parameters of these functions, namely joint angles $\vec{\theta}_i$, and their respective velocity $\dot{\vec{\theta}}_i$. Usually the kinematic functions of robotic grippers are known. Also joint angle measurements are required for any kind of joint control. Thus these angles are known. As mentioned before only the joint velocities might not be measurable, but can usually be computed from position readings. Hence, the first chain is completely determined in this context. In the second chain, the first part depends on the geometry $\vec{f}_{fc,i}(\vec{u}_{f,i})$ of the finger tip's surface, the contact parameters $\vec{u}_{f,i}$ of the finger's surface and third on their derivative $\dot{\vec{u}}_{f,i}$. Usually only the geometry function $\vec{f}_{fc,i}$ is known from hand design. For the algorithm presented in this section, no tactile or applicable fore/torque sensors are available. Hence neither the contact parameters $\vec{u}_{f,i}$ nor their derivatives are measurable. The second part depends on the twist ψ_i between the two surfaces and its derivative. These variables are not even detectable with tactile information. The third part depends on the geometry $\vec{f}_{oc,i}(\vec{u}_{o,i})$ of the object, the contact parameters $\vec{u}_{o,i}$ of the object and their derivatives $\dot{\vec{u}}_{o,i}$. In the context of this chapter, the geometry of the object is not required. The contact parameters $\vec{u}_{o,i}$ of the object and their derivatives are not measurable without particular setups like tactile sensors on the object. Obviously, the second kinematic chain gathers a part of the velocity chain that is not directly measurable. The analogy between the two chains suggests interpretation of the second chain as another joint. This joint has five degrees of freedom. The contact parameters $\vec{u}_i = [\vec{u}_{f,i}; \psi_i; \vec{u}_{o,i}]^T$ can be regarded as joint angles.

This chapter is focussed on the computation of the position and motion, hence the velocity, of the contact point $\vec{x}_{fc,i}$ on the side of the finger or equivalently $\vec{x}_{oc,i}$ on the side of the object. Recalling equation (2.8)

$$\vec{x}_o^{(w)} = T_{(w)}^{(f,i)} T_{(f,i)}^{(fc,i)} T_{(fc,i)}^{(oc,i)} T_{(oc,i)}^{(o)} [0,0,0,1]^T,$$

this equation can be reordered as

$$\begin{aligned} \vec{x}_{\diamond,i}^{(w)} = & \\ & \vec{x}_o^{(w)} - T_{(w)}^{(f,i)}(\vec{\theta}_i) T_{(f,i)}^{(fc,i)}(\vec{u}_{f,i}) T_{(fc,i)}^{(oc,i)}(\psi_i) T_{(oc,o)}^{(o)}(\vec{u}_{o,i}) [\vec{f}_{oc,i}, 0]^T = \\ & \vec{f}_{x,i} + T_{(w)}^{(f,i)}(\vec{\theta}_i) [\vec{f}_{fc,i}, 0]^T, \end{aligned} \tag{3.1}$$

the Cartesian position of the contact point $\vec{x}_\diamond, \diamond \in \{fc, oc\}$, can be determined. This represents an observation of the kinematic chain after the first joint of the second subchain. The third part of this equation contains measurable quantities and solely the two unknown *contact parameters*, $\vec{u}_{f,i}$ on the side of the finger.

Hence this part is preferred for computation of the contact point. Similarly, equation (2.11)

$$\vec{\nu}_o^{(w)} = \boldsymbol{J}_{f,i}(\vec{\theta}_i)\dot{\vec{\theta}}_i + \boldsymbol{J}_{c,i}(\vec{\theta}_i, \vec{u}_i)\vec{\nu}_{c,i}^{(fc,i)}$$

is revisited. The relative velocity $\vec{\nu}_{c,i}$ between $S^{(f,i)}$ and $S^{(o)}$ can be introduced to compute the velocity of the object in the common world frame $S^{(w)}$. Hence, the object velocity depends on measurable quantities and the velocity $\vec{\nu}_{c,i}$ as new unknown variable additionally to the same two unknown contact parameters, $\vec{u}_{f,i}$ as required in equation (3.1). This way, equation (2.11) can be rewritten as

$$\vec{\nu}_o^{(w)} = \boldsymbol{J}_{f,i}(\vec{\theta}_i)\dot{\vec{\theta}}_i + \boldsymbol{J}_{c,i}(\vec{\theta}_i, \vec{u}_{f,i})\vec{\nu}_{c,i}^{(fc,i)}. \tag{3.2}$$

The velocity $\vec{\nu}_{c,i}$ itself, however, depends on all contact parameters velocities $\dot{\vec{u}}_i$ according to

$$\vec{\nu}_{c,i} = \boldsymbol{J}_{u,i}(\vec{u}_i)\dot{\vec{u}}_i. \tag{3.3}$$

For a definition of the contact parameter Jacobian $\boldsymbol{J}_{u,i}$ refer to [Mon88]. The introduction of the six-dimensional relative velocity $\vec{\nu}_{c,i}$ has advantages over the obvious use of the five-dimensional contact parameter velocities $\dot{\vec{u}}_i$ to be explained here. Naturally, all admissible $\vec{\nu}_{c,i}$ cannot really span $\mathbb{R}^6$ as its dimension would suggest, because it describes the motion of a joint with only five degrees of freedom, which can at best only span $\mathbb{R}^5$. Additionally, the motion of a finger i grasping an object is constrained in order to maintain a stable contact with the item. The type of contact, e.g. a soft finger touching a rigid body, determines those constraints and produces conditions on the admissible velocities at the contact, e.g. rolling along the surface. These conditions can most intuitively be formulated in terms of the contact velocity $\vec{\nu}_{c,i}$ (see figure 3.3). Depending on the contact, a number g of the components of $\vec{\nu}_{c,i} = [v_{x,i}; v_{y,i}; v_{z,i}; \omega_{x,i}; \omega_{y,i}; \omega_{z,i}]^T$ have to be 0. Although theoretically any number g is possible, only a few combinations represent usual types of contact. A value of $g = 6$ represents the totally glued contact. A value of $g = 0$ corresponds to no contact at all. In order to keep in touch with each other, two surfaces have to at least be constrained to $v_{z,i} = 0$, i.e. no lift off is allowed. On the other hand, constraints in the tangential directions of e_x and e_y are usually active simultaneously. Thus the next possible number $g = 3$ corresponds to rolling with twist by $v_{z,i} = v_{x,i} = v_{y,i} = 0$ or sliding with twist $v_{z,i} = \omega_{x,i} = \omega_{y,i} = 0$. The first case matches many real cases, where the finger tips are sometimes rather hard, such that twist is not alway inhibited. The latter case corresponds to the motion of a planar body, e.g. a cube, on a slippery surface. With $g = 4$ two cases are possible. A plain sliding contact is characterised

g	conditions	description
0	-	no contact
1	$v_{z,i} = 0$	rolling and sliding with twist
2	$v_{z,i} = \omega_{z,i} = 0$	plain rolling and sliding
3	$v_{z,i} = \omega_{x,i} = \omega_{y,i} = 0$	sliding with twist
3	$v_{z,i} = v_{x,i} = v_{y,i} = 0$	rolling with twist
4	$v_{z,i} = \omega_{z,i} = \omega_{x,i} = \omega_{y,i} = 0$	plain sliding
4	$v_{z,i} = v_{x,i} = v_{y,i} = \omega_{z,i} = 0$	plain rolling
5	$v_{z,i} = v_{x,i} = v_{y,i} = \omega_{x,i} = \omega_{y,i} = 0$	not meaningful
6	$v_{z,i} = v_{x,i} = v_{y,i} = \omega_{z,i} = \omega_{x,i} = \omega_{y,i} = 0$	fixed contact

Table 3.1: Conditions on the contact velocity $\vec{\nu}_c$

by $v_{z,i} = \omega_{z,i} = \omega_{x,i} = \omega_{y,i} = 0$, and plain rolling by $v_{z,i} = \omega_{z,i} = v_{x,i} = v_{y,i} = 0$. The first case corresponds to two planar bodies in contact with sufficient friction to prevent twist. The plain rolling case matches a contact model of two rigid bodies with high torsional friction, as happens if the contact is obtained on a contact centroid [BSB93]. For $g = 5$ all but the twist constraint have to be active due to symmetry and to prevent lift off $v_{z,i} = v_{x,i} = v_{y,i} = \omega_{x,i} = \omega_{y,i} = 0$. This case, however, is hard to match to a real setup, as are non-symmetric cases. For a more comprehensive overview see table 3.1. The two cases of plain rolling and rolling with twist are encountered most often in grasping and thus serve as reference cases in the following discussions.

3.1.2 Solving for Unknown Contact Joint Angles

In this section, a system of equations is derived from equation (3.2) in order to solve for the unknown $\vec{u}_{fc,i}$ and $\vec{\nu}_{c,i}$. The guiding idea behind this new system of equations is that, in n-fingered grasps, the unknown object speed $\vec{\nu}_o$ can be computed using any of the n fingers. This produces n equations for $\vec{\nu}_o$. Since we are not interested in the velocity of the object on the first place, $\vec{\nu}_o$ can be eliminated. This is equivalent to closing a loop of velocities over any two fingers i and j as depicted in figure 3.5.

This loop follows the way from system $S^{(w)}$ via $S^{(f,i)}$, $S^{(o)}$, $S^{(f,k)}$ back to $S^{(w)}$, marked red in the figure. With initially n equations, $n-1$ independent loops can be closed choosing one finger, e.g. finger 1 as reference finger. This results in

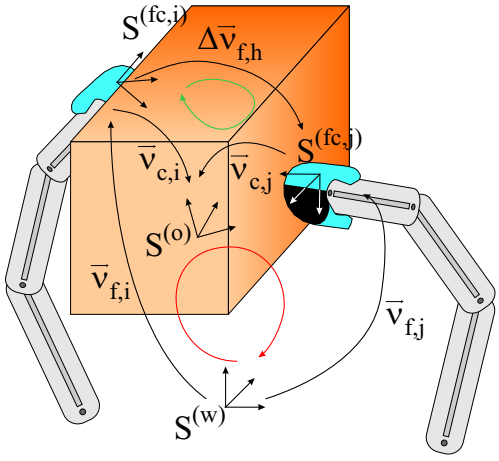

Figure 3.5: Loop of velocities

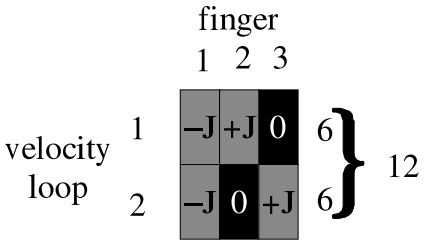

Figure 3.6: Structure of $\boldsymbol{J}_{c,h}$ and $-\boldsymbol{J}_{f,h}$

a set of equations

$$\begin{aligned} 0 \;=\; & \boldsymbol{J}_{f,1}(\vec{\theta}_1)\dot{\vec{\theta}}_1 + \boldsymbol{J}_{c,1}(\vec{\theta}_1, \vec{u}_{f,1})\vec{\nu}_{c,1}^{(fc,1)} - \\ & \boldsymbol{J}_{f,i}(\vec{\theta}_i)\dot{\vec{\theta}}_i - \boldsymbol{J}_{c,i}(\vec{\theta}_i, \vec{u}_{f,i})\vec{\nu}_{c,i}^{(fc,i)} \\ & \text{with } 1 < i \leq n. \end{aligned} \tag{3.4}$$

Now, terms depending on the unknown contact joint parameters $\vec{u}_{f,i}$ and contact velocity $\vec{\nu}_{c,i}^{(fc,i)}$ are brought on one side. All $n-1$ equations are then stacked, forming the vector equation

$$\boldsymbol{J}_{f,h}(\vec{\theta}_h)\dot{\vec{\theta}}_h \;=\; \boldsymbol{J}_{c,h}(\vec{u}_{f,h})\vec{\nu}_{c,h} \tag{3.5}$$

$$\Delta\vec{\nu}_{f,h} \;=\; \boldsymbol{J}_{f,h}(\vec{\theta}_h)\dot{\vec{\theta}}_h, \tag{3.6}$$

where $\vec{\nu}_{c,h} = [v_{c,1}, ...v_{c,n}]^T$, $\vec{\theta}_h$, $\dot{\vec{\theta}}_h$ and $\vec{u}_{f,h}$ are defined analogously. For the Jacobian matrices $\boldsymbol{J}_{f,i}$ and $\boldsymbol{J}_{c,i}$ respective hand Jacobians $\boldsymbol{J}_{f,h}$ and $\boldsymbol{J}_{c,h}$ are formed as block matrices containing the respective matrices of each finger assembled as depicted in figure 3.6 for the three finger case. The measured vector $\Delta\vec{\nu}_{f,h}$ represents the finger velocity of finger i relative to the reference finger 1, as coloured green in figure 3.5. In the n finger case, equation (3.5) represents a set of $6(n-1)$ equations with $6n$ unknown contact velocities $\vec{\nu}_{c,h}$ and $2n$ unknown contact joint parameters $\vec{u}_{f,h}$. As discussed above, for a given contact type all possible $\vec{\nu}_{c,h}$ only span a subspace of $\mathbb{R}^{6n}$. The g contact conditions constrain $\vec{\nu}_{c,h}$ to this subspace and render ng additional equations. This is in the plain rolling case $4n$ and in the case allowing twist $3n$. Incorporating the contact conditions into equation

(3.5), $\vec{\nu}_{c,h}$ can be reduced to its non–zero components $\vec{\tilde{\nu}}_{c,h}$ and $\boldsymbol{J}_{c,h}$ is adjusted appropriately as $\tilde{\boldsymbol{J}}_{c,h}$. In order to compute the contact joint angles $\vec{u}_{f,i}$, equation (3.5) has to be solved for $\vec{\tilde{\nu}}_{c,h}$ and $\vec{u}_{f,h}$. The adjusted system of equation (3.5) then represents a set of $6(n-1)$ equations in $(6-g)n+2n$ unknowns.

The contact parameters $\vec{u}_{f,i}$ describe the position of contact on the surface of the finger tip. In the model discussed above, they resemble joint angles of a kinematic chain. In both views, in a dynamical sense $\vec{u}_{f,i}$ has to be considered a state variable, which cannot perform jumps over time unless the contact velocity or joint velocity becoming infinite. Thus, when small finger movements are performed, the contact velocity is also small and the contact parameters $\vec{u}_{f,h}$ vary only little. Hence, when performing this motion sufficiently slowly or returning to a sample configuration and probing different motions, it is possible to obtain several measurements of $\vec{\nu}_{f,h}$ with $\vec{u}_{f,h}$ being constant or close to constant. On the other hand, in section 3.1.4 a method is presented to estimate an evolving $\vec{u}_{f,h}$ and thus to be able to determine the contact joint angles to later points in time when their initial value is known. Each additional new measurement adds $6(n-1)$ equations and $(6-g)n$ unknowns since the $2n$ values of $\vec{u}_{f,h}$ are identical over all measurements or their evolution can be predicted.

Examining equation (3.5) further, it can be seen that the measurement $\Delta\vec{\nu}_{f,h}$ depends linearly on $\vec{\tilde{\nu}}_{c,h}$ when $\vec{u}_{f,h}$ is known, whereas it depends nonlinearly on $\vec{u}_{f,h}$. This linear/non-linear structure of unknowns in combination with the state-like behaviour of the contact parameters suggests that, for the solvability of equation (3.5), there exist three different cases:

- First, the system is completely solvable or even over-determined in all, linearly and nonlinearly dependent unknowns with even one measurement. This happens if the number of contact constraints g is high.

- Second, with the evolution of $\vec{u}_{f,h}$ being known or constant, the system becomes over-determined in the rapidly-varying linearly-dependent $\vec{\tilde{\nu}}_{c,h}$. Each measurement is under-determined alone, however, several consecutive measurements can be combined, and the multi-measurement system even becomes over-determined.

- Third, too little information is obtained in each new sample even with the evolution of $\vec{u}_{f,h}$ being known or constant. Also, with an arbitrarily large number of samples, it is not possible to solve the multi-measurement system of equations.

The three cases are summarised in table 3.2 along with examples for a 3-fingered setup and a scenario of rolling with twist, which in the remainder of this thesis is the sample setup. In common dextrous manipulation setups, usually case 2 is

case	condition	description	$n = 3$	$g = 3$
1	$g\ n \geq 6 + 2n$	generally (over-) determined	$g \geq 4$	$n \geq 6$
2	$6 < g\ n < 6 + 2n$	over-determined in $\vec{\tilde{\nu}}_{c,h}$	$g = 3$	$2 < n < 6$
3	$6 \geq g\ n$	generally under-determined	$g \leq 2$	$n \leq 2$

Table 3.2: Solvability of the contact equation

achieved. Case 1 can be seen as special case of case 2 and be treated equivalently. Case 3 can not usually be achieved, due to the small number of fingers and motion constraints. The most general case 2 is therefore investigated here.

3.1.3 Formulation as Optimisation Problem

The interpretation given above can be applied using several measurements to solve for the $\vec{u}_{f,h}$ and $\vec{\tilde{\nu}}_{c,h}$. In the next section, a theoretical approach is derived followed by a numerical algorithm, performing the steps proposed in a numerically-efficient way.

Theoretical Approach

Considering case 2 of table 3.2, it is possible to interpret equation (3.5) as a linear mapping $\Gamma(\vec{u}_{f,h}) = \tilde{\boldsymbol{J}}_{c,h}(\vec{u}_{f,h})$ from the space $\mathcal{C} = I\!R^{(6-g)n}$ of reduced contact velocities $\vec{\tilde{\nu}}_{c,h}$ to the space $\mathcal{F} = I\!R^{6(n-1)}$ of relative finger velocities $\Delta\vec{\nu}_{f,h}$ [1]. This linear mapping depends on the contact joint angles $\vec{u}_{f,h}$. Obviously, the map is not surjective since $\dim(\mathcal{F}) > \dim(\mathcal{C})$. According to [Str80], the mapping Γ has a range $\mathcal{R} = \mathrm{range}(\Gamma)$ which is the column space of $\tilde{\boldsymbol{J}}_{c,h}$ and a left nullspace $\mathcal{L} = \{\nu | \nu \in \mathcal{F} \wedge \nu \perp \mathcal{R}\}$, which is not reachable from $\mathcal{C}$ through Γ. With the scalar product being defined as discussed, the left nullspace is the orthogonal complement of $\mathrm{range}(\Gamma)$ in $\mathcal{F}$.

Since Γ is not surjective, the inverse map from the space $\mathcal{F}$ of relative finger velocities to the space $\mathcal{C}$ of contact velocities is not unique. Those finger velocities $\Delta\vec{\nu}_{f,h}$ that are contained in $\mathrm{range}(\Gamma)$ have a directly corresponding contact velocity $\vec{\tilde{\nu}}_{c,h}$ in $\mathcal{C}$. For any other vector $\Delta\vec{\nu}_{f,h}$ that contact velocity vector $\vec{\tilde{\nu}}_{c,h}$ in

[1] In a strict sense, the generalised velocities $\Delta\vec{\nu}_{f,h}$ and $\vec{\tilde{\nu}}_{c,h}$ contain different types of variables, namely translational and rotational velocities. Hence they do not represent a Euclidean space which is required for later derivations. However, by introducing a relation between rotational and translational velocities, a scalar product can be introduced. One possible relation for rotational velocities is the translational velocity which the rotation would cause in a typical distance. This can be considered as weighting rotations by an appropriate factor. In following formulas, this weighting is omitted for ease of notion.

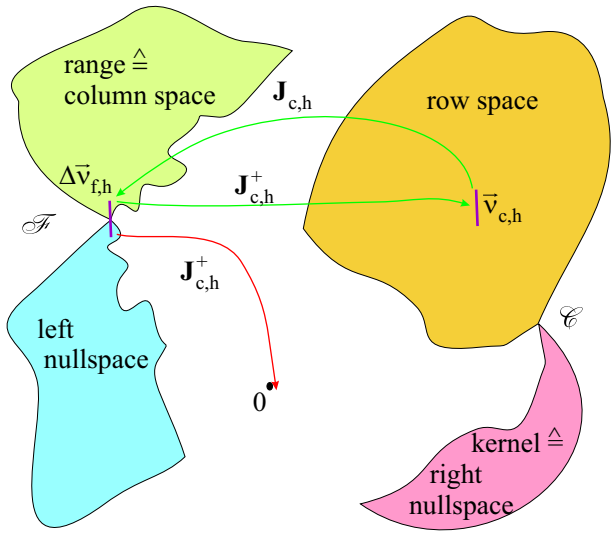

Figure 3.7: Mappings of the contact Jacobian

$\mathcal{C}$ can be chosen, whose correspondence in $\mathcal{F}$ is closest to the measured velocity $\Delta\vec{\nu}_{f,h}$. This represents an inverse map Γ^{-1} from $\mathcal{F}$ to $\mathcal{C}$ using the known left pseudo-inverse $\tilde{\boldsymbol{J}}^{+}_{c,h}$. For those vectors $\Delta\vec{\nu}_{f,h}$ not in $\mathrm{range}(\Gamma)$, this pseudo-inverse returns the best possible estimate $\hat{\vec{v}}_{c,h}$ in the sense of least squares [2]. Both mappings are shown in figure 3.7. The mappings depend on the unknown contact joint parameters $\vec{u}_{f,h}$.

Assume for the instance that a good value $\hat{\vec{u}}_{f,h}$ for $\vec{u}_{f,h}$ can be estimated. With a perfect estimate, a measured relative velocity $\Delta\vec{\nu}_{f,h}$ would lie totally in the subspace $\mathcal{R}$ of $\mathcal{F}$. As illustrated in figure 3.7, with an imperfect estimate $\hat{\vec{u}}_{f,h}$, a measured $\Delta\vec{\nu}_{f,h}$ is a linear combination of either of the two subspace of $\mathcal{F}$. The better the initial estimate of $\vec{u}_{f,h}$ is, i.e. the more the estimate represents the true values, the smaller the component parallel to $\mathcal{L}$ will be. When mapping $\Delta\vec{\nu}_{f,h}$ to $\mathcal{C}$, its components parallel to $\mathcal{L}$ are projected to 0. These are the components that result from a false estimate of $\vec{u}_{f,h}$ and cause an error to occur in the least squares fit of $\tilde{\boldsymbol{J}}^{+}_{c,h}$. The components of $\Delta\vec{\nu}_{f,h}$ parallel to the range space $\mathcal{R}$ of Γ are mapped to its unique pre-image $\hat{\vec{\nu}}_{c,h}$ in $\mathcal{C}$. Projecting $\hat{\vec{\nu}}_{c,h}$ back to $\mathcal{F}$ will give those components of $\Delta\vec{\nu}_{f,h}$ parallel to the range space $\mathcal{R}$. With this result, the

[2] In general cases, a map Γ can also have a right nullspace, the kernel, being the orthogonal complement to the row space. In this scenario, however, this would mean that there exist $\hat{\vec{v}}_{c,h}$ which cannot be caused by any $\Delta\vec{\nu}_{f,h}$. Practically, a motion of the object is possible, which cannot be controlled by the motion of the fingers, hence this grasp is not stable. These grasps are irregular and not investigated further here.

components of $\Delta\vec{\nu}_{f,h}$ parallel to the nullspace $\mathcal{L}$ can be computed as

$$\vec{\eta}_{f,h}(\vec{\hat{u}}_{f,h}, \Delta\vec{\nu}_{f,h}) = \Delta\vec{\nu}_{f,h} - \tilde{\boldsymbol{J}}_{c,h}\tilde{\boldsymbol{J}}^{+}_{c,h}\Delta\vec{\nu}_{f,h}. \tag{3.7}$$

As stated, in a properly estimated, theoretically exact setup, an undisturbed measurement $\Delta\vec{\nu}_{f,h}$ lies in the range space $\mathcal{R}$ and the mapping Γ^{-1} is bijective for the subspace of possible actual measurements $\Delta\vec{\nu}_{f,h}$. Therefore $\vec{\eta}_{f,h} = \vec{0}$. Taking the norm of $\vec{\eta}_{f,h}$ renders a scalar measure ξ_1 for this inconsistency of the mapping Γ^{-1}. Since the mappings Γ and Γ^{-1} depend on the estimate of contact joint parameters $\vec{\hat{u}}_{f,h}$, so does $\vec{\eta}_{f,h}$ and consequently ξ_1 according to

$$\xi_1(\vec{\hat{u}}_{f,h}, \Delta\vec{\nu}_{f,h}) = \vec{\eta}^{\,T}_{f,h}(\vec{\hat{u}}_{f,h}, \Delta\vec{\nu}_{f,h})\vec{\eta}_{f,h}(\vec{\hat{u}}_{f,h}, \Delta\vec{\nu}_{f,h}). \tag{3.8}$$

With m different measurements of $\Delta\vec{\nu}_{f,h}$, it is possible to solve not only for $\vec{\hat{v}}_{c,h}$ by

$$\vec{\hat{v}}_{c,h} = \tilde{\boldsymbol{J}}^{+}_{c,h}\Delta\vec{\nu}_{f,h}, \tag{3.9}$$

but also get a better estimate $\vec{\hat{u}}_{f,h}$ for $\vec{u}_{f,h}$ by minimising ξ_1 over $\vec{u}_{f,h}$:

$$\vec{\hat{u}}_{f,h} = \arg(\min_{\vec{u}_{f,h}}(\xi_m(\vec{u}_{f,h}))) = \arg(\min_{\vec{u}_{f,h}} \sum_{i=1}^{m} \xi_1(\vec{u}_{f,h}, \Delta\vec{\nu}_{f,h,i})). \tag{3.10}$$

As shown above, several measurements are always required. As numerical examinations also show, one single measurement only causes significant errors ξ_1 along a particular direction of $\vec{u}_{f,i}$, whereas in other directions ξ_1 varies only little. This is obvious, as movement along the surface of the finger tip is always along a one dimensional line on a two dimensional surface. The direction orthogonal to the direction of motion is not explored. Now, with estimates of the contact joint angle $\vec{\hat{u}}_{f,i}$ and the contact velocity $\hat{\vec{\nu}}_{c,i}$, the desired contact point $\vec{x}_{fc,i}$ and the surface normal $\vec{n}_{fc,i}$ can be retrieved as exteroceptive information of position sensors. In the consequence, also the object velocity $\vec{\nu}_o$ can be computed:

$$\begin{aligned}
\vec{x}_{fc,i} &= \boldsymbol{T}^{(f,i)}_{(w)}(\vec{\theta}_i)\vec{f}_{f,i}(\hat{\vec{u}}_{f,i}) \\
\vec{n}_{fc,i} &= \boldsymbol{T}^{(f,i)}_{(w)}(\vec{\theta}_i)\boldsymbol{T}^{(fc,i)}_{(f,i)}(\hat{\vec{u}}_{f,i})\,[0,0,1,0]^T \\
\vec{\nu}_o &= \boldsymbol{J}_{f,i}(\vec{\theta}_i)\dot{\vec{\theta}}_i + \boldsymbol{J}_{c,i}(\vec{\theta}_i, \vec{u}_i)\hat{\vec{\nu}}_{c,i}
\end{aligned} \tag{3.11}$$

Improved Algorithm for Optimisation

Performing a tracking of the contact joint angles as presented above in equation (3.10) is computationally costly. For each step of a chosen minimisation algorithm, the pseudo-inverse $\tilde{\boldsymbol{J}}^{+}_{c,h}$ has to be computed anew. This is an unnecessary

effort, since $\tilde{\boldsymbol{J}}^{+}_{c,h}$ is only needed once for the projection. The idea of the algorithm presented in 3.1.3 is to compute the norm of the components of a measurement $\Delta\vec{\nu}_{f,h}$ in the left nullspace $\mathcal{L}$ of $\tilde{\boldsymbol{J}}_{c,h}$. This is basically the same idea underlying the Gram-Schmidt orthogonalisation [Str80]. In this method, an ordered set $\boldsymbol{Q}$ of vectors $\vec{q}$ is orthogonalised recursively as a whole. From each vector $\vec{q}_b$, those components are subtracted that are parallel to any already orthogonalised vector $\vec{q}_c, c < b$ earlier in the set according to

$$(\vec{q}\,^{c}_{b})(\boldsymbol{Q}) = (\vec{q}\,^{c-1}_{b}) - \frac{(\vec{q}\,^{c-1}_{c})^T(\vec{q}\,^{c-1}_{b})}{(\vec{q}\,^{c-1}_{c})^T(\vec{q}\,^{c-1}_{c})}(\vec{q}\,^{c-1}_{c}), \tag{3.12}$$

where $\vec{q}\,^{c}_{b}(\boldsymbol{Q})$ means that from the b^{th} vector all components parallel to all predecessors in the set $\boldsymbol{Q}$ up to the c^{th} vector have been subtracted. Using the latter algorithm, the function $\vec{\eta}_{f,h}$ can be rewritten. In order to compute the component of $\Delta\vec{\nu}_{f,h}$ being in the nullspace of $\tilde{\boldsymbol{J}}_{c,h}$ and hence being orthogonal to the the range space $\mathcal{R}$ of $\tilde{\boldsymbol{J}}_{c,h}$, one can use

$$\vec{\eta}(\vec{\hat{u}}_{f,h}, \Delta\vec{\nu}_{f,h}) = \vec{q}\,^{\dim\mathcal{C}}_{\dim\mathcal{C}+1}(\left[\tilde{\boldsymbol{J}}_{c,h}(\vec{\hat{u}}_{f,h}); \Delta\vec{\nu}_{f,h}\right]). \tag{3.13}$$

First an orthogonal basis of the range space $\mathcal{R}$ is computed by orthogonalising $\tilde{\boldsymbol{J}}_{c,h}$ with equation (3.12). Applying this equation once again to $\Delta\vec{\nu}_{f,h}$ renders the component $\vec{\eta}_{f,h}$ of the measurement in $\mathcal{L}$. The scalar error ξ_1 is computed according to equation (3.8). Although this process is critical in terms of accumulating roundoff errors [PTVF92], in actual scenarios the precision of computers is accurate enough, as can be seen in examples. One major advantage of the Gram-Schmidt orthogonalisation is the inherent possibility to compute a Jacobian explicitly with respect to changing parameters $\vec{u}_{f,h}$ in vectors $c < b$ of the vector valued function of equation (3.12) that returns vector $\vec{q}\,^{c}_{b}$ as

$$\begin{aligned}\frac{d\vec{q}\,^{c}_{b}}{d\vec{u}_{f,h}} &= \frac{d\vec{q}\,^{c-1}_{b}}{d\vec{u}_{f,h}} - \vec{q}\,^{c-1}_{c}\left\{\frac{\left(\frac{d\vec{q}\,^{c-1}_{c}}{d\vec{u}_{f,h}}\right)^T\vec{q}\,^{c-1}_{b} + \left(\frac{d\vec{q}\,^{c-1}_{b}}{d\vec{u}_{f,h}}\right)^T\vec{q}\,^{c-1}_{c}}{\left(\vec{q}\,^{c-1}_{c}\right)^T\left(\vec{q}\,^{c-1}_{c}\right)}\right\}^T \\ &\quad + \vec{q}\,^{c-1}_{c}\left\{\frac{2\left(\vec{q}\,^{c-1}_{c}\right)^T\left(\vec{q}\,^{c-1}_{b}\right)\left(\frac{d\vec{q}\,^{c-1}_{c}}{d\vec{u}_{f,h}}\right)^T\vec{q}\,^{c-1}_{c}}{\left(\left(\vec{q}\,^{c-1}_{c}\right)^T\left(\vec{q}\,^{c-1}_{c}\right)\right)^2}\right\}^T \\ &\quad - \frac{(\vec{q}\,^{c-1}_{c})^T(\vec{q}\,^{c-1}_{b})}{(\vec{q}\,^{c-1}_{c})^T(\vec{q}\,^{c-1}_{c})}\left(\frac{d\vec{q}\,^{c-1}_{c}}{d\vec{u}_{f,h}}\right).\end{aligned} \tag{3.14}$$

For a minimisation of ξ_m, the gradient of ξ_m can be computed with equation (3.14) as

$$\frac{d\xi_m}{d\vec{u}_{f,h}} = 2\frac{d\vec{\eta}}{d\vec{u}_{f,h}}\vec{\eta}. \tag{3.15}$$

A standard gradient search [Pap96, PTVF92] can be used to minimise equation (3.10) using $\vec{\eta}$ as defined in equation (3.13) to find best fitting contact parameters $\vec{\hat{u}}_{f,h}$.

3.1.4 Observer Based Correction

In a scenario where it is feasible to probe the object by moving along the surface consecutively in several directions as described above, section 3.1.3 provides a measure of how likely an estimate $\vec{\hat{u}}_{f,h}$ of the contact joint parameters is.

In practical scenarios, however, it is also desirable to track the contact point during manipulation. Then, probing is not feasible and the condition of a nearly constant $\vec{u}_{f,h}$ is violated. Also disturbances in individual probing measurements may require additional filtering. Here, an observer will render better results for $\vec{\hat{u}}_{f,h}$. With each step, this observer incorporates measurements $\Delta\vec{\nu}_{f,h}$ into a previous estimate of both, contact velocity $\vec{\hat{\nu}}_{c,h}$ and contact parameters $\vec{\hat{u}}_{f,h}$. The observer concept proposed here is dual to Kalman-filtering. Figure 3.8 illustrates this information filter. In a first step, the filter minimises a merit function χ. This merit

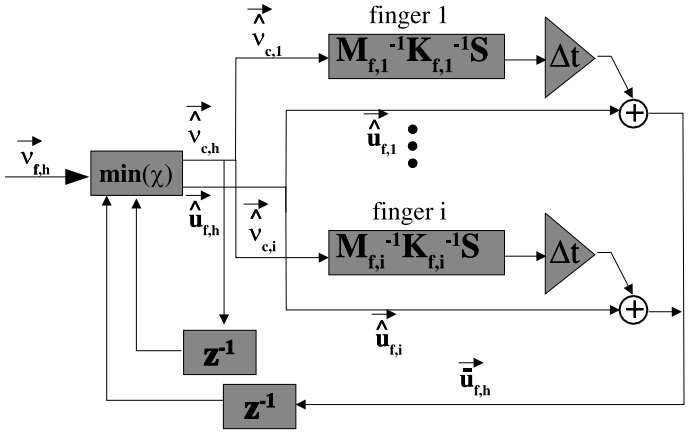

Figure 3.8: Structure of observer: estimation and extrapolation

function consists of two parts. Its first component puts a penalty on the mismatch between the measurement $\Delta\vec{\nu}_{f,h}$ and an expected measurement $\tilde{\boldsymbol{J}}_{c,h}(\vec{\hat{u}}_{f,h})\hat{\vec{\nu}}_{c,h}$ derived from a $\vec{\hat{\nu}}_{c,h}$ and $\vec{\hat{u}}_{f,h}$ as obtained in equation (3.5). The second component punishes a mismatch between an estimate $\vec{\bar{u}}_{f,h}(t)$, previously computed and extrapolated to the actual moment, and the recent estimate $\vec{\hat{u}}_{f,h}(t)$. The recently estimated contact velocity is also compared to its previous value to suppress unlikely large changes but is weighted little, as it is only a state variable in a second

order dynamical, accelerated scenario in contrast to the first order states of contact parameters. The merit function χ is hence defined as

$$\begin{aligned}\chi(\vec{u}_{f,h}, \vec{\nu}_{c,h}, \vec{\hat{v}}_{c,h}(t-1), \vec{\hat{u}}_{f,h}(t)) = \\ \frac{1}{2}\left(\Delta\vec{\nu}_{f,h}(t) - \tilde{\boldsymbol{J}}_{c,h}(\vec{u}_{f,h})\vec{\nu}_{c,h}\right)^T \\ \boldsymbol{C}_m^{-1}\left(\Delta\vec{\nu}_{f,h}(t) - \tilde{\boldsymbol{J}}_{c,h}(\vec{u}_{f,h})\vec{\nu}_{c,h}\right) \\ +\frac{1}{2}\left([\vec{\nu}_{c,h}(t), \vec{u}_{f,h}(t)]^T - \left[\vec{\hat{v}}_{c,h}(t-1), \vec{\hat{u}}_{f,h}(t)\right]^T\right)^T \\ \boldsymbol{C}_s^{-1}(t)\left([\vec{\nu}_{c,h}(t), \vec{u}_{f,h}(t)]^T - \left[\vec{\hat{v}}_{c,h}(t-1), \vec{\hat{u}}_{f,h}(t)\right]^T\right),\end{aligned} \tag{3.16}$$

with $\boldsymbol{C}_m$ and $\boldsymbol{C}_s$ as the measurement and the system covariance matrix respectively. Minimising this merit function χ returns an estimate $\vec{\hat{\nu}}_{c,h}(t)$ for $\vec{\nu}_{c,h}(t)$ and an improvement $\vec{\hat{u}}_{f,h}(t)$ of the previously extrapolated estimate of $\vec{\hat{u}}_{f,h}(t)$ according to

$$\left[\vec{\hat{\nu}}_{c,h}(t), \vec{\hat{u}}_{f,h}(t)\right] = \arg(\min_{\vec{\nu}_{c,h}(t), \vec{u}_{f,h}(t)} \chi(\vec{\nu}_{c,h}(t), \vec{u}_{f,h}(t), \vec{\hat{v}}_{c,h}(t-1), \vec{\hat{u}}_{f,h}(t)))). \tag{3.17}$$

To perform the minimisation, a Levenberg-Marquard algorithm is used. With an estimate of the contact velocity and contact parameters a kinematic extrapolation of $\vec{\hat{u}}_{f,h}(t)$ to $\vec{\hat{u}}_{f,h}(t+1)$ is possible according to equation (3.3) and its inversion in [Mon88]. In this propagation, the complete five-dimensional vector of contact parameters $\vec{u_i}$ for each finger i is needed. The unknown surface properties of the object are approximated as a plane, and so the contact parameters on the object are irrelevant. This is reasonable for common objects with a curvature that is not too high. The extrapolation can be performed for each finger as

$$\begin{aligned}\vec{\hat{u}}_{f,i}(t+1) &= \boldsymbol{M}_{f,i}^{-1}\boldsymbol{K}_{f,i}^{-1}\boldsymbol{S}\vec{\hat{\nu}}_{c,i}\Delta t + \vec{\hat{u}}_{f,i}(t) \\ \boldsymbol{S} &= \begin{bmatrix} 0 & 0 & 0 & 0 & -1 & 0 \\ 0 & 0 & 0 & 1 & 0 & 0 \end{bmatrix} \\ \boldsymbol{C}_s(t+1) &= \frac{d^2\chi}{d\left(\left[\vec{\hat{\nu}}_{c,h}(t), \vec{\hat{u}}_{f,h}(t)\right]^T\right)^2} + \boldsymbol{C}_z.\end{aligned} \tag{3.18}$$

where $\boldsymbol{C}_z$ is the state covariance matrix, $\boldsymbol{S}$ is a selection matrix, $\boldsymbol{M}_{f,i}$ and $\boldsymbol{K}_f, i$ are the metric and curvature matrix of the finger as defined in [Mon88]. According to [PTVF92], the state covariance matrix $\boldsymbol{C}_s$ corresponds to the Hessian matrix of the associated minimisation problem χ.

3.1.5 Numerical Examination of the Merit Functions ξ and χ

In this section, the numerical properties of the merit functions ξ and χ of both approaches, geometric and observer based, are examined. For this, a grasp is simulated in a kinematical model of the DLR Hand II. In contrast to the method presented later in section 3.2, in both approaches presented in this section a number of n fingers has to be in contact with the object. In order to allow re-grasping and hence removal of individual fingers, the algorithms have been tested with the minimum number of fingers required for a stable contact with an object during grasping. From chapter 2.1.5 this number is known to be 3. The item to be manipulated is assumed locally planar in the contact points. In figure 3.9, the fingers

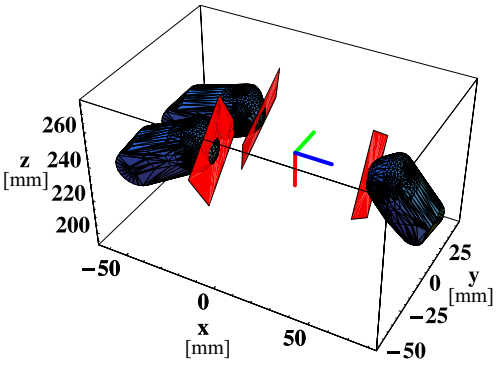

Figure 3.9: Finger tips in contact with an object

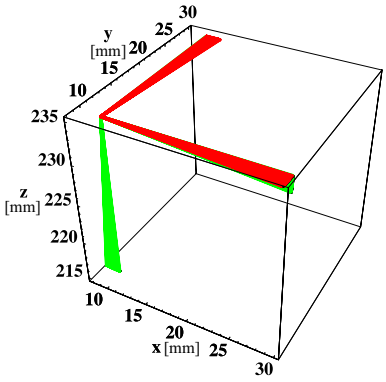

Figure 3.10: Different motions of the object

are represented by their last link and the object is represented by its tangential planes in the points of contact. The finger on the right hand side will be regarded as finger number 1 (thumb), the fingers on the left hand side are numbered from back to front as 2 (index finger) and 3 (middle finger).

The object system $S^{(o)}$ is drawn with its $x-$, $y-$ and $z-$ axis in red, green and blue respectively. It is initially rotated $90°$ around the world's $y-$axis. The finger joints are initially set to $(-7.1°, 17.2°, 21.8°)$, $(1.3°, -5.7°, 45.9°)$ and $(-0.6°, -5.7°, 41.0°)$. The finger tip is modeled as a sphere with radius 11mm which is slightly smaller than the actual fingertip, compensating for deformations in practical experiments. The contact parameters $\vec{u}_{f,i}$ are chosen to be longitude and latitude on this sphere. The zero meridian crosses the finger tip at the palm side, facing into the grasp. The latitude starts at the distal north pole and increases down to the equator. A sketch is given in figure 3.11. The longitudinal

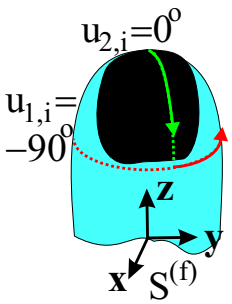

Figure 3.11: Exteroceptive contact parameters

parameters of the three fingers start at $(0.°, 0.°, 0.°)$ and the latitudinal parameters are initialised with $(60.°, 33.°, 30.°)$.

As was pointed out above, observations of motions in several directions have to be combined in order to determine the position of contact. In two sample motions, the object is first rotated around its red x-axis and secondly around its green y-axis, as shown in figure 3.10 in red and green.

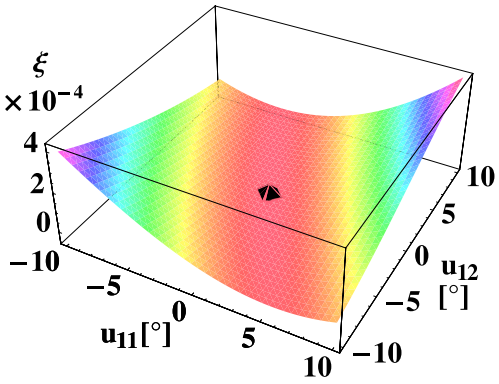

Figure 3.12: Value of ξ over longitudes while rotating around x

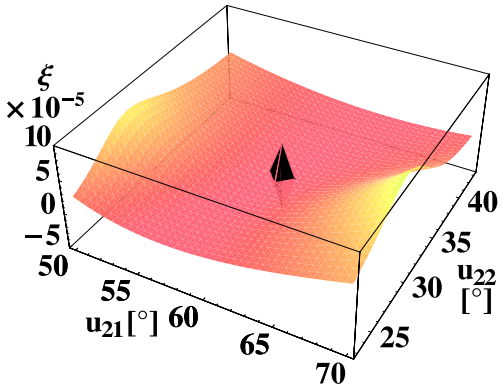

Figure 3.13: Value of ξ over latitudes while rotating around x

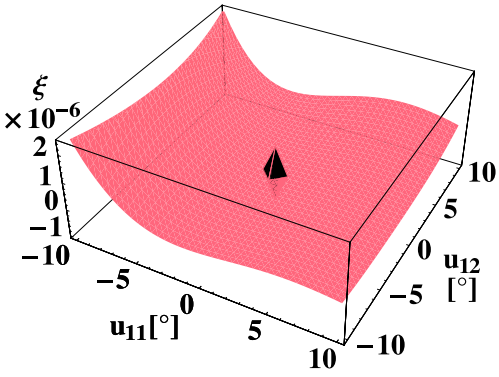

Figure 3.14: Value of ξ over longitudes while rotating around y

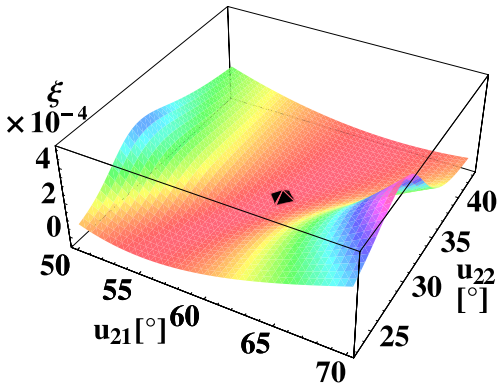

Figure 3.15: Value of ξ over latitudes while rotating around y

The value of the geometric merit function ξ over varying longitudinal and latitudinal contact parameters is shown in figures 3.12 and 3.13 for the rotation around the x-axis and in figures 3.14 and 3.15 for the rotation around the y-axis. The contact parameters are varied $\pm 10°$ around their true value. In the pictures, the true value is marked with a diamond. Neighbouring plots of longitude and latitude use the same colour coding. In both tests, it can be seen that the overall

magnitude of error strongly depends on the direction of motion: when rotating the object around the x-axis, the object rolls more across longitudes than across latitudes of the finger tip's sphere, causing significant errors of ξ when the longitudinal parts of $\vec{u}_{f,h}$ are falsely chosen (see figure 3.12) and only little error when the latitudes are wrong (see figure 3.13). On the other hand, rotating the object about the y-axis moves the object's surface almost only across latitudes of the finger tip, causing significant error on erroneous latitudes (see figure 3.15) and almost no error on erroneous longitudes (see figure 3.14). Due to the usage of a pseudo-inverse in ξ, different from χ below, an intuitive interpretation of this observation is impossible. All four plots exhibit a clear direction of steep gradient and a flat direction. The flat directions correspond to contact positions that are erroneous but somewhat consistent for all fingers, whereas the steep directions are caused by impossible contact positions: for example the object can erroneously be assumed as turned counter-clockwise around its x-axis. Then, the longitudinal contact parameter u_{11} at the thumb would have to be smaller than the true value whereas u_{12} at the index finger would have to be larger than in reality, see diagonal from upper left to lower right in figure 3.12. With this somewhat consistent erroneous assumption, relative velocities $\vec{\nu}_{f,h}$ can be interpreted not correctly, but better causing only little error. In contrast, an inconsistent erroneous assumption would lead to larger errors.

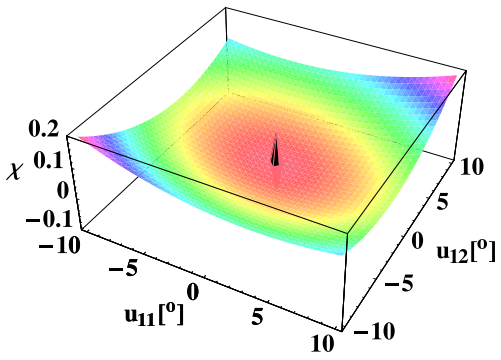

Figure 3.16: Value of χ over longitudes while rotating around x

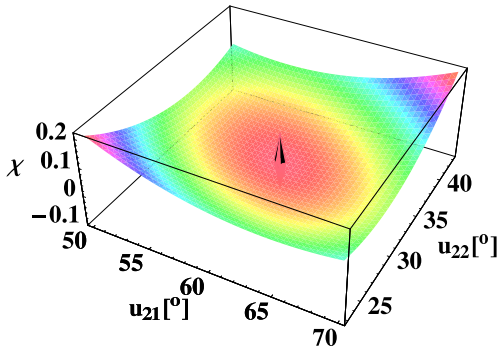

Figure 3.17: Value of χ over latitudes while rotating around x

In figures 3.16, 3.17, 3.18, and 3.19 the observer merit function χ is depicted again over varying longitudinal and latitudinal parameters for $\pm 10°$ while rotating the object around its x- and y-axis respectively. The inverse system covariance matrix $\boldsymbol{C}_s^{-1}$, which propagates information from the past to the actual moment, is set to zero, pretending that any knowledge about the past is completely unreliable. Hence the plots exhibit only the first part of the merit function, which generates new knowledge about the parameters in each estimation step. In all plots, the lack

of steep and flat directions can be noticed. While the geometric merit function ξ inherently estimates the values of the contact velocities $\vec{\nu}_{c,h}$ and thus has only 6 parameters, the observer function χ explicitly contains these variables and consequently is based on 15 parameters. In the latter method, good estimates on other parameters thus have a stronger impact on a single weak estimate causing significant changes in the value of χ. Due to its smaller number of parameters, the first method tolerates single erroneous estimates or a weakly defined combination of estimates to a much larger extent, as can be seen in the flat directions above. In principle, the curvature of χ is high in the direction of a contact parameter u_{ij}, when the rolling motion along the surface travels parallel to the lines of equal value for that parameter and low when traveling orthogonally: For example, the curvature in direction of u_{11} is highest, when rolling around y which makes the object travel almost only along a line of constant u_{11}. In figures 3.16 and 3.17

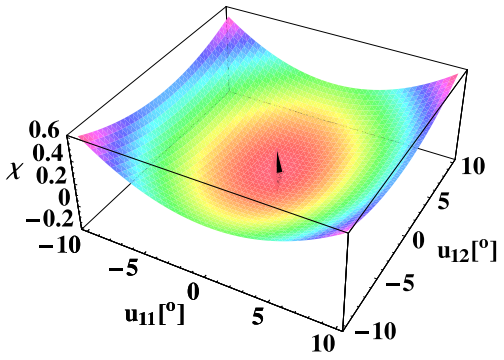

Figure 3.18: Value of χ over longitudes while rotating around y

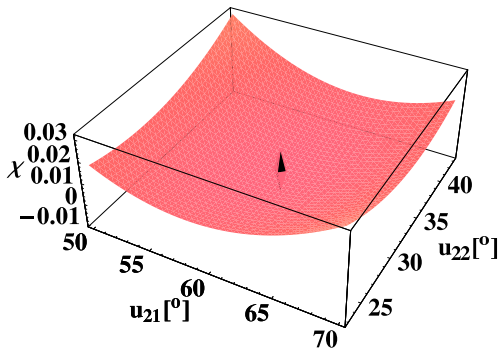

Figure 3.19: Value of χ over latitudes while rotating around y

the error landscape for variations around longitudinal and latitudinal parameters are depicted. The curvature of longitudinal and latitudinal plots are almost even: A Rotation of the object around its x-axis travels across both, lines of longitude and lines of latitude. In contrast, in figures 3.18 and 3.19 the longitudes are better defined than the latitudes. The error increases far more when varying u_{11} and u_{12} than when varying the latitudinal parameters: Rotating the object around its y-axis moves almost only along lines of constant longitude and crosses latitudes orthogonally. Hence, the latter parameter is almost not detectable.

In order to verify the robustness of the given approach to varying measurements, the estimate from the observer based correction is compared to its true value when the object is rotating around its y-axis and some of the measurements are disturbed. In figures 3.20 and 3.21 the distance of the estimated contact point to the true contact point as measured on the surface of a sphere is depicted. The measurements of the finger translational velocities v_{x1} and v_{y1} and rotational ve-

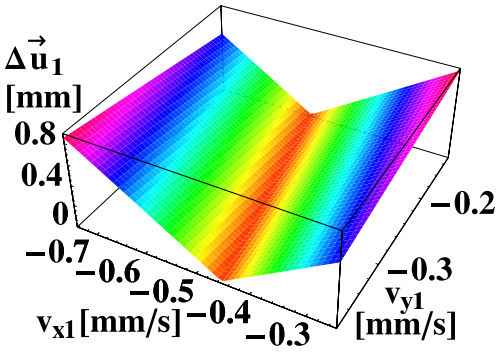

Figure 3.20: Distance between estimate and true value of contact parameters with disturbed measurements in v_{x1} and v_{y1}

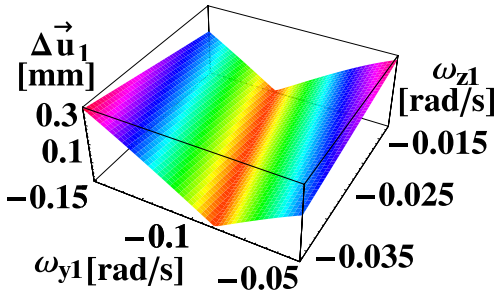

Figure 3.21: Distance between estimate and true value of contact parameters with disturbed measurements in ω_{y1} and ω_{z1}

locities ω_{y1} and ω_{z1} of finger 1 in world coordinates $S^{(w)}$ are varied from 50% to 150% of their true values. Both, the translational velocity v_{y1} and the rotational velocity ω_{z1} have relatively low amplitudes compared to v_{x1} and ω_{y1}: as the body is rotating around its y-axis, finger 1 has to follow this motion by moving down and inwards in world's negative x- and z-direction and rotating clockwise around its y-axis. There is almost no motion along its y-axis nor rotation around the other axes. With the little amplitude, these components of the velocity have low impact on the overall direction of the velocity vector and hence only small influence on the estimation process. This results in the valley-like shape of both pictures. On the other hand, in both cases, the maximum distance on the tip's sphere is less than 1mm although the dominating components of the velocity vector $\vec{\nu}_{f1}$ vary significantly. This proves the robustness of the estimate with respect to measurement disturbance.

3.1.6 Simulation Runs

In this section, the observer based estimation algorithm is examined in its behaviour over time, simulating different object motions. Samples of the location of the object frame at different times are depicted in figure 3.4. The coordinate frames are shaded according to the time as changing hue colour values from red through yellow green, blue, violet to red. The motion sequence is also given in table 3.3. At first, the general properties of tracking this motion are examined, without noise on the measurements. In figures 3.22 and 3.23 the evolution of its contact parameters over time is depicted for all three fingers. Solid lines represent true values while dashed lines represent the respective estimates. Initial true val-

time [s]	motion
0	rotation around y-axis
7.5	rotation around x-axis
15	translation along x-axis
22.5	translation along z-axis
30-60	as above

Table 3.3: Motion of the simulated object

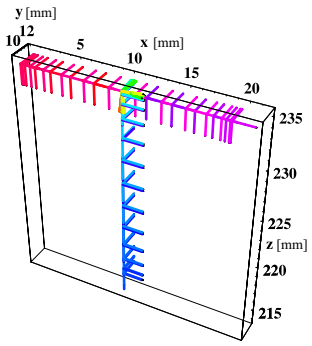

Table 3.4: Motion of the object over time

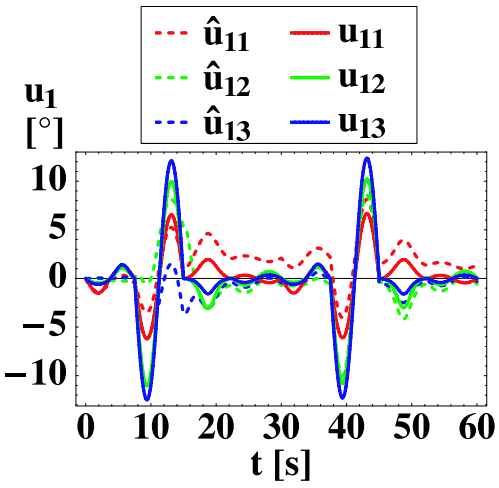

Figure 3.22: Evolution of u_{1i} over time

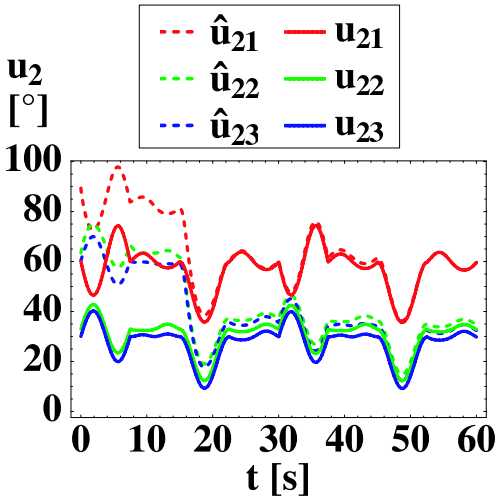

Figure 3.23: Evolution of u_{2i} over time

ues are taken as given in the previous section. The initial estimate is set to a $30°$ mismatch in the latitudes. Estimates of longitudes are set to their real values. As can be seen in figure 3.23, after about 20s the estimates arrive close to their true values. After 60s the latitudinal contact parameters have completely converged. Although the parameters have not converged during the first 20s, their motion nevertheless mimics the motion of the true values. This is a direct result of the dynamic step of the observer, which extrapolates the contact parameters into the future. This figure also shows that certain motions only affect certain directions in the space of contact parameters. While the rotation around the x-axis between $t = 7.5\text{s}$ and $t = 15\text{s}$ hardly causes any convergence in the latitudinal parameters, the translation along the object's $x-$axis between $t = 15\text{s}$ and $t = 22.5\text{s}$ results in

a large decrease of estimation error. In contrast to the theoretical considerations above at plots 3.16 to 3.19, in this setup, several parameters deviate from their true value. Thus, it is impossible to determine by intuition that motion causing the best observability and hence the best decrease of those errors. In the plot of longitudinal parameters in figure 3.22 the estimated parameters deviate slightly from their initial true values. This is in particular true for finger 1. Due to its closeness to the north pole, this deviation causes no large displacement on the surface of the sphere and hence causes only little error in the merit function. Effects of the low-pass properties of the observer can be seen between $t = 7.5\mathrm{s}$ and $t = 15\mathrm{s}$. The estimates are not able to follow the rapid motions in this period. The overall accuracy of the observer can be studied in figure 3.26. In this image, the distance of the true contact point to the estimated contact point on the sphere of the finger tip is depicted. The remaining difference decreases after $20\mathrm{s}$ from initially $6\mathrm{mm}$ to only $2\mathrm{mm}$ and converges to less than $1\mathrm{mm}$ after $60\mathrm{s}$. It does not converge completely to 0 due to a stopping criterion on the minimisation of the merit function χ. Again the effect of different directions of motion can be observed between $t = 15\mathrm{s}$ and $t = 22.5\mathrm{s}$.

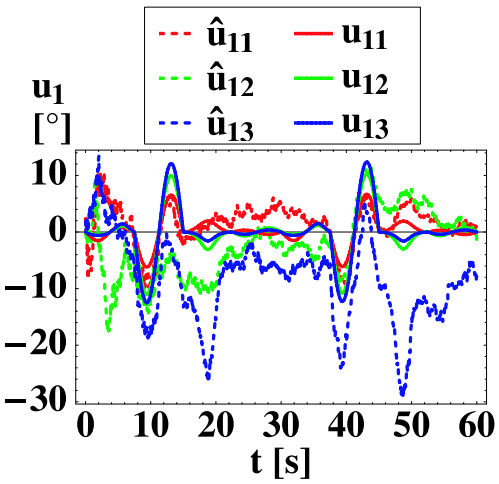

Figure 3.24: Evolution of longitude u_{1i} over time with noise

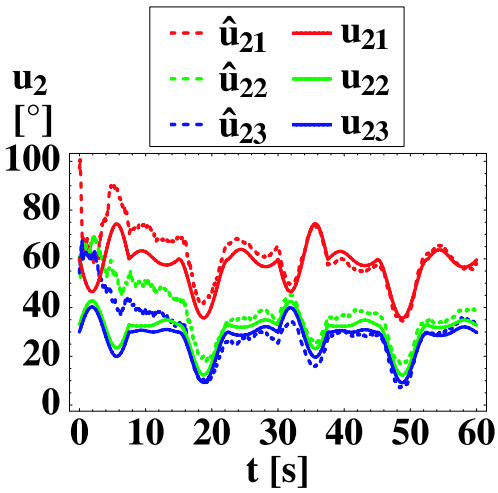

Figure 3.25: Evolution of latitude u_{2i} over time with noise

The same simulation has been run with white Gaussian noise on the measurement of the finger tip velocities. The standard deviation of the noise has been set to $2\mathrm{mm/s}$ for the translational measurements and $1.9°/\mathrm{s}$ for the rotational readings. The values have been chosen according to the noise observed in typical measurements at DLR Hand II. The typical amplitude for a translational finger tip velocities is $6\mathrm{mm/s}$ and $5.7°/\mathrm{s}$ for the rotational velocities. Figures 3.24 and 3.25 show that the general tendencies as discussed above remain the same although

the convergence to the true values is disturbed in some points as can be seen for example in figure 3.25 between $t = 37.5\text{s}$ and $t = 45\text{s}$. As shown above for the corresponding period between $t = 7.5\text{s}$ and $t = 15\text{s}$, the motion of the object in this period is such that latitudinal parameters can only weakly be observed. Consequently this may result in a deviation from a previously better estimate. Nevertheless, the general convergence, as shown in figure 3.27, is still accurate. The remaining error is again below 1mm on the finger tip's sphere. The behaviour is not as steady as in the undisturbed simulation. This, however, is to be expected given the amount of noise inflicted on the measurement.

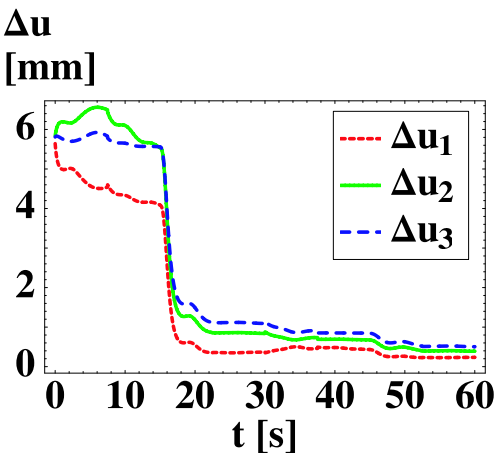

Figure 3.26: Distance between estimate and true value over time

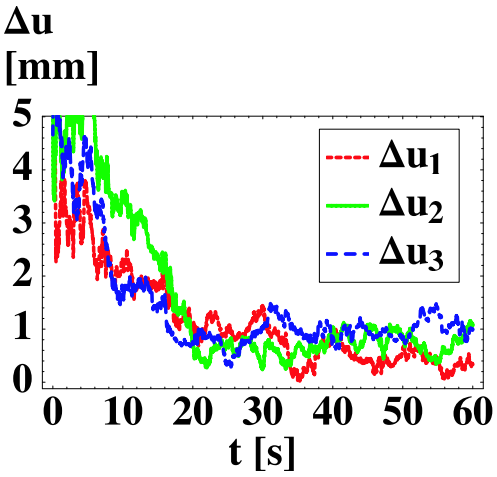

Figure 3.27: Distance between estimate and true value over time with noise

3.2 Contact Positions from Intrinsic Measurements

When a finger touches an object, forces and torques are transmitted at the point of contact. The material characteristics of the finger and object determine the behaviour of transmission as described by different models of contact in section 2.1.4. These forces and torques can be measured at the finger, a measurement which not only depends on the direction and amplitude of the contact forces but also on the point of contact. Hence, from the readings of force and torque sensors, the point of contact can be concluded. The method is termed *intrinsic* contact point detection. Using rigid body mechanics, in this thesis a parameter estimation algorithm is proposed using a least squares approach. This section extends work from literature and allows a uniform approach for all contact models. This

is in contrast to the revisited earlier work (see section 2.1.6). There, Salisbury and Bicchi both present closed form solutions for particular contact models and special surfaces. For more general surfaces, Bicchi presents an iterative method. In some contact models, the total number of unknowns, contact forces/torques together with contact point, is higher than 6, the maximum number of independent force/torque measurements at a rigid body. This leads to a space of indistinguishable contacts. In a line contact for example, a three-dimensional force and a two-dimensional torque is transmitted at the contact point, which can be described with two contact parameters on the surface of the finger. The total number of unknowns is 7 and is thus higher than 6. Salisbury approaches this by multiple measurements. A smooth transition between two contact types, however, is not possible with the methods from literature, but it may be required, for example when only little contact torque is present to switch between soft finger contacts and point contact. Also, additional force /torque measurements e.g. from a joint or wrist sensor, may decrease the influence of measurement noise. These limitations will be relaxed in this section by the generalised approach. Also, in this generalised approach, the subspace of indistinguishable contacts can be directly seen. A comparison of performance of the presented algorithm with work known from literature can be found in [Wim02].

In this section, without loss of generality and for the ease of understanding, derivations are made explicitly for the model of Bicchi's soft finger contact according to [BSB93]. Using this contact model, a transmission of a three-dimensional force $\vec{f_c}$ at the point of contact $\vec{x}_c$ and a one-dimensional torque τ_c around the surface normal is possible. This contact describes a wide variety of contacts actually performed by usual robotic grippers and also includes simpler models as degenerate cases. Further, this section assumes a standard robotic gripper with r serial joints. In each joint s, a sensor measures the resulting torque τ_s. Additionally, a force/torque sensor measures forces $\vec{f_t}$ and torques $\vec{\tau}_t$ induced at the surface of the finger tip. In the remainder of this chapter it is assumed that the contact is made at the finger tip resulting in measurable forces at the finger tip sensor. However, if an adequate sensor is available at another link, this approach also transfers to contacts there. Thus, in this section, the unknown contact location $\vec{x}_c$, contact forces $\vec{f_c}$ and contact torque τ_c are estimated from the finger sensor readings $\vec{\tau}_f = (\tau_1, ...\tau_s, ..)$, and the tip readings $\vec{f_t}$ and $\vec{\tau}_t$.

3.2.1 Measurement Equations for a Merit Function

In order to relate obtained measurements to the unknown parameters, *measurement equations* are defined. Measurements at the finger tip refer to the contact

location and contact force as

$$\begin{aligned} \vec{f}_t^{(t)} &= \boldsymbol{R}_{(t)}^{(fc)} \vec{f}_c^{(fc)} \\ \vec{\tau}_t^{(t)} &= \boldsymbol{R}_{(t)}^{(fc)} [0,0,\tau_c]^T + \vec{x}_c^{(t)} \times \boldsymbol{R}_{(t)}^{(fc)} \vec{f}_c. \end{aligned} \tag{3.19}$$

In this equation, all measurements are displayed in a sensor fixed coordinate system $S^{(t)}$. The homogeneous transform $\boldsymbol{T}_{(t)}^{(fc)}(\vec{x}_c) = \begin{bmatrix} \boldsymbol{R}_{(t)}^{(fc)} & \vec{t}_{(t)}^{(fc)} \\ [0,0,0] & 1 \end{bmatrix}$ relates the contact frame $S^{(fc)}$ to the sensor system $S^{(t)}$. It depends on the actual position of contact $\vec{x}_c^{(t)}$ in sensor coordinates. Revisiting equation (2.5), the contact location

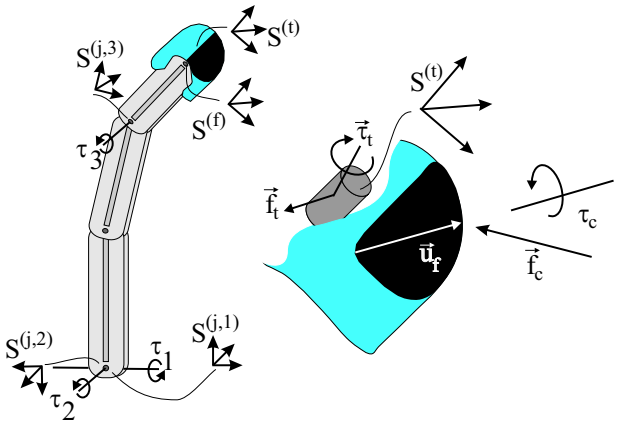

Figure 3.28: Coordinates for intrinsic contact point detection

can be reformulated as

$$\begin{aligned} \vec{x}_c^{(f)} &= \vec{f}_{fc}(\vec{u}_f) \\ \vec{x}_c^{(t)} &= \boldsymbol{T}_{(t)}^{(f)} \vec{f}_{fc}(\vec{u}_f). \end{aligned} \tag{3.20}$$

The homogeneous transform $\boldsymbol{T}_{(t)}^{(f)}$ relates the finger system $S^{(f)}$ to the sensor system. In figure 3.28 a sketch of the coordinate systems is given. This transform is constant and known from calibration and design. Computing joint torques from induced forces and torques requires the lever between the point of induction $\vec{x}_c$ and the point of measurement as

$$\vec{x}_c^{(j,s)} = \boldsymbol{T}_{(j,s)}^{(f)} \vec{x}_c^{(f)}. \tag{3.21}$$

The transform $\boldsymbol{T}_{(j,s)}^{(f)}$ relates the finger system to a system $S^{(j,s)}$ attached to the joint sensor at joint s. This system is defined such that the axis of the joint torque

coincides with the z- axis. The transform can directly be obtained from a kinematic description of the finger and joint position readings $\vec{\theta}$ as introduced in chapter 2.2.2. It contains only measurable quantities. The torque at a sensor can be expressed as

$$\tau_s = [0,0,1]\left(\vec{x}_c^{(s)} \times \boldsymbol{R}_{(j,s)}^{(f)} \boldsymbol{R}_{(f)}^{(fc)} \vec{f}_c^{(fc)} + \boldsymbol{R}_{(j,s)}^{(f)} \boldsymbol{R}_{(f)}^{(fc)} [0,0,\tau_c]\right). \tag{3.22}$$

The transform $\boldsymbol{T}_{(f)}^{(fc)} = \begin{bmatrix} \boldsymbol{R}_{(f)}^{(fc)} & \vec{t}_{(f)}^{(fc)} \\ [0,0,0] & 1 \end{bmatrix}$ relates the contact system $S^{(fc)}$ to the finger system $S^{(f)}$ (see chapter 2.2.2). It depends on the contact point $\vec{x}_c$. Now a vector of measurements can be defined as $\vec{y} = [\vec{\tau}_f, \vec{f}_t, \vec{\tau}_t]^T$. With the equations given above, from estimates of the unknown variables $\vec{x}_c$, $\vec{f}_c$ and τ_c an expected measurement $\vec{\hat{y}}$ can be computed. Using equation (3.20), the three-dimensional vector $\vec{x}_c$ can be substituted by the two-dimensional vector of contact parameters $\vec{u}_f$. Now an approach of least squares is applied. In a merit function ς this measurement vector $\vec{y}$ can be compared to the expected measurements $\vec{\hat{y}}$ according to

$$\varsigma(\vec{u}_f, \vec{f}_c, \tau_c) = \left(\vec{y} - \vec{\hat{y}}\right)^T \boldsymbol{C}_\varsigma^{-1} \left(\vec{y} - \vec{\hat{y}}\right), \tag{3.23}$$

with $\boldsymbol{C}_\varsigma$ as the covariance matrix of the measurement. Minimising ς over the unknown parameters delivers estimates for these parameters as

$$[\vec{\hat{u}}_f, \vec{\hat{f}}_c, \hat{\tau}_c] = \arg(\min_{[\vec{u}_f, \vec{f}_c, \tau_c]} \varsigma(\vec{u}_f, \vec{f}_c, \tau_c)). \tag{3.24}$$

In the case of indistinguishable contacts, the Hessian matrix of $\varsigma(\vec{u}_f, \vec{f}_c, \tau_c)$ will be rank-deficient. Using a Singular Value Decomposition [PTVF92], the respective indistinguishable subspace can be identified.

3.2.2 Numerical Examination of Merit Function ς

This section examines the minimisation properties and robustness of the suggestions of section 3.2.1. The DLR Hand II, as introduced in chapter 2.1.1, is used as sample gripper. A finger of the hand is touching an object in stretched out configuration with all joint angles θ at $(0°, 0°, 0°)$. The finger tip is modeled as a globe with radius $11\mathrm{mm}$ and is parameterised by spherical coordinates $\vec{u}_f = (\phi, \theta)$. The prime meridian $\phi = 0°$ passes through the negative part of the y-axis of $S^{(f)}$ and the north pole. The latitudes θ are measured beginning at the north pole. A drawing of the setup is given in figure 3.29. The contact coordinates are set to $(90°, 45°)$. The contact force is assumed $(-5\mathrm{N}, -5\mathrm{N}, -5\mathrm{N})$ with respect to $S^{(t)} = S^{(f)}$ and the contact torque is set to $0.1\mathrm{Nmm}$. The covariance

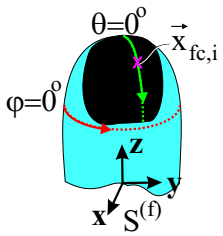

Figure 3.29: Contact parameters for intrinsic contact point detection

Figure 3.30: Colour bar

matrix $\boldsymbol{C}_\varsigma$ has been assumed diagonal, with a standard deviation of 5% of the actual measured value. In figure 3.31 the value of the merit function ς is depicted as contour plot over varying contact parameters $\vec{u}_f$. This plot is also projected onto the sphere of the finger-tip in figure 3.32. The respective values of ς can be obtained from the colour bar in figure 3.30. Within a reasonable neighbour-

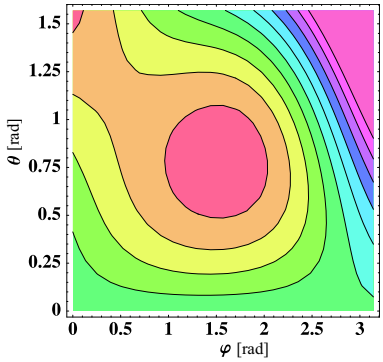

Figure 3.31: Merit function ς over varying contact parameters

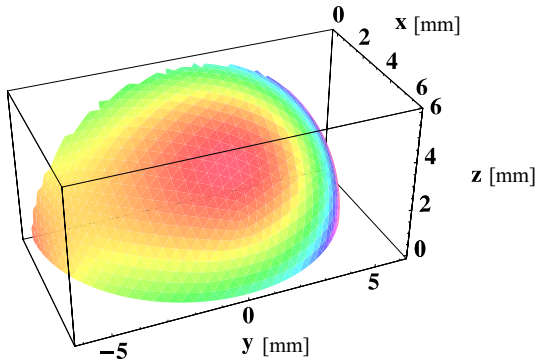

Figure 3.32: Merit function ς projected on fingertip

hood to the point of contact, no other local minimum exists in the plot and the behaviour of ς can be approximated by a quadric. Minimisation is hence done with a Levenberg-Marquard algorithm [PTVF92]. Variations in the reliability of measurements through changes in the entries of the covariance matrix $\boldsymbol{C}_\varsigma$ vary the contribution of individual measurements to the estimate. Examining the different measurements individually unveiled that the error landscape over the contact parameters ϕ and θ, as shown in these figures, is dominated by the measurement of tip torque $\vec{\tau}_t$ from equations (3.19). In comparison, the contribution of other measurements, joint torque $\vec{\tau}_f$ and tip force $\vec{f}_t$, to ς, are much smaller. In figure 3.31, in the upper left corner, the beginning of a second valley can be seen. This is also

visible at the lower left side of the spherical display in figure 3.32. The minima lie at either intersection of the finger surface with the line of action of the contact force. According to the soft-finger contact model, contact forces have to obey Coulomb's law of friction, and also need to be pushing, not pulling. Hence only one of those minima will be located within the valid contact area of the finger at the upper quarter sphere as depicted, and there is a unique solution to the problem of finding the contact location.

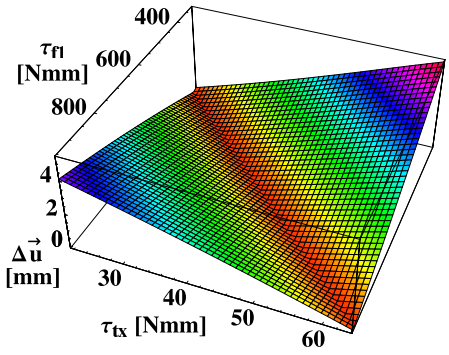

Figure 3.33: Error in estimate of $\vec{u}$ over varying τ_{f1} and τ_{tx}

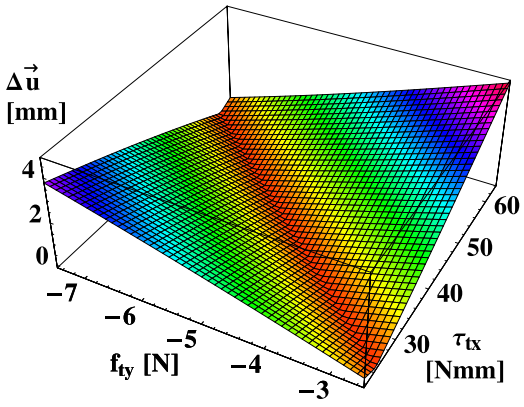

Figure 3.34: Error in estimate of $\vec{u}$ over varying τ_{tx} and f_{ty}

A second evaluation examines the influence of erroneous measurements on the estimated parameters as depicted in figures 3.33, 3.34, 3.35 and 3.36. In all pictures, measurements are varied $\pm 50\%$ around their true values in the centre of the plot. As a measure of accuracy, the distance $\Delta\vec{u}$ of the estimated contact point $\vec{x}_{c,est}$ to the true contact point $\vec{x}_{c,true}$ measured on the surface of the sphere is used in the first three plots. In the fourth plot $\Delta\vec{f}_c$ is depicted as the difference between true and estimated contact force. The uncertainty described by $\boldsymbol{C}_\varsigma$ is set as given above. In figure 3.33, the error in the estimated contact position $\vec{x}_c$ is depicted over the joint torque τ_{f1} and tip torque τ_{tx}. Both torque axes are parallel to each other and lie in the plane described by $\phi = 90°$. The worst case error over the whole displayed area is $5\mathrm{mm}$. Throughout the majority of the parameter range and in a reasonable neighbourhood around the undisturbed measurements it is far below this value. It can also be seen that, when changing tip torque and joint torque uniformly, the algorithm is much more tolerant compared to changing the torques inversely. In the first case, both measurements consistently vote for the same contact point, although they assume a different contact force. When both torques are inversely changed, neither of them is consistent with the measured tip force nor are the torques consistent with each other. Hence a larger error in the contact position occurs. A similar observation can be made in figure 3.34. This

figure depicts the estimation error $\Delta\vec{u}$ over varying tip force f_{ty} and tip torque τ_{tx}. The range of error is comparable to above in this figure. A valley in the diagonal direction is again remarkable. Here, f_{ty} and τ_{tx} produce only little error in the direction from upper left to lower right when they are consistently changed, but cause significant error when they are inconsistently altered from lower left to upper right.

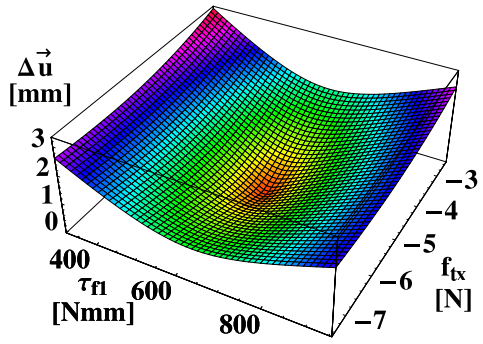

Figure 3.35: Error in estimate of $\vec{u}$ over varying τ_{f1} and f_{tx}

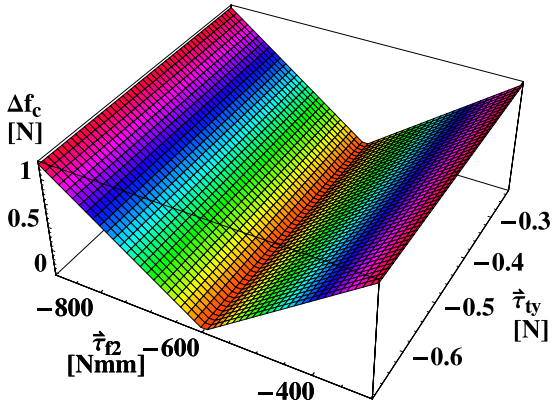

Figure 3.36: Error in estimate of $\vec{f_c}$ over varying τ_{f2} and τ_{ty}

In figure 3.35, $\Delta\vec{u}$ is depicted over changing τ_{f1} and f_{tx}. The two measurements do not influence each other directly in the equations. In this configuration, τ_{f1} can only measure forces in $y-$ direction. These, however, are not measured by f_{tx}. Hence, no direct compensation can take place between both measurements. Here, the nonlinearity of the estimation is dominant. The figure shows that, in this configuration, an error in f_{tx} has a smaller influence on $\Delta\vec{u}$ than τ_{tx}. While the equation for τ_{t1} directly contains the contact point $\Delta\vec{u}$, the equation for f_{tx} is only indirectly influenced by the contact point through estimates of contact forces. In a similar argument, figure 3.36 explains that, when comparing the influence of τ_{f2} and τ_{ty}, the contact force f_c is determined almost entirely by the measurement of joint torque τ_{f2}, and the quality of tip torque τ_{ty} is nearly irrelevant for that parameter estimate. This is due to the very different lever of the two torques.

The ability to correct erroneous measurements is examined in figures 3.37 3.38, 3.39 and 3.40. In these figures, the error of an estimated contact torque and contact force is depicted over varying tip torque and tip force. Plotted in green solid lines is the result of the given approach with only the tip sensor rendering good measurements. Here, no compensation is possible. Depicted in red dashed lines is the result of the given approach and all sensors with good readings. In this case, compensation is possible. It can be seen that an erroneous tip force f_{tx} can be compensated by the joint torque measurements and hence the estimates

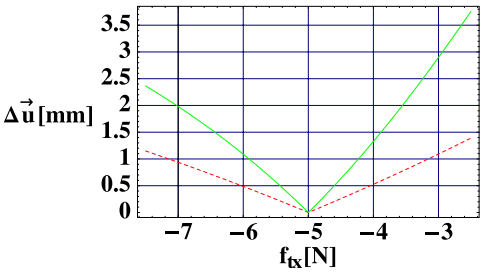

Figure 3.37: Error in estimate of $\vec{u}$ over varying f_{tx} with and without redundant measurements

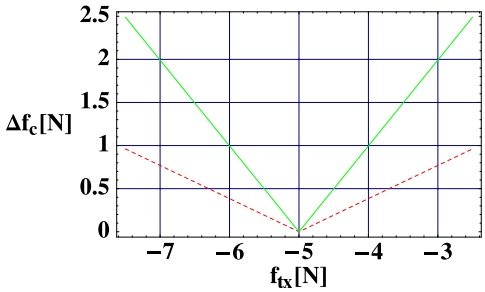

Figure 3.38: Error in estimate of $\vec{f_c}$ over varying f_{tx}

for $\vec{u}$ and $\vec{f_c}$ are more robust in the all-sensor case. An erroneous tip torque τ_{tx},

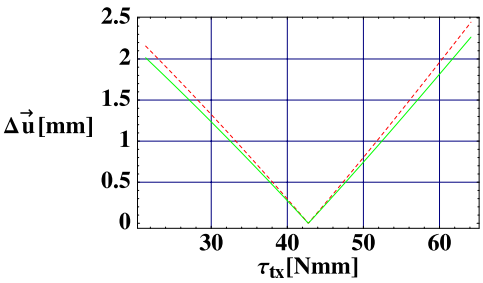

Figure 3.39: Error in estimate of $\vec{u}$ over varying τ_{tx} with and without redundant measurements

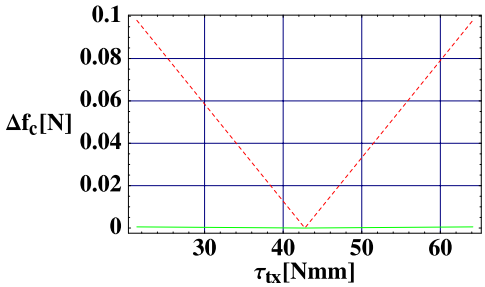

Figure 3.40: Error in estimate of $\vec{f_c}$ over varying τ_{tx}

however, cannot be compensated by joint torque measurements. In both estimated parameters, an attempt to compensate for wrong readings causes a slight deterioration. Compared to the advantage of a far better estimate in the case of a false tip force reading, this slight deterioration, however, is insignificant. Small changes in contact position change the moment arm for tip torques significantly, whereas the lever of joint torques varies only little. Thus, joint torque measurements can hardly compensate erroneous tip torques. On the other hand, the absolute length of the lever at joint torques is much larger than at tip torques. Therefore, tip forces can be compensated very well by joint torque readings. Quantitatively, this behaviour depends strongly on the choice of entries in $\boldsymbol{C}_\varsigma$ and hence on the particular case under investigation. Generally, in order to compute the contact parameters (ϕ, θ) a good tip torque signal is required. In order to compute the force situation at the point of contact, a good tip force signal or equivalently a good joint torque signal is required.

Chapter 4

Detection of Object Position

When a robot hand has to grasp an object, at first every finger individually approaches the item until it makes contact. Now the contact points and the orientation and location of this object should be determined. Due to disturbances or erroneous assumptions, the actual situation may differ from the previous plan of the grasping action. An approach to a mocca maker by the fingers of DLR Hand II

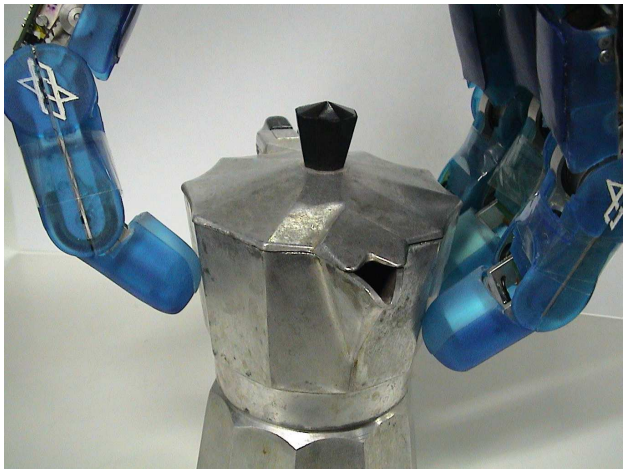

Figure 4.1: Contacting a mocca maker with a dextrous gripper

is depicted in figure 4.1. Measurements taken from each finger are processed, e.g. according to section 3. In this way, the position of the contact point between each finger and the pot in world coordinates can be determined. Also the normal vector of the object and finger surface can be determined. Point and normal describe the tangential plane of contact given in world coordinates. The contact position on the object surface, i.e. the position of the contact point in object coordinates, is, however, still unknown and hence also the position of the pot in world coordinates.

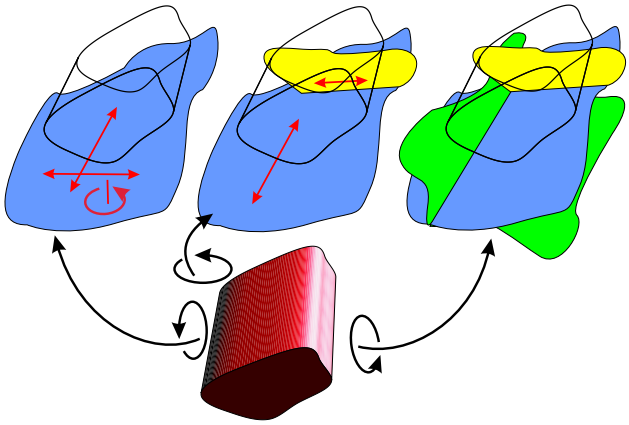

Figure 4.2: Narrowing an object's degrees of freedom by contact planes

As depicted in figure 4.2, each finger contact can give information about the object position by the common tangential plane at the contact point. One tangential plane to an object partially determines the item's position leaving free the two translational and one rotational degree of freedom of the plane. With two regular measurements, the object position is determined except for the single translational degree of freedom along the intersection line of the two tangent planes. With three or more measurements, the object's position is determined completely. This observation is analogous to considerations about force and form closure as presented in chapter 2.1.5. The localisation problem hence translates now to determine an object position and contact positions on the object's surface that fit to the tangential planes, measured through contact. Obviously with measurement noise present either in the contact measurements or in the modeling of the object, the fit has to be determined in the sense of a best match of these parameters. In this chapter, a method will be proposed to compare a previously obtained model of an item with the measurements obtained when several fingers touch the object. Hypotheses for the possible locations of contact can then be generated. Now, for each hypothesis, an object position has to be estimated that best matches the respective parts of the object surface to the measured point of contact. The degree of match determines the quality of the hypothesis. On the sample pot, the hypotheses of contact location for example can be described as answer to the question "Which face of the ten sided pot is touched by which finger?". With these faces, the object position can be determined to fit to the measured tangential planes.

Modeling of the object for this particular purpose and consistent preparation of the measurements is described in section 4.1. For the examination, in section 4.2 an algorithm is introduced which allows separation of computational load into

two parts: In a modeling phase, object data is prepared and stored in a library for rapid access (see sec. 4.2.2). This can be done off-line before a task execution. In a detection phase, previously stored data is tested (see sec. 4.2.2) and contact hypotheses are generated and verified (4.2.3). This part has to be performed online on the basis of actual measurements.

Using the classification of algorithms as introduced in section 2.1.7, this method represents the *locating* process in the two steps of the algorithms termed *recognising before locating*. The methodology used here is in generally valid for any position detection, once contact is made. By limiting input information to contact measurements, however, the density of information is sparse compared to e.g. optical localisation methods: While contact information is usually only available at few points, optical scene images can contain far more points of an object, allowing to use also for example edges and vertices for position detection. Thus the intention of the algorithm presented here is to enhance the capabilities of other visual localisation systems by giving information "while doing". The proposed algorithm uses the same measurements that are also used for control of the fingers of a hand. For this reason, during a grasp, contact information is always available and so no obstruction can occur. Also, calibration of the localisation system and the control system with respect to each other is inherent.

Other researchers also examined the evaluation of contact information and tactile data for the location of an object (see 2.1.7). The approach presented here, however, can locate the object statically from only one grasp, and thus stands out from those model-free approaches that require some way of object exploration. Unlike other approaches that also use an object model, this approach generalises the concept of generation of hypotheses for contact locations at the object prior to object localisation. In this generalised concept it is possible to control the generation of hypotheses not only by information that pairs of contacting fingers generate, but also by information from general contact tuples. Additionally, for the generation of hypotheses, an optimised concept is proposed that improves the performance of a method called *branch and bound* [Bur72, Ben03, GHP$^+$97]. In classical branch and bound, a tree of all possible hypotheses is developed, with the degree of refinement increasing to the end of the branches. Systematically, the hypotheses at the junctions of the tree are tested. When the hypotheses test fails, the whole branch with all more refined hypotheses is pruned. Here, instead of testing and pruning a complete tree, only the feasible subtrees are generated at each level of refinement. By its two-step concept of generating hypotheses and locating the object, this algorithm can also naturally handle the generation hypotheses more generously when measurements are afflicted with noise. The localisation step then performs estimation of object position in a least squares method to discover the hypothesis that best matches the disturbed measurements.

4.1 Describing Object and Measurements

4.1.1 An Object Model For Contact Sensing

For the method to be presented in this chapter, tactile perception from n fingers of a robotic hand has to be compared with a model of the grasped object. As discussed in chapters 2.1.2 and 3, measurements obtainable from robotic fingers usually consist of isolated points of contact with surface normal and possibly isolated forces and torques at the point of contact. Only by sophisticated sensors or exploration methods can more information, e.g. about the curvature at the contact be received. Hence, extending the nomenclature of [JH98] to non-optical sensors, the measurement of a real robotic hand is usually limited to an *oriented point*, a position and orientation of surface normal. Comparing the object descriptions given in chapter 2.2.3, modeling through polygonal surfaces best represents the features detected by measurements of oriented points. Additionally, for simple objects this modeling is also suitable to manually setup and easy to interpret by inspection without graphical rendering. This format is wide spread in graphical tool software and hence particularly advantageous as issues of modeling and model post-processing is not in the focus of this work. Although neither modeling nor the algorithm presented here rely on a particular number of vertices of a polygon in this polygonal description, for the sake of clearness in presentation, triangles are used as polygons. Subsequently, an object will be represented by m triangular facets. The accuracy of the object description depends on the number of facets used to sample the surface and is hence adjustable to the actual precision needs. The individual facets $k \in [1, m]$ are characterised by its vertices $\left(\vec{x}^{(o)}_{1,k}, \vec{x}^{(o)}_{2,k}, \vec{x}^{(o)}_{3,k}\right)$. The coordinates are given in an object-fixed coordinate frame $S^{(o)}$. In order to compare a surface given in facet representation to perceptions from the hand obtained as oriented point, a description of the plane containing the facet is constructed. The parameters of the plane, given in offset/direction notation, can be interpreted as corresponding oriented point $\vec{p}_{oc,k} = (\vec{x}^{(o)}_{oc,k}, \vec{n}^{(o)}_{oc,k})$ for facet k. Additionally, the region of validity for this planar description is given by the boundaries of the triangular face. The planar description is computed as:

$$\begin{aligned} \vec{x}^{(o)}_{oc,k} &= \frac{1}{3}\left(\vec{x}^{(o)}_{1,k} + \vec{x}^{(o)}_{2,k} + \vec{x}^{(o)}_{3,k}\right) \\ \vec{n}^{(o)}_{oc,k} &= \left(\vec{x}^{(o)}_{2,k} - \vec{x}^{(o)}_{1,k}\right) \times \left(\vec{x}^{(o)}_{3,k} - \vec{x}^{(o)}_{1,k}\right) \\ d^{(o)}_{oc,k} &= -\left(\vec{n}^{(o)}_{oc,k}\right)^T \vec{x}^{(o)}_{oc,k}. \end{aligned} \tag{4.1}$$

As depicted in figure 4.3, the point $\vec{x}^{(o)}_{oc,k}$ represents the centre of gravity of the vertices of the facet k and the surface normal $\vec{n}^{(o)}_{oc,k}$ is represented by the third axis

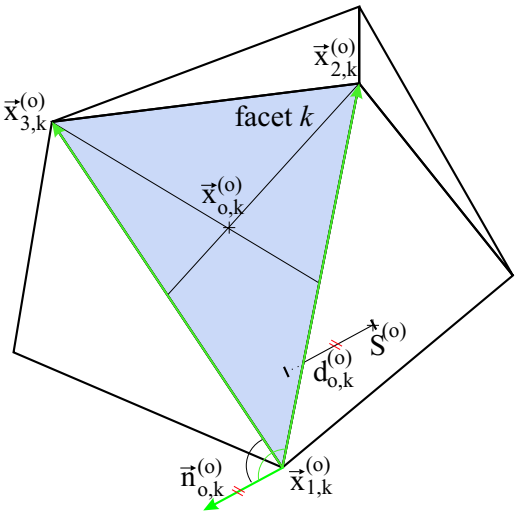

Figure 4.3: Description of facet k

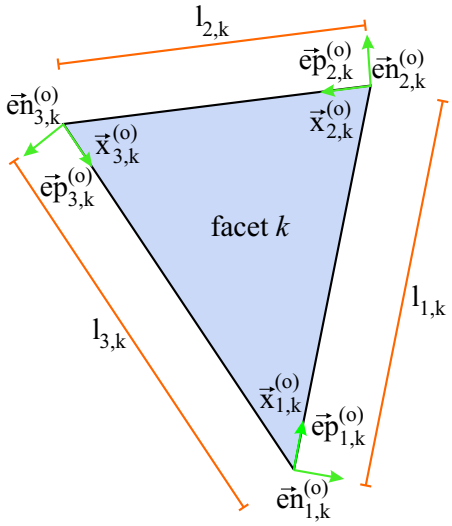

Figure 4.4: Vertex coordinates at facet k

of the non-orthogonal frame constructed by the first and third edge of the facet. Depending on the method used to generate the triangulated model, the normal can sometimes also be obtained directly from the object description as an additional parameter to a facet or to a vertex. The latter requires averaging of normals as discussed in chapter 2.2.3. The distance of the triangle plane to the origin $S^{(o)}$ along $\vec{n}^{(o)}_{oc,k}$ is represented by $d^{(o)}_{oc,k}$. The plane can be described in normal form as

$$\left(\vec{n}^{(o)}_{oc,k}\right)^T \vec{x}^{(o)} + d^{(o)}_{oc,k} = 0 \tag{4.2}$$

with $\vec{x}^{(o)} \in$ triangle k. When n fingers grasp an object, n oriented points $\vec{p}_{oc,k}$ can be combined to a set $\mathcal{F}_{oc}$ of possible contact locations.

In order to describe the boundaries of the triangle and the distance of any point $\vec{x}^{(o)}$ to the facet within the triangle plane k, a two dimensional coordinate system $S^{(v)}_{r,k}$ is defined at each vertex r as shown in figure 4.4. Its two basis vectors are one parallel $e\vec{p}^{(o)}_{r,k}$ and one normal $e\vec{n}^{(o)}_{r,k}$ to the adjacent edge between $\vec{x}^{(o)}_{r,k}$ and $\vec{x}^{(o)}_{((r+1) \bmod 3),k}$ of length $l_{r,k}$ as

$$\begin{aligned} l_{r,k} &= \| \vec{x}^{(o)}_{((r+1) \bmod 3),k} - \vec{x}^{(o)}_{r,k} \| \\ e\vec{p}^{(o)}_{r,k} &= \frac{\vec{x}^{(o)}_{((r+1) \bmod 3),k} - \vec{x}^{(o)}_{r,k}}{l_{r,k}} \\ e\vec{n}^{(o)}_{r,k} &= e\vec{p}^{(o)}_{r,k} \times \vec{n}^{(o)}_{oc,k}. \end{aligned} \tag{4.3}$$

With this, the interior of the triangle can be described as

$$\begin{aligned} & \vec{x}^{(o)} \in \text{triangle } k \Leftrightarrow \\ \forall_r \quad & \left(e\vec{n}_{r,k}^{(o)}\right)^T \left(\vec{x}^{(o)} - \vec{x}_{r,k}^{(o)}\right) \leq 0. \end{aligned} \tag{4.4}$$

4.1.2 Evaluation of Measured Contact Information

With a finger i touching an object in the course of grasping, detection of the oriented point of contact $\vec{p}_{fc,i} = (\vec{x}_{fc,i}^{(w)}, \vec{n}_{fc,i}^{(w)})$ in the world reference frame $S^{(w)}$ is possible (see chapter 3). The measurements $\vec{p}_{fc,i}, i \in [1, n]$ from n fingers can

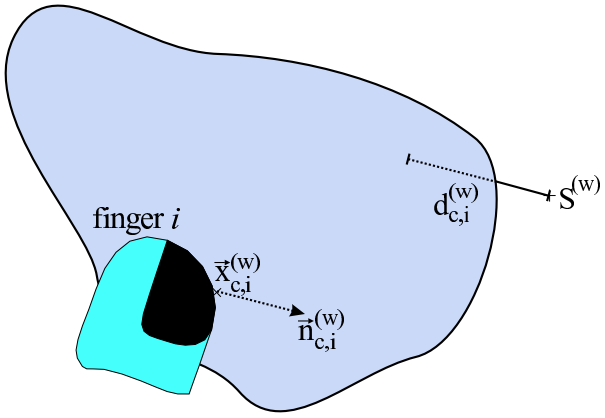

Figure 4.5: Description of contact i

be combined to a set $\mathcal{F}_{fc}$ of perceptions in a grasp. This set can be used to describe the planes tangential to the object in the points of contact in normal form analogously to equation (4.2) as

$$\begin{aligned} 0 &= \left(\vec{n}_{fc,i}^{(w)}\right)^T \vec{x}^{(w)} + d_{fc,i}^{(w)} \\ \text{with} & \\ d_{fc,i}^{(w)} &= -\left(\vec{n}_{fc,i}^{(w)}\right)^T \vec{x}_{fc,i}^{(w)}, \end{aligned} \tag{4.5}$$

with $d_{fc,i}^{(w)}$ representing the distance of the tangential plane to the origin $S^{(w)}$ along $\vec{n}_{fc,i}^{(w)}$ as illustrated in figure 4.5. These measured planes correspond to properly chosen planes $k \in [1, m]$ of the object description as given in section 4.1.1. The process of choosing a correspondence and hence putting up a hypothesis (i, k) for the position of contact between object and finger i is treated in the next section.

4.2 Matching Model and Contact Measurements

Assume a sufficient number n of fingers is in contact with an object. Then, the object can be rotated and shifted in space in order to find n contact positions of the fingers on the surface of the item, which bring the respective surface description in compliance with the measurement as shown in figure 4.6. On a continuous object model this could be achieved by minimisation of an error defined from the discrepancy between the related oriented points or planes. In this continuous case, the optimisation parameters are two independent surface coordinates for each contact on the object and the location and orientation of the item itself. As

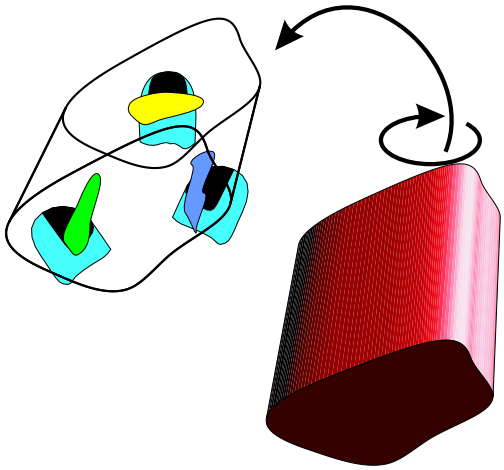

Figure 4.6: Determination of object position

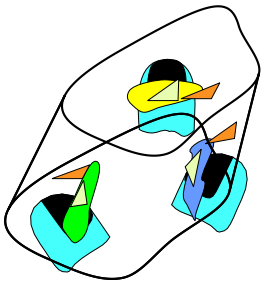

Figure 4.7: Determination of finger contact points

discussed in section 4.1.1, the best object model for this comparison, however, is non-continuous. At this discontinuous type of model, the optimisation has to be separated into a discrete search of contact positions, in this case contact triangles as depicted in figure 4.7, and into a continuous optimisation to detect location and orientation of the object.

4.2.1 Geometric Conditions as Constraints to a Search

With a model consisting of m facets and a hand grasping an item with n fingers there are m^n possible sets $\mathcal{F}_{oc}$. Hence, the complexity of a complete search on all possible $\mathcal{F}_{oc}$ would be in the order $O(m^n)$. This is polynomial in the number of facets but exponential in the number of fingers. Therefore, with an increasing number m of facets the complexity increases with the power n of number of fingers. A practical model of a real world object with a general shape can easily

contain 10 000 facets. If one complete test for compliance of selected facets $\mathcal{F}_{oc}$ and measurement $\mathcal{F}_{fc}$ would only take $1\mu s$ a complete search would still need $10^{10}s \approx 317y$. With this large number of facets a complete search would be prohibitive. It is not necessary, however. Given measurements impose geometrical constraints, *grasp conditions*, on the admissible facets of the object model. These grasp conditions can be the distance between two contact points, the angle between the surface normal, the volume of the tetrahedron formed by two points with adjacent normal vectors and a third point or others. With these grasp conditions, it is possible to search and remove facets already on lower levels of permutation, e.g. facet pairs, before forming full n-tuples instead of working on n-tuples of a full search from the beginning. A sketch of this process is given in figure 4.8. When examining a-tuples with b facets still remaining after previous constraints and n fingers grasping an object, $\binom{n}{a}$ sets of size b^a have to be examined. The advantage of this process is that it is possible to prune several small sets instead of searching one large set. The effort of searching small sets increases only linearly with the number of sets to prune. When also considering

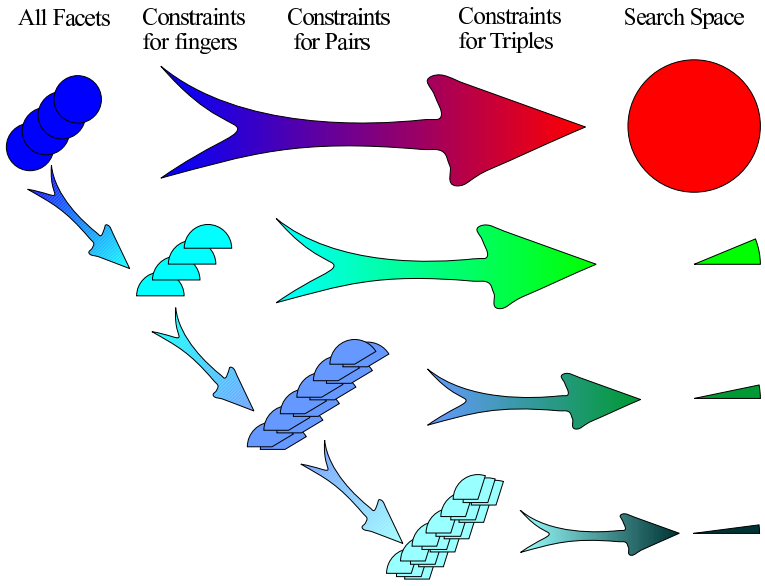

Figure 4.8: Reducing combinatorial effort

the construction of the search space from several small sets, this process can also be considered as an extension to the known process of *branch and bound* as introduced above. In the branch and bound process, those more refined branches of a tree are pruned whose less detailed junction was tested infeasible. In this proposition, only a reduced tree is developed, which does not contain those branches to be pruned. The grasp conditions can be chosen to be geometric invariants of rigid

body transformations, e.g. distances between two points or the angle between surface normals. An enhanced object model can be designed which sorts and indexes the facet tuples according to these grasp conditions. This sorting and indexing can then be performed off-line. In order to extend the object model in this manner, the grasp conditions must first be easily and quickly verifiable from measurements during the online phase, and second be reasonably fast to compute off-line for all facets in the original model. The latter is important, in particular for large models that need a huge amount of grasp condition testing during classification of facets tuples. Second, when processing the object model off-line, no absolute positions with respect to a later grasp are yet known. Hence, only relative information between facets can be used. As already depicted in figure 4.8, the expense of storing and testing increases with higher levels a of permutations as seen above. The profit, however, decreases. Hence, restraining grasp conditions to $a = 1$ of admissible facets and $a = 2$ of facet pairs is usually a good trade-off between cost and use and is mainly followed in the rest of this chapter. Nevertheless constraints of $a > 2$ can be constructed, e.g. to distinguish between triples of points forming the same triangle, but allowing different orientations within this triangle relative to one surface normal as shown in figure 4.9. These constraints can become useful

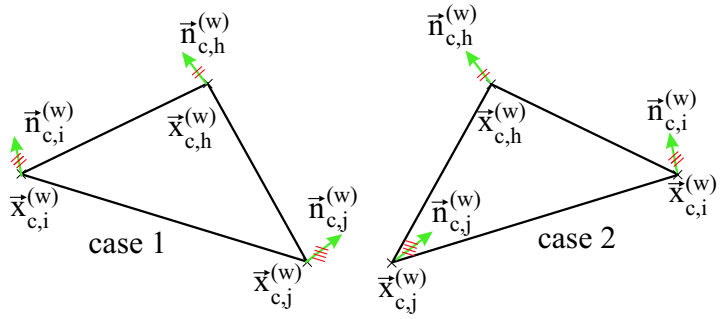

Figure 4.9: Indistinguishable configurations for pair-conditions

for very large objects and remain feasible by using different triangulation rates m_a on different levels of a. As mentioned, for standard purposes grasp conditions for pairs are sufficient. Simple conditions obtainable from the measured set $\mathcal{F}_{fc}$ are the relative distance $\Delta_{fc,ij}$ between the contact points of two fingers i and j and the angle $\alpha_{fc,ij}$ between the respective surface normals. These conditions are defined by

$$\begin{aligned} \Delta_{fc,ij} &= \| \vec{x}^{(w)}_{fc,j} - \vec{x}^{(w)}_{fc,i} \| \\ \alpha_{fc,ij} &= \arccos(\vec{n}^{(w)}_{fc,i} \cdot \vec{n}^{(w)}_{fc,j}). \end{aligned} \tag{4.6}$$

Figure 4.10 illustrates these conditions. Another simple condition is the ordering Ω_{fc} of the sorted individual oriented points. It can be determined according to

$$\Omega_{fc} = \det(\left[\vec{x}_{fc,2}^{(w)} - \vec{x}_{fc,1}^{(w)}, \vec{x}_{fc,3}^{(w)} - \vec{x}_{fc,1}^{(w)}, \vec{x}_{fc,4}^{(w)} - \vec{x}_{fc,1}^{(w)}\right]). \tag{4.7}$$

This condition is depicted in figure 4.11. It easily tests 4-tuples. Off-line classification using this condition in standard object resolution is infeasible. However, it is very cheap to test and can hence be used as pretest during online facet matching before performing the regular position detection.

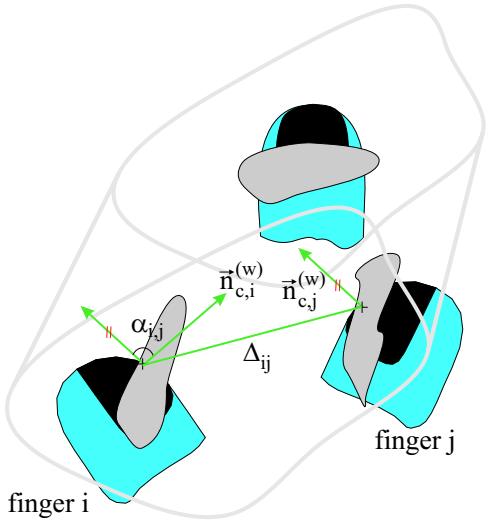

Figure 4.10: Grasp conditions on pairs

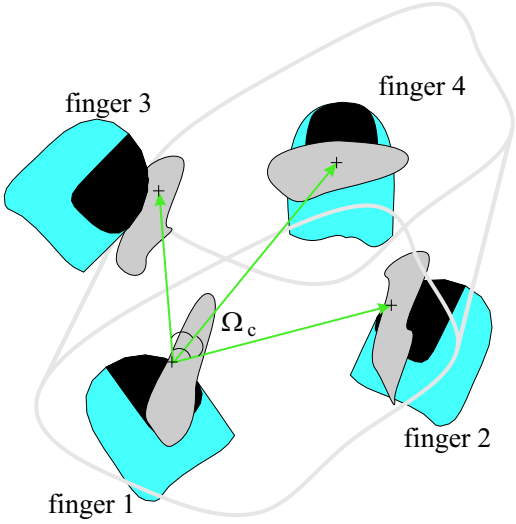

Figure 4.11: Grasp condition on 4-tuples

The off-line process of enhancing the model is briefly described in the first part of section 4.2.2. The retrieval of admissible facets from the enhanced object description and development of grasp hypotheses during actual grasping is explained in the second part. It is only this step that is to be performed in real time. This separation into a preparation step and an execution step is comparable to a human studying an object when first being confronted with it, and on a later re-encounter using this information to grasp it in different positions.

4.2.2 Discrete Optimisation

Learning Phase

This section presents a method to refine a triangulated geometry with data required to evaluate the grasp conditions and to fit measurements from a hand to

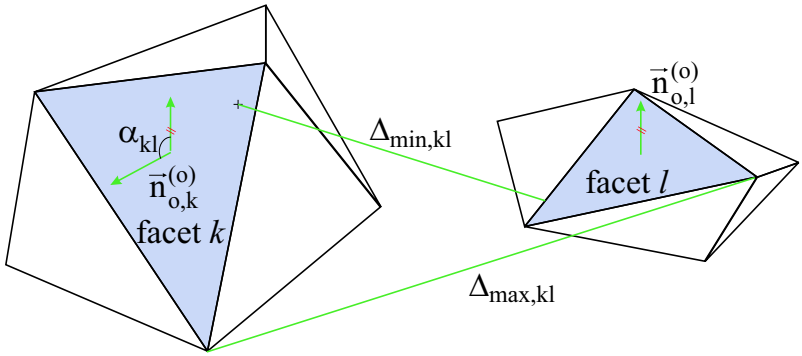

Figure 4.12: Characteristics of a facet pairing

the object. This accelerates the choice of admissible facet hypotheses $\mathcal{F}_{oc}$ during the actual online phase. The trade-off with this method is an increased consumption of memory, because all information learned about the object has to be stored for later use. In the following, the maximum memory usage in each step is also presented, assuming that one numerical value consumes memory of size ε. On common computer architectures ε is 4 bytes.

Learning Individual Facets In the course of learning about an object its individual facets are stored in a list F_1. Index 1 indicates that each entry in the list contains only information about one facet. This list contains, for each facet, its geometrical data: coordinates of vertices $\vec{x}^{(o)}_{1,k}, \vec{x}^{(o)}_{2,k}, \vec{x}^{(o)}_{3,k}$ and direction of surface normal $\vec{n}_{oc}$. Additionally in the optimisation step derived data is required as given in equations (4.1) and (4.3). This data is already computed ahead. The memory consumption sums to $\mathrm{size}(\mathrm{F}_1) = m{\cdot}(3{\cdot}3{+}3{+}3{+}1{+}3{\cdot}1{+}3{\cdot}3{+}3{\cdot}3){\cdot}\varepsilon = m{\cdot}37{\cdot}\varepsilon$.

Preparation of a List of Facet Pairs In a next step, individual facets are grouped in pairs in preparation for the verification of the grasp conditions. The relative geometrical properties of the m^2 possible facet pairs are determined and stored in a list P_2. Index 2 emphasises that this list contains information about facet pairs. It is to be noted, that two fingers may contact on the same facet and also the ordering of fingers and respective facets is of importance. Thus, this list in principle has dimension m^2, although for the sake of saving memory the information of one pairing k and l has to be stored only once and the multiplicity has to be taken into account when reading from the list. In contrast to the relative distance and orientation of two isolated oriented points i and j from a tactile perception, the distance of points on two facets k and l spans a range between a maximum and a minimum Euclidean distance $\Delta_{min,oc,kl}$ and $\Delta_{max,oc,kl}$. On the other hand the relative angle $\alpha_{oc,kl}$ between two facets is constant over the whole area. The relative maximum

distance $\Delta_{max,oc,kl}$ between two triangles must be spanned between two vertices of these triangles. Hence it is sufficient to determine and compare the $3^2 = 9$ possible distances between the vertices.

Proof: Assume, the maximum distance d exists between two points $\vec{x}_1$ and $\vec{x}_2$ in the interior of the respective triangles 1 and 2. All points with same distance d away from $\vec{x}_1$ lie on a sphere of radius d around $\vec{x}_1$. For d to be the maximum distance, all points of triangle 2 must lie within or on the surface of this sphere. With the triangles being planar, if $\vec{x}_2$ is in the interior of the triangle, the triangle intersects or touches the sphere at $\vec{x}_2$ and there exists at least one point $\vec{x}_2' \in$ triangle 2 which is outside the sphere, and hence a larger sphere could be constructed with $d' = \mid \vec{x}_2' - \vec{x}_1 \mid$. The same argument holds for points on the edges of the triangles. Hence, the maximum distance must lie between two vertices. □

For the minimum distance $\Delta_{min,oc,kl}$ a constrained minimisation is necessary as in this case no assumption on the position of $\vec{x}_1$ and $\vec{x}_2$ can be made. However, there exist numerous algorithms that provide for minimum distance between triangles that are applicable for this case, e.g. in obstacle avoidance. The memory consumption of P_2 amounts to $\mathrm{size(P_2)} = 1/2 \cdot m \cdot (m+1) \cdot 3 \cdot \varepsilon$ when it is saved in a compacted form. This storage is temporary and can be cleared after the next step. It is to be noted that in this work only grasp conditions for pairs are further investigated. However, in the same manner a list P_a of triples, $a = 3$, or a-tuples can also be constructed.

Preparation of a Hash Table of Facet Pairs In order to speed up selection of facet tuples complying with the grasp constraints from P_2, another step is suggested. When regarding P_2 as a map from the domain of facet pairs to the associated domain of grasp constraints, in this case maximum and minimum distance and angle between the facets, an inverse map H_2 can be defined. The map H_2 relates the domain of grasp conditions to the domain of facet pairs obeying these constraints. For those conditions presented here, H_2 can be represented as a 3-dimensional container of lists of facet pairs. Each axis of the container corresponds to one $\diamond$ with $\diamond \in \{\Delta_{min,oc}, \Delta_{max,oc}, \alpha_{oc}\}$. Its range is discretised into $p_\diamond$ equally spread bins of width $q_\diamond$, see figure 4.13. On each axis, the bin size depends on the overall maximum $Max_\diamond$ and minimum $Min_\diamond$ of each $\diamond$ within all possible facet pairs and is defined corresponding to

$$\begin{aligned} Max_\diamond &= \max_{kl} \diamond_{kl} \\ Min_\diamond &= \min_{kl} \diamond_{kl} \\ q_\diamond &= \frac{Max_\diamond - Min_\diamond}{p_\diamond}. \end{aligned} \tag{4.8}$$

The access functions to each of the three bin coordinates (t_1, t_2, t_3) are defined by

$$\begin{aligned} t_1(\Delta_{max,kl}) &= \text{floor}(\frac{\Delta_{max,kl} - Min_{\Delta max}}{q_{\Delta max}}) \\ t_2(\Delta_{min,kl}) &= \text{floor}(\frac{\Delta_{min,kl} - Min_{\Delta min}}{q_{\Delta min}}) \\ t_3(\alpha_{kl}) &= \text{floor}(\frac{\alpha_{kl} - Min_{\alpha}}{q_{\alpha}}) \\ \text{with} \quad & t_1, t_2, t_3 \in I\!N. \end{aligned} \tag{4.9}$$

Figure 4.13 depicts the access of H_2 through (t_1, t_2, t_3). Again, the implemen-

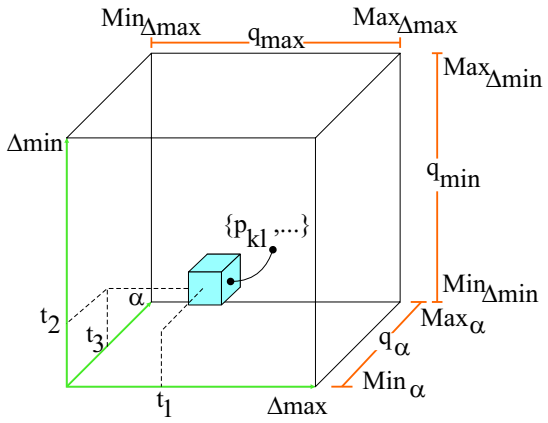

Figure 4.13: 3D container H_2 for sorted pairs

tation has been presented with three grasp conditions for pairs. This can, however, easily be extended to a a dimensional container H_b of b-tuples for a constraints. Usually, H_2 will be sparsely occupied. Along with its property of having bins instead of continuous values, a good implementation for this storage is a hash table. When F_1 is also kept, the hash table has to contain only the indices of the tuples. Hence, the memory consumption for H_2 amounts to $\text{size}(\text{H}_2) = 1/2 \cdot m \cdot (m+1) \cdot 2 \cdot \varepsilon$ plus additional space $3 \cdot 3 \cdot \varepsilon = 9 \cdot \varepsilon$ for the addressing information.

Detection Phase

In this section, the selection of possible contact points of n fingers at the object is presented. These are limited to those points that lie in sets $\mathcal{F}_{oc}$ of facets that comply with the grasp conditions. In order to construct $\mathcal{F}_{oc}$, the measured perception of a set $\mathcal{F}_{fc}$ can be used to extract facet pairs for two fingers i and j respectively

from the hash table H_2. These pairs have to satisfy the first two relative grasp conditions. Respecting also the third grasp condition, the orientation of ordered points, these lists can be merged to admissible n-tuples of facets forming hypotheses $\mathcal{F}_{oc}$ for facets that contain the contact points on the object corresponding to the oriented points from the measurement.

Selecting Admissible Facets From the measurement set $\mathcal{F}_{fc}$ the values of the grasp conditions on all levels of permutation are derived according to equation (4.6). For the case of pair-wise constraints, a number of $\binom{n}{2}$ lists $A_{2,ij}$ of admissible facet pairs, one for each finger pairing (i, j), can be obtained. This is achieved by the merger of the contents of all appropriate bins of H_2. With a measured relative distance Δ_{ij} between two fingers at an object, the admissible bins comprise all containers whose maximum distance is equal to or larger than Δ_{ij} and whose minimum distance is less or equal to Δ_{ij}. Constraints on permutation level 1, e.g. constraints on the reachability of facets for the respective finger i and j, result in two other lists $R_{1,i}$ and $R_{1,j}$. When $A_{2,ij}$ is constructed, those facets not contained in these lists can be disregarded. This is done according to

$$A_{2,ij} = \left\{ (x,y) \mid (x,y) \in \bigcap_{a,b,c} H_2[a,b,c], x \in R_{1,i}, y \in R_{1,j} \right\}$$

with

$$\begin{aligned} a &\in [t_1(\Delta_{ij} - \sigma_\Delta), p_{\Delta max}] \\ b &\in [0, t_2(\Delta_{ij} + \sigma_\Delta)] \\ c &\in [t_3(\alpha_{ij} - \sigma_\alpha), t_3(\alpha_{ij} + \sigma_\alpha)]. \end{aligned} \tag{4.10}$$

In order to compensate for measurement noise and approximation errors when triangulating the object, also neighbouring bins should be included. This is guaranteed by the measurement uncertainty $\sigma_\diamond$. The memory consumption in this step depends on the numberer of admissible facet pairs. The upper bound $\mathrm{size}(\mathrm{A_{2,ij}}) = m^2 \cdot \varepsilon$ is reached in highly symmetric cases such as all symmetric approximations of a sphere. These cases, however, are ill-posed, as no information can be drawn from such a grasp and all contact points are equally good, as long as they comply with the conditions. This is no problem in general, as for grasp control these different configurations are indistinguishable.

Determination of Facet Hypotheses by Selection Tree From the lists $A_{2,ij}$, each containing admissible pairs k and l for fingers i and j, a list of admissible n-tuples has to be computed as generalised intersections of these pair lists. A permutation tree as a common method for discrete optimisation seems useful. In contrast to methods like branch and bound, using the preparation work described

in the previous sections, this section suggests building a reduced tree that does not contain infeasible combinations. At first the $A_{2,ij}$ are sorted by the first and then second facet k and l and indexed with k for a faster access. In order to find n-tuples satisfying all $A_{2,ij}$ the permutation tree T_n is constructed with each tree level corresponding to one finger. Every node in the tree relates the respective facet to the finger with the level of the branch as index. The branches of the tree connect feasible combinations of facets starting at root node via finger 1 to finger n. With a constructed tree, admissible n-tuples can be found by traveling through the tree starting at any node on level 1 along all branches that end on level n and hence present feasible facets for each finger. With here $j = n$, in figure 4.14,

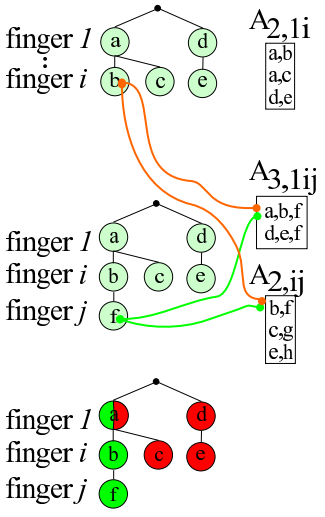

Figure 4.14: Search tree T_n for valid tuples

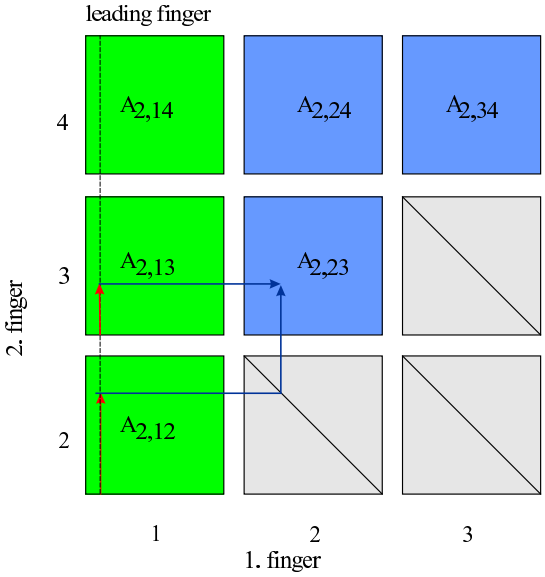

Figure 4.15: Search-tables for pairs

a valid hypothesis is depicted in bright, starting at facet a for finger 1 traveling through finger i with facet b and ending at finger $j = n$ with facet f. Incomplete and hence invalid hypotheses are drawn dark and start at facets a and d for finger 1 ending at facets c and e for finger i. To construct T_n, first $A_{2,12}$ is added to the root node of the tree, as depicted in the upper sketch of figure 4.14. When working through the the list $A_{2,12}$ with entries (k_1, k_2) each new k_1 adds a new node to level 1 connected with a branch to the root node, whereas each new k_2 adds a new node at level 2 and a new branch to node k_1 on level 1.

Then, in order to add level 3, all nodes on level 2 of T_n are parsed horizontally. In the upper illustration of figure 4.14 this contains the nodes b, c and e. Finger two then resides on facet k_2 associated with the currently parsed tree node, finger

one resides on the facet k_1 associated with the parent node of the currently parsed node. This is depicted in the middle illustration of figure 4.14. With fingers one and two assumed on facets (k_1, k_2), the respective lists $A_{2,13}$ and $A_{2,23}$ are compared for a common entry k_3 determining a commonly feasibly facet for the third finger. On success a new branch to and new node r is added at level 3. In figure 4.14 two lists $A_{2,ij}$ and $A_{3,1ij}$ are searched for a common entry from finger j which results in a new node f. This also shows the possibility to generalise the suggested construction scheme to lists of n-tuples, for example $A_{3,1ij}$ is a list of triples. Access to and searching of the lists $A_{2,ij}$ are simplified through sorting and indexing as mentioned above. Thus, instead of searching the whole lists $A_{2,13}$ and $A_{2,23}$ anew each time a new node is added, only those parts which have not previously been searched have to be examined.

Similarly, the nodes on level 3 are parsed and lists $A_{2,14}$, $A_{2,24}$ and $A_{2,34}$ are intersected for a common facet k_4 for finger 4. This is repeated for all n fingers. During the construction of the tree, further grasp conditions can be tested that were not taken into account when constructing the lists $A_{2,ij}$. This is the case in this work with the orientation constraint of equation (4.7). After having constructed the tree T_n, all paths ending at level n represent the hypothesis set $\mathcal{F}_{oc}$ with hypotheses $\vec{h} = k_1, k_2, ..., k_n$ for facets. The hypotheses contain at least one oriented point that obeys the grasp conditions. Again, memory consumption depends on the object and the actual grasp. As presented, this approach is valid also for higher level conditions.

Determination of Facet Hypotheses by Set Comparison Another method that is somewhat faster but less obvious is comparison of sets. For this, one leading finger is chosen, say finger 1. Now all lists $A_{2,1j}$ are sorted and indexed like above. For all other lists $A_{2,ij}, i \neq 1$ an array of Boolean values $\bar{A}_{2,ij}(k, l)$ is created with true on elements $(k, l) \in A_{2,ij}$ and false elsewhere. This is for direct testing of a facet pairing. This array is of size $m \times m$. In order to save storage also for large numbers m of facets, a hash table is used. Now all elements (k_1, k_2) of $A_{2,12}$ are parsed. With k_1 fixed, all elements (k_1, k_3) of $A_{2,13}$ are searched by index and parsed. Now $\bar{A}_{2,23}(k_2, k_3)$ is tested for $true$. If so, with k_1 fixed, all elements (k_1, k_4) of $A_{2,14}$ are parsed. Arrays $\bar{A}_{2,24}(k_2, k_4)$ and $\bar{A}_{2,34}(k_3, k_4)$ are tested for $true$. This continues for lists $A_{2,1n}$, $\bar{A}_{2,2n}(k_2, k_n)$,..., $\bar{A}_{2,(n-1)n}(k_{n-1}, k_n)$. Finally additional grasp conditions such as the orientation constraint are tested at the n-tuple $(k_1, ..., k_n)$. If true, this tuple represents a valid hypothesis $\vec{h} = k_1, k_2, ..., k_n$. This process is shown in figure 4.15.

4.2.3 Continuous Optimisation

In the previous sections, a method was introduced to determine hypotheses $\vec{h}$ for facet tuples that contain at least one oriented point which obeys all grasp conditions. This was done by discrete optimisation. In this section, a method is given to verify those hypotheses and rank them in order to pick out the best. For testing a hypothesis of facets, a transform $\boldsymbol{T}_{(o)}^{(w)}(\vec{\theta},\vec{t}) = \begin{bmatrix} \boldsymbol{R}_{(o)}^{(w)}(\vec{\theta}) & \vec{t}_{(o)}^{(w)} \\ [0,0,0] & 1 \end{bmatrix}$ has to be found that best matches the actually measured oriented points $\in \mathcal{F}_{fc}$ from n fingers given in the world system $S^{(w)}$ to oriented points within the facets of a hypothesis $\vec{h} \in \mathcal{F}_{oc}$ given in object coordinates $S^{(o)}$. This transform depends on the rotation angles $\vec{\theta}$ and the displacement $\vec{t}$ and represents the world's position with respect to $S^{(o)}$, $\left(\boldsymbol{T}_{(o)}^{(w)}\right)^{-1}$ represents the object's position in $S^{(w)}$. With a given hypothesis (i,k) of facet k being touched by finger i, the relative transformation $\boldsymbol{T}_{(o)}^{(w)}$ relates

$$\begin{aligned} \vec{n}_{fc,i}^{(w)} &= -\boldsymbol{R}_{(o)}^{(w)\,T}\,\vec{n}_{oc,k}^{(o)} \\ \vec{x}_{fc,i}^{(w)} &= \boldsymbol{T}_{(o)}^{(w)\,-1}\,\vec{x}_{k}^{(o)}, \end{aligned} \tag{4.11}$$

with $\vec{x}_k^{(o)}$ being a properly chosen point on facet k. The planar description of a facet can be transformed according to

$$\begin{aligned} 0 &= \vec{n}_{oc,k}^{(o)\,T}\,\vec{x}^{(o)} + d_{oc,k}^{(o)} \\ &= \vec{n}_{oc,k}^{(o)\,T}\left(\boldsymbol{R}_{(o)}^{(w)}\vec{x}^{(w)} + \vec{t}_{(o)}^{(w)}\right) + d_{oc,k}^{(o)} \\ &= \left(\boldsymbol{R}_{(o)}^{(w)\,T}\,\vec{n}_{oc,k}^{(o)}\right)^{T}\vec{x}^{(w)} + \left(d_{oc,k}^{(o)} + \vec{n}_{oc,k}^{(o)\,T}\,\vec{t}_{(o)}^{(w)}\right). \end{aligned} \tag{4.12}$$

It is to be noted that the normal vectors of two surfaces in contact are always anti-parallel resulting in the negative sign in the first equation of equation (4.11) (see [Mon95]).

A merit function $\chi_a^2(\vec{\theta},\vec{t},\vec{h}_a)$ can be defined that evaluates the a^{th} facet/finger pairing of a hypothesis $\vec{h}$ with respect to the mismatch between the oriented points of the measurement and those possible within an assumed facet. The function $\chi_a^2(\vec{\theta},\vec{t},\vec{h}_a)$ depends on $\vec{\theta}$ and $\vec{t}$. The minimum value of χ_a^2 determines how good a hypothesis is. In each finger/facet pair $a = (i,k)$ of the hypothesis $\vec{h}$, three conditions have to be considered. The planar representation of an oriented point measurement has to match the plane of the respective facet. In particular, the normals $\vec{n}_{fc,i}^{(w)}$ and $-\vec{n}_{oc,k}^{(w)}$ have to match in order for both planes to be parallel. Also, the distances $d_{fc,i}$ and $d_{oc,k}$ have to match for both planes to be tangential to the same sphere. When both conditions are met, the planes are identical. Third, the

oriented points of the measurement have to lie within the limits of the respective facet for the planar approximation to be valid. Hence the first term $\chi^2_{a,1}(\vec{\theta},\vec{t},\vec{h}_a)$ of $\chi^2_a(\vec{\theta},\vec{t},\vec{h}_a)$ is defined as

$$\chi^2_{a,1}(\vec{\theta},\vec{t},\vec{h}_a) = (\vec{n}^{(w)}_{fc,i} - (-\boldsymbol{R}^{(w)\,T}_{(o)}\,\vec{n}^{(o)}_{oc,k}))^T \boldsymbol{W}_1 (\vec{n}^{(w)}_{fc,i} - (-\,\boldsymbol{R}^{(w)\,T}_{(o)}\,\vec{n}^{(o)}_{oc,k})), \quad (4.13)$$

with $\boldsymbol{W}_1$ being the weight matrix for this part of the merit function. Instead of punishing the angle between the two normal vectors and hence the length of the arc on the unit circle, the length of the difference vector is chosen. This avoids computing $\cos^{-1}$ and uses a secant in the unit circle instead. The comparison is performed in $S^{(w)}$ and the negative sign originates from the anti-parallel surface normals of two faces in contact (see equation (4.11)). The second term of $\chi^2_a(\vec{\theta},\vec{t},\vec{h}_a)$ is defined by

$$\chi^2_{a,2}(\vec{\theta},\vec{t},\vec{h}_a) = W_2 \left(d^{(w)}_{fc,i} - (-d^{(w)}_{oc,k})\right)^2 = \left(d^{(w)}_{fc,i} + d^{(o)}_{oc,k} + (\vec{n}^{(o)}_{oc,k})^T \vec{t}^{(w)}_{(o)}\right)^2, \quad (4.14)$$

with weight W_2. Here again, the negative sign results from opposing surface normals.

A third term is defined to penalise a violation of triangle boundaries within the contact plane. As described in section 4.1.1, a two-dimensional coordinate system $S^{(v)}_{r,k}$ is defined in each vertex r (see equation (4.3)). The coordinates of the measurement $\vec{x}^{(w)}_{fc,i}$ are mapped to the respective systems

$$\begin{aligned} \lambda_{r,k} &= e\vec{p}^{(o)}_{r,k} \left(\boldsymbol{T}^{(w)}_{(o)} \vec{x}^{(w)}_{fc,i} - \vec{x}^{(o)}_{r,k}\right) \\ \kappa_{r,k} &= e\vec{n}^{(o)}_{r,k} \left(\boldsymbol{T}^{(w)}_{(o)} \vec{x}^{(w)}_{fc,i} - \vec{x}^{(o)}_{r,k}\right). \end{aligned} \quad (4.15)$$

With this coordinate representation $(\lambda_{r,k}, \kappa_{r,k})$, the distance of a point of the tangential plane to the facet can be computed. Two cases can occur: Either the path to a vertex or to an edge is shortest. According to figure 4.16 the outside of a facet is divided into six sectors. In even sectors II, IV and VI, the distance is computed to the closest edge. In odd sectors I, III and V the distance is computed to the closest vertex. Sector VII describes the interior of the facet. The boundaries of each sector are shown in table 4.1. The value of the error is computed as the squared distance to the facet as also shown with weight W_3. Finally, the complete merit function takes the form

$$\chi^2(\vec{\theta},\vec{t},\vec{h}) = \frac{1}{2} \sum_{a\in(i,k)} \chi^2_{a,1} + \chi^2_{a,2} + \chi^2_{a,3} \quad (4.16)$$

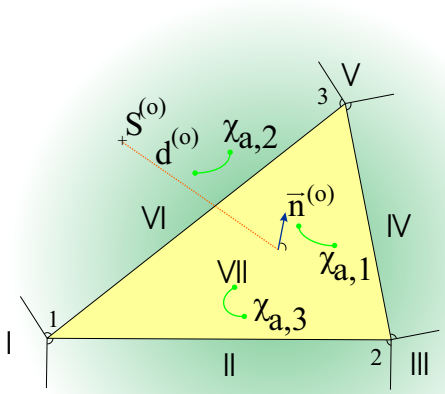

Figure 4.16: Merit functions χ^2_a

As described above, with a given facet hypothesis $\vec{h}$, minimising

$$\chi^2_{min,\vec{h}}(\vec{\theta}_{min,\vec{h}}, \vec{t}_{min,\vec{h}}, \vec{h}) = \min_{\vec{\theta},\vec{t}} \chi^2(\vec{\theta}, \vec{t}, \vec{h}) \tag{4.17}$$

renders the best estimate of the position $\vec{t}_{min,\vec{h}}$ and orientation $\vec{\theta}_{min,\vec{h}}$ of the object with respect to $S^{(w)}$ considering given contact measurements $\mathcal{F}_{fc}$. The value of $\chi^2_{min,\vec{h}}$ itself gives a measure of how good the measurements fit to the assumed facets in the sense of least squares. The optimisation can be done using a standard Levenberg-Marquard algorithm [PTVF92]. The gradient and Hessian of the merit function can be computed explicitly and hence improve computation. Any previous localisation from vision or similar can be taken into account as a starting value.

4.2.4 Probabilistic Interpretation

According to [PTVF92], a least squares problem as given in section 4.2.3 can be also regarded as maximum likelihood estimation. In this sense the presented discrete-continuous optimisation can also be reinterpreted. Assume the n fingers of the robotic hand touch the object at the facets given in $\vec{h}$ and the relative location between object and world is given by $T^{(w)}_{(o)}$. In this case, what is the likelihood of obtaining within a certain range δ the measurement given in $\mathcal{F}_{fc}$? The likelihood

sector number	related vertex	$\lambda_{r,k}$	$\kappa_{r,k}$	$\chi^2_{a,3}(\vec{\theta},\vec{t},\vec{h}_a)$
I	1	$\lambda_{1,k}<0;\lambda_{3,k}>l_{3,k}$		$W_3\left(\lambda^2_{1,k}+\kappa^2_{1,k}\right)$
II	1	$0\leq\lambda_{1,k}\leq l_{1,k}$	$\kappa_{1,k}>0$	$W_3\kappa^2_{1,k}$
III	2	$\lambda_{2,k}<0;\lambda_{1,k}>l_{1,k}$		$W_3\left(\lambda^2_{2,k}+\kappa^2_{2,k}\right)$
IV	2	$0\leq\lambda_{2,k}\leq l_{2,k}$	$\kappa_{2,k}>0$	$W_3\kappa^2_{2,k}$
V	3	$\lambda_{3,k}<0;\lambda_{2,k}>l_{2,k}$		$W_3\left(\lambda^2_{3,k}+\kappa^2_{3,k}\right)$
VI	3	$0\leq\lambda_{3,k}\leq l_{3,k}$	$\kappa_{3,k}>0$	$W_3\kappa^2_{3,k}$
VII			$\kappa_{1,k}\leq 0$ $\kappa_{2,k}\leq 0$ $\kappa_{3,k}\leq 0$	0

Table 4.1: Sectors of distance to facet

of obtaining the exact value is obviously zero. Thus, a small range has to be defined around the exact value. Assuming white Gaussian noise and statistically independent parameters $\vec{h}$ and $T^{(w)}_{(o)}$, the related probability P can be given as

$$P\propto\delta e^{-\chi^2(\vec{\theta},\vec{t},\vec{h})} \tag{4.18}$$

In this case, the weights $\boldsymbol{W}_1$, W_2 and W_3 have to be chosen as the inverse of the covariance matrices of the respective parts of χ^2. These covariance matrices can be derived when the statistical characteristics of the measurement noise and noise in the object model are known. Usually, the noise disturbing the object description can be assumed white Gaussian, affecting the positions of vertices $\left(\vec{x}^{(o)}_{1,k},\vec{x}^{(o)}_{2,k},\vec{x}^{(o)}_{3,k}\right)$ and as a consequence all values dependent on them. The noise disturbing the measured oriented points can also be assumed white Gaussian. Its covariance matrix has to be determined from the actual method of measurement. For simplicity a diagonal matrix is assumed describing independent noise on the parts of position $\vec{x}_{fc}$ and normal $\vec{n}_{oc}$. Considering the nonlinearity of the parts of χ^2, the propagation of uncertainty through the function has to be linearised as

$$\begin{aligned}\vec{y} &= \vec{f}(\vec{x})\\ \mathbf{Cov}(y) &= \boldsymbol{J}(\vec{x})\mathbf{Cov}(x)\boldsymbol{J}(\vec{x})^T,\end{aligned} \tag{4.19}$$

with $\boldsymbol{J}(\vec{x})$ as the Jacobian of $f(\vec{x})$ at point $\vec{x}$. Maximising equation (4.18) is equivalent to minimising the negative logarithm of (4.18) and returns the problem to its initial form of equation (4.16).

4.3 Numerical Examination of the Function χ^2

In this section, the geometrical and numerical properties of the merit function χ^2 and the discrete-continuous optimisation will be examined. Information will be given about the robustness of the process proposed here along with computational details necessary in implementation.

4.3.1 Geometrical Properties of the Function χ^2

At first, the geometrical properties of the individual parts of χ^2 will be examined. As test object, a deformed torus will be used as depicted in brighter in figure 4.17 at the right. The contact position will be determined as the barycentres of randomly drawn facets. The respective facets are marked dark in the depicted torus. The perceived torus as seen from the perspective of the world system $S^{(w)}$ is shifted and rotated. This torus is drawn in dark at the left into the same image. The transformation of $S^{(w)}$ to the object coordinates $S^{(o)}$ is in its translational part $\vec{t} = (4\text{cm}, 1\text{cm}, 2\text{cm})$. The world system $S^{(w)}$ has to be rotated $(0.1\text{rad}, 0.2\text{rad}, 0.1\text{rad})$ radians around its fixed $x-$, $y-$ and $z-$axis to coincide with $S^{(o)}$. Hence, the dark torus has to be shifted along $\vec{t} = (4\text{cm}, 1\text{cm}, 2\text{cm})$ and rotated for $\vec{\theta} = (0.1\text{rad}, 0.2\text{rad}, 0.1\text{rad})$ to coincide with the brighter torus. Also depicted on the dark torus are the surface normals of the measured facets.

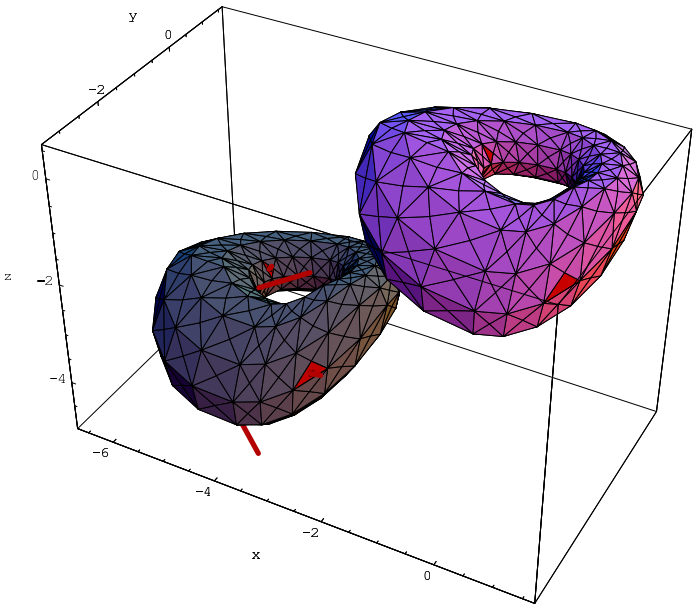

Figure 4.17: Torus, original (bright, right) and as seen from $S^{(w)}$ (dark, left)

Landscape of the Function χ^2

Of particular interest for the behaviour of χ^2 during optimisation is the topology of its error landscape. This landscape represents the value of χ^2 around the true optimum $((0.1\mathrm{rad}, 0.2\mathrm{rad}, 0.1\mathrm{rad}), (4\mathrm{cm}, 1\mathrm{cm}, 2\mathrm{cm}))$ of the continuous parameters $(\vec{\theta}, \vec{t})$ when the discrete parameters, the finger/facet pairings, are at their true values $\vec{h}$ as depicted in figure 4.17. In the following figures, the value of the merit function χ^2 is depicted with two continuous parameters varying. In contour plots, figures 4.18, 4.19 and 4.22 depict the values of $\chi^2(\vec{\theta}, (x, y, 2\mathrm{cm}))$, $\chi^2(\vec{\theta}, (x, 1\mathrm{cm}, z))$ and $\chi^2(\vec{\theta}, (4\mathrm{cm}, y, z))$ respectively. The correct value for x, y, and z in each plot is marked by a black diamond. The plots represent a planar motion of the estimated torus position away from the true value. Similarly, the value of χ^2 over varying rotational parameters is shown in figures 4.20, 4.21 and 4.23. This corresponds to rotating the estimated torus away from its true position around two axes. Any point on the torus moves along the surface of a sphere. The range of the parameters used in this plot represents the situation as seen from an initial guess of zero translation and zero rotation between $S^{(w)}$ and $S^{(o)}$. In the translational directions this range spans the maximum distance of two points on the dark and bright object of figure 4.17 in the direction of each axis. The rotational parameters vary between $[-\pi/2, \pi/2]$. The plots 4.18 through 4.23 are hence global images. The colour range is defined as hue range from red through yellow green, blue, violet to red from values of $1.03 \cdot 10^5$ to $4.23 \cdot 10^6$ according to the colour code in figure 4.24. As can be seen in all six plots, the error landscape has a clearly defined bottom. There are several local maxima with soft edges as for example in figure 4.18 at $(0.75\mathrm{cm}, -1.5\mathrm{cm})$ or even sharp pillar-like peaks or plateaux, in particular as seen in the rotational parameter plots 4.20, 4.21 and 4.23. However, the minima are distinct. The pillars and plateaux in the given plots do not cause local minima in the sense of obstructing a gradient descent to the global minimum. This has also been confirmed by numerous other simulation runs, where no such case was encountered with a local minimum. Over a long range, the error function χ^2 varies over about one and a half decades. Generally, the landscape is strongly non-quadratic in the long range. Hence the components of χ^2 are dominated by nonlinear effects before squaring and summing them as in equations (4.13), (4.14), and (4.16). In figures 4.25, 4.26 and 4.27 a closeup of χ^2 around the minimum value is depicted for a translation in the $Y - X$-plane in two resolutions and for a rotation around the $X-$ and $Y-$ axes. The colouring is again performed as given in figure 4.24. It can be seen in all three plots that with decreasing distance to the minimum, the landscape becomes increasingly quadratic. The effects of nonlinearity vanish. This is to be expected. Parts of the nonlinearity are caused by the nonlinear dependency of χ^2 on the rotational parameters $\vec{\theta}$. This effect vanishes for small angles. Apart from this, the effects of pillars and

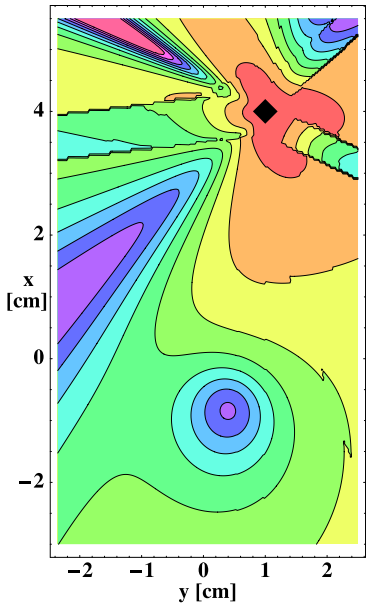

Figure 4.18: Value of χ^2 in a Y-X plane

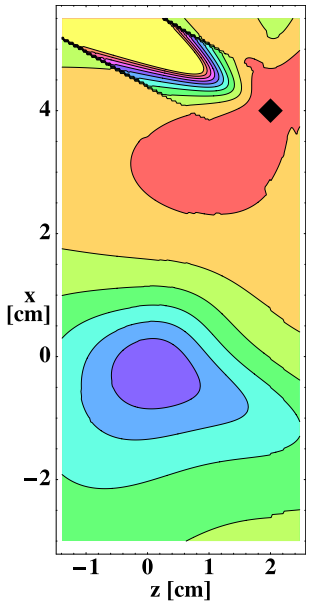

Figure 4.19: Value of χ^2 in a Z-X plane

mountain ranges are caused by the part χ^2_3, determining the distance of a contact point from a given facet.

Effects of Sectors in χ^2_3

Moving parameters away from the minimum value will cause the measured contact points $\vec{x}_{fc}$ to leave the assigned facet. This instantly causes an error χ^2_3 to occur. This error depends on the sector (see table 4.1) in which each finger is located. In figures 4.28, 4.29 and 4.30 the combination of sectors for each finger is determined over two varying parameters, translation in the $Y - X$-plane, in the $Z - X$-plane and in the $Y - Z$-plane. Each combination of sectors is assigned one colour value, and the depicted lines represent the change of a sector for at least one of the 4 fingers. It can bee seen that the density of sector changes is highest close to the minimum value of the parameter. This is caused by the fact that the sectors come closest at the respective triangle. On the other hand, the triangular structure underlying the sectors is still visible, especially in figure 4.28. In figures 4.31, 4.32, and 4.33 the value of χ^2 is overlayed with the lines of sector change. In these pictures, the influence of sector changes on the general shape of the landscape, in particular steep mountain ranges become apparent. In figure 4.32 the range in the upper left part is the result of changes in sectors. Similarly the

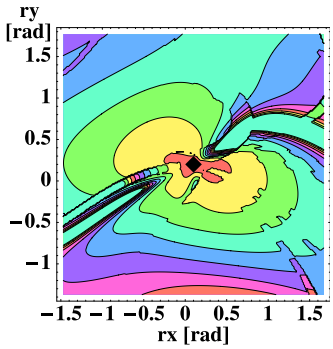

Figure 4.20: Value of χ^2 in a X-Y rotation

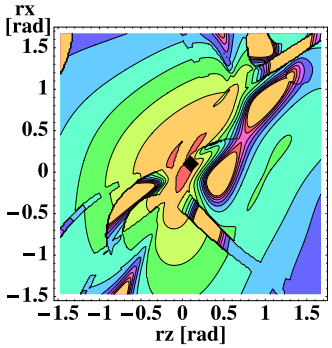

Figure 4.21: Value of χ^2 in a Z-X rotation

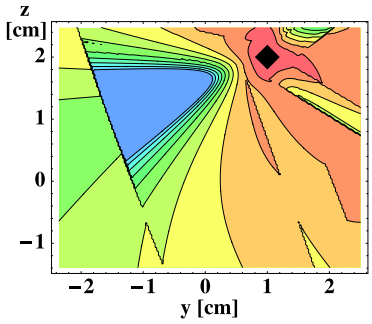

Figure 4.22: Value of χ^2 in a Y-Z plane

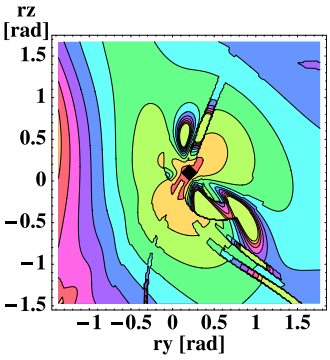

Figure 4.23: Value of χ^2 in a Y-Z rotation

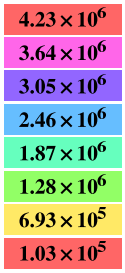

Figure 4.24: Colour bar

star-like structure of the valleys in figure 4.31 has its origin in the sector switches. Also the edge cutting from the upper left to the lower middle of figure 4.33 can be explained this way.

Three-dimensional Structure of χ^2

In figure 4.34 the overlay plots of merit function χ^2 and sector images are commonly depicted in a three-dimensional scene plot. The respective planes represent the values of χ^2 with the 4 non-varying parameters at their minimum value. These planes would intersect at the origin of the violet object. However, for a better visibility, they have been moved out of the scene in a direction orthogonal to the plane itself. In the plot, the motion of $\vec{t} = (4\text{cm}, 1\text{cm}, 2\text{cm})$, necessary to bring the brown torus onto the violet model, can clearly be identified.

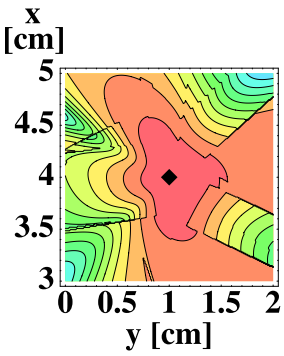

Figure 4.25: Closeup 1 of χ^2 in a Y-X plane

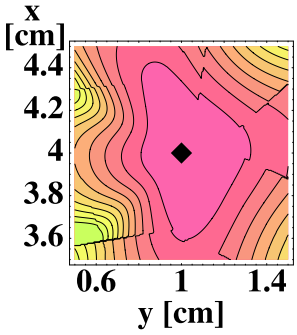

Figure 4.26: Closeup 2 of χ^2 in a Y-X plane

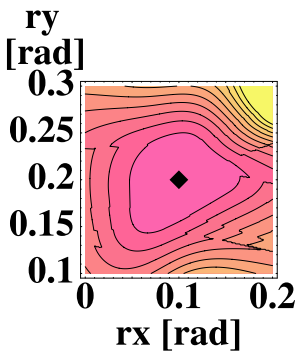

Figure 4.27: Closeup of χ^2 in a X-Y rotation

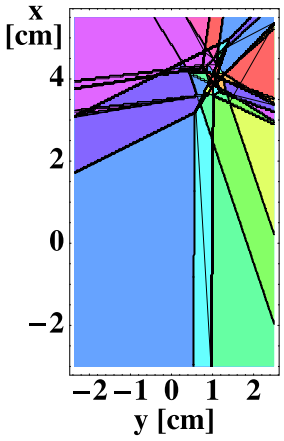

Figure 4.28: Sectors of contacts in Y-X plane

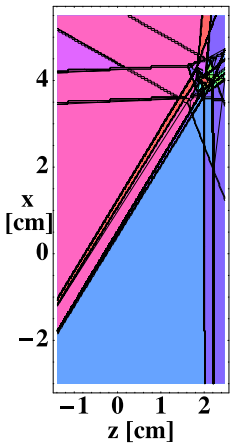

Figure 4.29: Sectors of contacts in Z-X plane

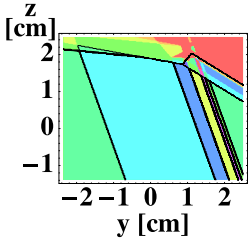

Figure 4.30: Sectors of contacts in Y-Z plane

4.3.2 Implementation Details

As can be seen from the previous section 4.3.1, the algorithm presented here is highly nonlinear. Although local minima could not be found in a number of examinations their existence is not impossible in general. Thus, in order to improve convergence and avoid problems through local minima, special care has to be taken. The algorithm has been implemented such that a first step optimises only the merit function χ_1^2, disregarding the rest. This is a result of the geometrical argument: Each rotation causes significant translation. A translation, however, does not cause any rotation. Optimising only χ_1^2 brings the rotational parameters close to their optimal value. A further shift in rotational parameters occurs later only through possible inconsistencies in the measurement. Then, the resulting error is

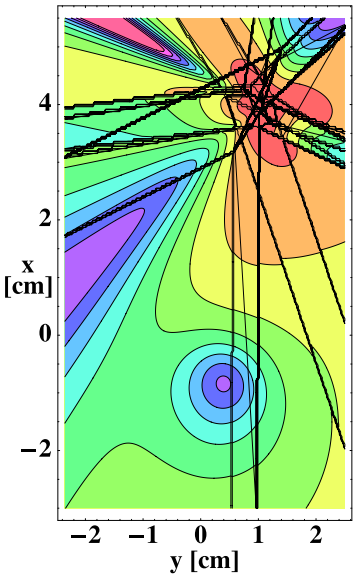

Figure 4.31: Sector/value overlay in Y-X plane

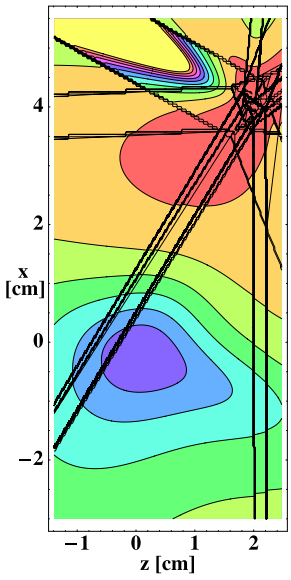

Figure 4.32: Sector/value overlay in Z-X plane

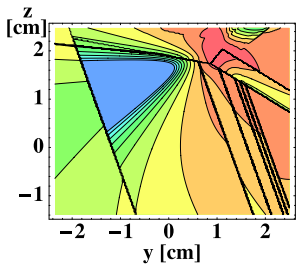

Figure 4.33: Sector/value overlay in Y-Z plane

distributed on several parameters according to their weight in the optimisation. When the minimisation has come closer to an optimal value this way, a standard nonlinear optimisation scheme can be performed. The algorithm of Levenberg-Marquard (see [PTVF92]) proved useful. In larger distance of the optimum a slow but robust descent technique is used whereas in close vicinity of the optimum a closed-form solution to the approximate quadratic problem is determined. Both can be achieved by the solution of a linear vector equation that smoothly transforms between the two cases. In this context the gradient $\vec{g}$ and the Hessian matrix $\boldsymbol{H}$ of the merit function χ^2 have to be computed. The proposed method allows an analytical computation of both. For increased numerical robustness the resulting system of equations can be normalised through dividing each equation by the norm of the respective diagonal entry of the Hessian matrix. Also, when solving the system of linear equations, a Singular Value Decomposition is used. This prevents large motions in the parameter space in the direction of weakly-determined parameter combinations. This may be necessary for example in the case of a cube that is grasped only on the sides but with no contact on either top or bottom. The position of the cube along the common normal of bottom and top face is not determined. This is also required when disabling parts χ_2^2 and χ_3^2 in the merit function, leaving translational parameters undefined. Weakly determined directions cause small singular values in Σ. In these cases, when inverting Σ, the

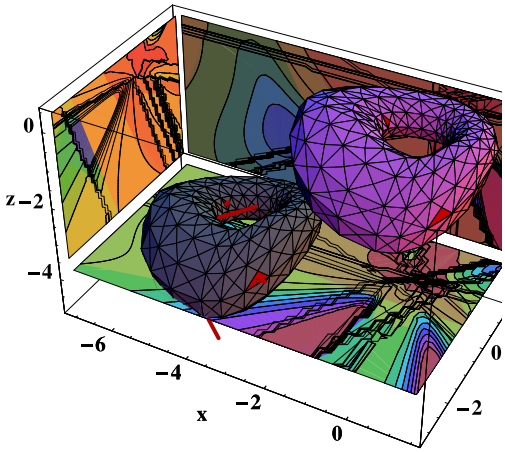

Figure 4.34: Overlay of values/sectors of χ^2 and scene

inverse of a small entry σ is set to zero instead of a large value. The system of equations is briefly outlined in equation (4.20).

$$\begin{aligned} \boldsymbol{H} d\vec{x} &= -\vec{g} \\ \boldsymbol{U}\boldsymbol{\Sigma}\boldsymbol{V}^T d\vec{x} &= -\vec{g} \qquad (4.20) \\ d\vec{x} &= -\boldsymbol{V}\boldsymbol{\Sigma}^{-1}\boldsymbol{U}^T\vec{g} \qquad (4.21) \end{aligned}$$

The performance of the algorithm naturally depends on the number n of fingers contacting an object and on the number m of facets used to describe this object. Additionally it also strongly depends on the ability to sort out facet combinations not compliant with given grasp conditions. A general analysis can thus not be made. Nevertheless it is possible to determine the average magnitude of time consumption during the individual steps in 20 examples. As a sample body, the deformed torus of picture 4.17 will be used. This torus has $m = 800$ facets and is contacted with $n = 4$ fingers. On average, 293 hypotheses had to be tested in each example grasp. The time consumption of steps of the algorithm are individually measured and listed in table 4.2. The test was performed on a Sun-Fire with 4 sparc processors. However, the test was only run on one processor. The performance of a single processor of this machine is comparable to an Intel Pentium II 933 MHz system.

4.4 Simulation Runs and Practical Examples

This section will now examine the performance of the algorithm presented earlier in this chapter by numerical simulations. For all test runs, several sample objects are generated from graphical primitives. Obviously, with only sparse information

step	storage	average time consumption [s]
Preparation of a List of Facet Pairs	P_2	2.9
Preparation of a Hash Table of Facet Pairs	H_2	0.95
Selecting Admissible Facets	$A_{2,ij}$	0.08
Determination of Facet Hypotheses by Set Comparison, Continuous Optimisation	$\vec{h}$	3.59

Table 4.2: Time consumption during steps of detection

available, the given algorithm cannot distinguish between multiple valid solutions for symmetric objects. In real world applications, from the perspective of tactile grasp these multiple solutions are indistinguishable. Hence finding only one is a good result. A limit to this may occur if the weight of the object is to be considered for any reason and valid solutions refer to different distributions of weight. This, however, is beyond the scope of this work. For evaluation purposes comparability of a found solution and a previously-assumed measurement has to be guaranteed. Therefore, to ensure unique, reproducible results, the sample objects are deformed in several directions such that no simple symmetries exist, but sharp edges and general object vertices are preserved. Five sample objects are used: a torus, a cube, a cone, a sphere and a tetrahedron. The properties of these objects are listed in table 4.3. Images are given after the table.

name	no. of vertices	no. of facets	char. length of object [cm]	char. length in facet [cm]	figure
Torus	400	800	3.19	0.353	4.35
Cube	50	96	2.72	0.858	4.36
Sphere	542	1080	3.98	0.358	4.37
Cone	61	80	3.38	1.26	4.38
Tetrahedron	34	64	3.87	1.23	4.39

Table 4.3: Sample objects for evaluation of position detection

In this chapter, a four finger hand is used. Measurements are given relative to the typical length of edges of the object's facets. This is computed as the mean length of all edges in an object. As a reference the typical dimension of the object is also given as $\sqrt[3]{V}$ with V being the volume of the sample object.

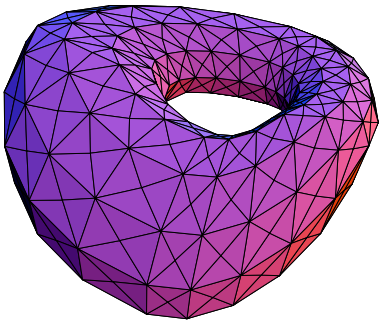

Figure 4.35: Deformed torus

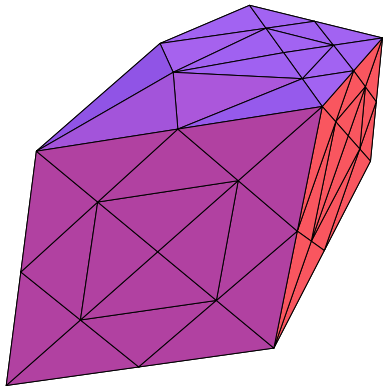

Figure 4.36: Deformed cube

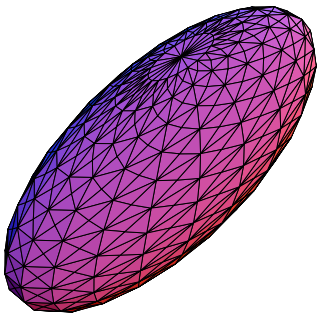

Figure 4.37: Deformed sphere

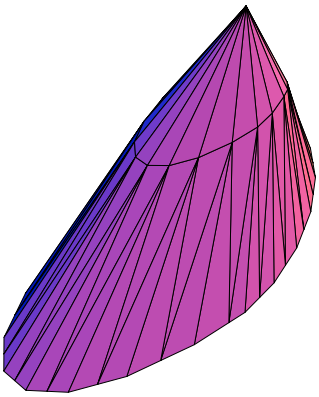

Figure 4.38: Deformed cone

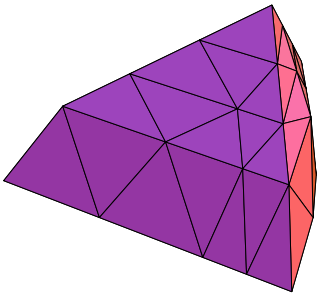

Figure 4.39: Deformed tetrahedron

4.4.1 General Reliability

Randomly, four facets are selected as contact points. The noiseless model is shifted $(10\text{cm}, 0\text{cm}, 5\text{cm})$ and rotated $(5°, 6°, 7°)$ around the three axes of a fixed system. Measurements are taken from the model, consisting of position and normal of a contact point located in the barycentre of the selected facets. In each individual simulation run up to 100 of the best hypotheses for a match between measured impression and model are evaluated. Each hypothesis renders a set of four facets taken as those facets containing the point of contact in the object model. Secondly the translation and rotation are obtained that transform coordinates of the object model given in its own coordinate system to world coordinates used in the measurements. The accuracy and uniqueness of a hypothesis depends

on the chosen grasping points. This dependency on one particular test case is not desirable for a general evaluation. Thus a large number of 150 simulation runs are performed for statistical evaluation.

Reliability of Individual Facet Estimates

At first, the reliability of the best hypothesis compared to the following hypotheses for a set of contact facets and associated object positions is examined. One measure of quality for a given hypothesis is the probability P of obtaining a given measurement, provided reality is as described in the facet hypothesis and position estimate. This probability has been introduced in section 4.2.4. In this chapter, the pairing hypothesis and related position estimate is simply called the estimate.

The statement that an estimate is the best estimate has a high significance when the estimate has an isolated high probability for a given measurement, whereas other estimates have significantly lower probabilities of producing the given measurement. In contrast, the significance of the best estimate is poor when the probability of the given measurement is equally high over a number of estimates.

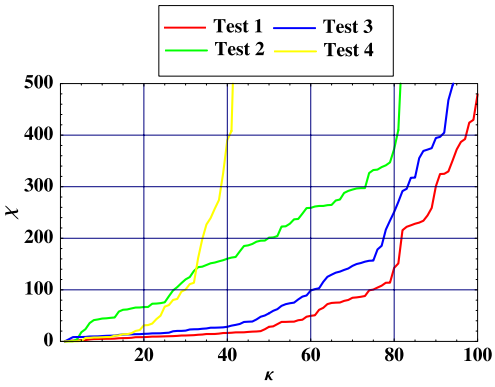

Figure 4.40: Value of χ^2 of a facet hypothesis under 0% noise

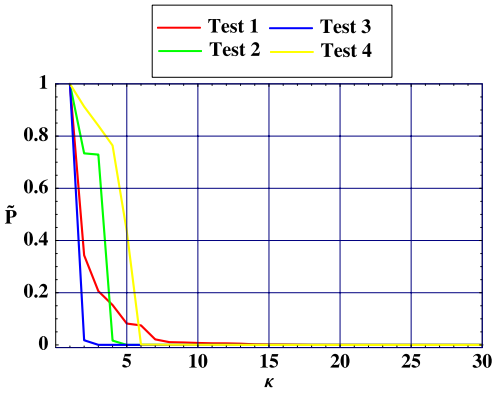

Figure 4.41: Likelihood of a facet hypothesis under 0% noise

For a first examination, the deformed torus is used as sample model with no noise. Four randomly selected test configurations are measured. In figure 4.40 the minimum value of the merit function χ^2 is plotted for the best 100 facet hypotheses of each test case. The cases have been sorted by the value of χ^2. In this type of plot, a flat curve would mean that between estimates the value of χ^2 changes only little. Hence a rating of the relative quality of one estimate with respect to another would be hard. A strongly-increasing curve would indicate a significant distinction in the quality of estimates. For all four test cases, the value of χ^2 is below 10 for the first few estimates in the plot and increases to above 400 for the

hypotheses rated most improbable. The rate of increase, however, depends on the test case. This means that some points of touch of fingers at an object have a higher capability for exactly locating the object, while others vote for several, possibly similar, object positions.

The distinctiveness of estimates is even more clear, when regarding the likelihood $\tilde{P} = e^{-\chi^2}$ of obtaining the given measurement when the facet hypothesis $\vec{h}$ was true. This likelihood is plotted in figure 4.41. In contrast to equation (4.18) the yet unknown proportionality constant is set to 1 in this computation. In order to determine actual probabilities, this constant has to be computed such that $\sum_{\vec{h}} P = 1$. As can be seen here from the unnormalised plot, the likelihood of a measurement given a particular hypothesis $\vec{h}_a$ decreases rapidly to zero. Estimates $\vec{h}_a \in]100, m^n]$ beyond the 100 best estimates have a very low likelihood $\tilde{P}_a$. To achieve comparability this likelihood is set to zero $P_a = 0, a \in]100, m^n]$ and the likelihood of the remaining 100 estimates can be normalised such that $\sum_{a=1}^{100} P_a = 1$.

In order to determine the significance of the probability P_a as a measure, a statement has to be made about how similar estimated and simulated facet tuples are. Similar facet tuples describe contact positions in the same region on the surface, whereas if the facet tuples are not similar they refer to different points of contact in the simulation on the one hand and in the estimate on the other hand. For this purpose a cumulative facet distance d is defined as $d = \sum_1^4 (\|\hat{\vec{x}}_{oc,i} - \vec{x}_{oc,i}\|)$, with $\hat{\vec{x}}_{oc,i}$ being the barycentre of the estimated facet i. In figure 4.42 the evolution of this cumulative facet distance here over up to 300 best facet hypotheses $\vec{h}_a, a \in [1, 300]$ is depicted. First, it can be seen that in test cases 1, 3 and 4 the total number of facet estimates is already limited to 145, 168 and 88 respectively by the grasp conditions despite a generous tolerance σ_Δ and σ_α. This confirms the previous assumption of $P_a = 0$ for larger a. Second, approximately the first ten facet hypotheses have significantly smaller cumulative distance than the remaining hypotheses. It is less than $0.5\mathrm{cm}$ which is in the range of four times the characteristic length of a facet of $4 \cdot 0.353\mathrm{cm} = 1.412\mathrm{cm}$. The multiplication by four corresponds to the sum of four distances in the computation of cumulative distance. In these estimates, none or only one of the four facets misses the simulated value. Regarding the cumulative distance in estimates $a \in [10, 100]$, the value corresponds to four times the average distance within one facet of $4 \cdot 0.353\mathrm{cm} = 1.412\mathrm{cm}$ (see table 4.3). This value is to be expected as these estimated facet tuples lie in the immediate neighbourhood of the simulated configuration. Only a slight tendency for d to increase can be seen. The variation between successive hypotheses is dominant. Assuming a minimum neighbourhood of 6 facets per examined facet, this generates $6^4 = 1296$ hypotheses. All the hypotheses represent geometrically similar configurations to the simulated one. Thus other, minor factors determine the

quality of the match beyond the 10 best estimates and hence explain the large variations without significant trend. This, however, is an indication for the robustness of the algorithm. Obviously only the immediate surroundings of the simulated value are taken in consideration as hypothesis.

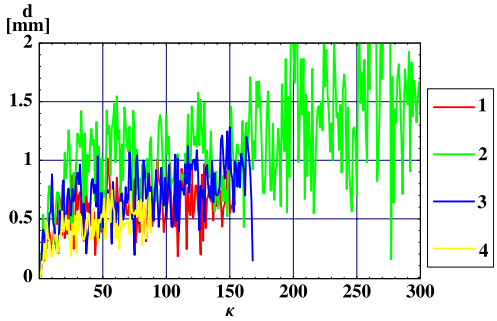

Figure 4.42: Cumulative distance of a facet hypothesis under 0% noise

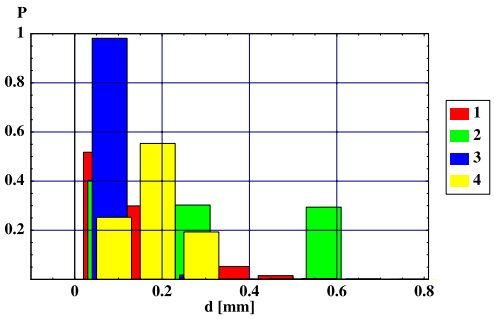

Figure 4.43: Probability distribution of cumulative distance under 0% noise

In order to determine the likeliness of obtaining a hypothesis with a particular cumulative distance, for figure 4.43 the 100 best hypotheses are grouped into classes of similar cumulative distance d. For each class the associated probability P is depicted. Of course, the results show a general dependency of the reliability of estimate on the particular test case. However, the most likely cases lie at values of $d < 0.2\text{cm}$. This is significantly below the typical distance 0.353cm in a triangle. The probability decreases to zero with higher distances. This again proves the solidity of the estimate.

Reliability for Several Estimates

The evaluation of the results given above only allows conclusions about the particularly selected simulation runs. To overcome this limitation, the probability distributions of the previous section, namely of the cumulative distance d over the 100 best estimates, are compared for 150 different test runs.

At first the expected values of the probability distributions of d are compared. The expected value is defined according to as $\bar{d} = \sum_a d_a \cdot P_a$. Figure 4.44 shows that the prediction is closely gathered around 0 throughout the 150 test cases. There is only one isolated outlier and all other expected values are less than a typical distance 0.353cm away from the true value. Note again that the cumulative distance is the sum over the distances of four contacts. If all contacts were one facet away, a typical cumulative distance would be $4 \cdot 0.353\text{cm} = 1.412\text{cm}$.

Another characteristic of a distribution is its entropy, a measure of how closely all values are gathered around the expected value. The entropy is defined in

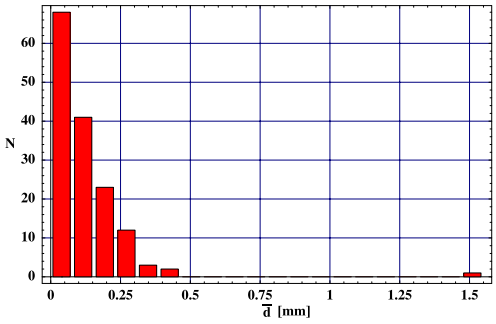

Figure 4.44: Distribution of cumulative distance over 150 test cases under 0% noise

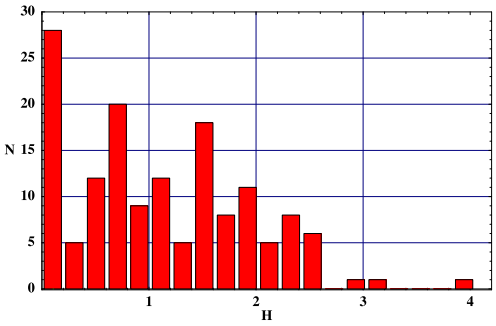

Figure 4.45: Distribution of entropy over 150 test cases under 0% noise

[Kre91] as $H = -\sum_a P_a \ln P_a$. In the case of a homogeneously flat distribution of 100 estimates it takes the value $H = -\sum_{100} 1/100 \ln(1/100) = \ln(100) = 4.6$. In the other extreme, when the distribution has only one isolated peak the entropy takes the value $H = 1 \cdot \ln(1) = 0$. Accordingly, in figure 4.45 the entropy of the probability distributions over the 100 best estimates in 150 test cases is depicted in a histogram. The entropy for these test cases of 0% noise in the setup is low in most runs, and in all runs significantly far away from an even distribution. The number of counted runs decreases in bins with higher values of the entropy. It can hence be concluded that the choice of a best hypothesis as estimate is meaningful as it differs from other hypotheses significantly in quality.

Concluding, both the choice of the geometric location of an estimate as well as the significance of a particular choice is reasonable. This has been tested over a large number of 150 trials. In a few test cases there are, however, facet configurations that are almost equally good and close to indistinguishable. It is these configurations that are most likely to be influenced by measurement disturbances. This, however, poses no problem, as these tests proved that all these configurations lie in close vicinity to the simulated configuration and are hence also indistinguishable in geometric terms. Consequently they can be considered to be equally good estimates.

4.4.2 Validity of Results on Different Objects

Finally, the general validity of the results of simulation is verified for the additional test objects of figures 4.36 through 4.39. The same examination is performed as described in section 4.4.1 for the model of a deformed torus.

In figures 4.46 and 4.47, the results are depicted for a deformed cube. The typical length of a facet in this model is $0.858\mathrm{cm}$ and the typical length of the

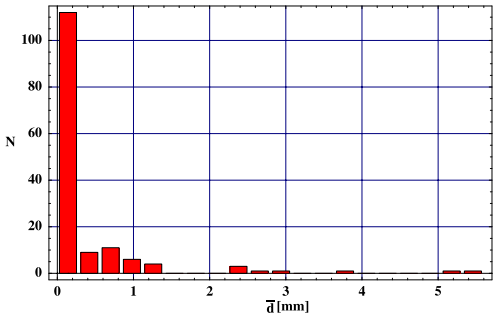

Figure 4.46: Distribution of cumulative distance for a deformed cube under 0% noise

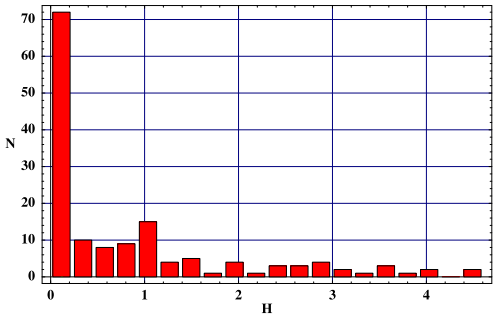

Figure 4.47: Distribution of entropy for a deformed cube under 0% noise

object is 2.72cm. Again, a distinct peak around an expected cumulative distance of 0 can be noted. The expected values of only a few test runs were in the range of $[0\text{cm}; 1.4\text{cm} = 4 \cdot 0.34\text{cm}]$. This is again below the typical distance. Only 3 test runs had an expected cumulative distance of more than $4 \cdot 0.858\text{cm} = 3.432\text{cm}$. Also the entropy distribution is very clear. A large peak can be seen around 0. Only very few runs did not allow a significant decision on one best hypothesis. The decisions could be made with more significance in the case of the cube than in the case of the torus (see figures 4.46 and 4.47).

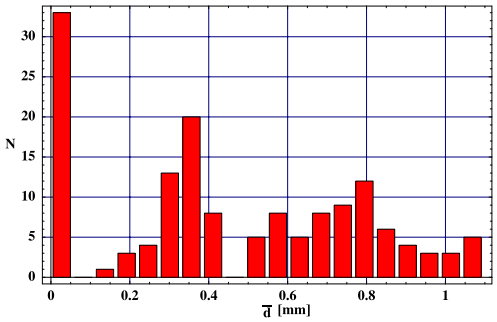

Figure 4.48: Distribution of cumulative distance for a deformed cone under 0% noise

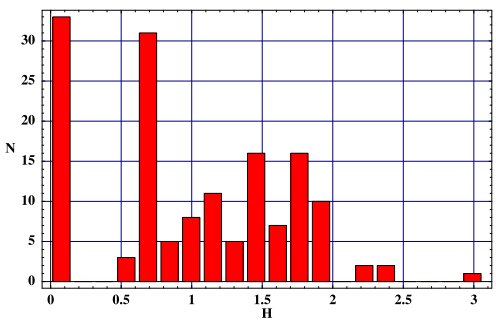

Figure 4.49: Distribution of entropy for a deformed cone under 0% noise

For the case of a cone, the results are depicted in figures 4.48 and 4.49. The typical distance of facets in this object is 1.26cm and the typical length of the object is 3.38cm. Also in this object, the expected cumulative distance peaks around 0. However, a second peak can be spotted at 0.35cm. This peak represents those hypotheses that contain one facet which is neighbouring the simulated one in the direction parallel to the cone's bottom plane. Similarly the third peak at 0.8cm can

be explained. Obviously the previous rotational symmetry of the now deformed torus is still visible. The measure of a typical distance in a triangle is, in this particular case, not useful as a significant part of facets are very long but narrow. The plot of entropy also mirrors this ambiguity. In some test runs, obviously a facet combination was simulated that is very distinctive. In others, several hypotheses had similar likeliness. Hence, the peak around 0 is not as particular as in the previous cases. Especially, the second peak at an entropy of $0.7 \approx -\sum_2 1/2 \ln(1/2)$ can be explained by 2 hypotheses having similar likeliness. This exhibits the original symmetry of the cone. Generally, however, all test cases were still far away from an even distribution and the values of expected cumulative distance still show that the most likely hypotheses are in the neighbourhood of the simulated contact points.

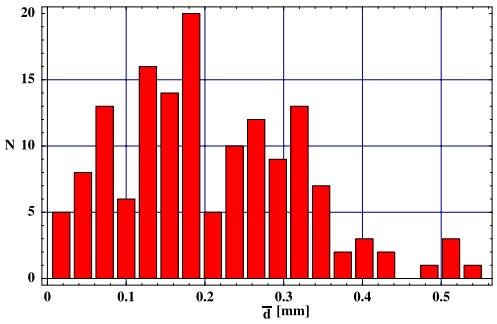

Figure 4.50: Distribution of cumulative distance for a deformed sphere under 0% noise

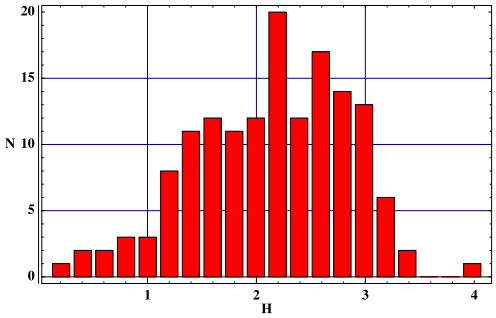

Figure 4.51: Distribution of entropy for a deformed sphere under 0% noise

The behaviour seen at the cone is even more obvious for the deformed sphere. The sphere has a characteristic length within a facet of $0.358\mathrm{cm}$ and a typical object dimension of $3.98\mathrm{cm}$. The topological structure of the sphere is such that a facet has a total of 14 neighbours. Four of the neighbours are about 60% of the average edge length within one facet away. This corresponds to an average of $0.22\mathrm{cm}$ throughout the object. The other neighbours have a larger distance. Figure 4.50 shows the distribution of $\bar{d}$ over the test runs. Only a few test runs had an expected value around 0. A peak occurs at $\bar{d} = 0.18\mathrm{cm}$. This represents half the typical distance of a facet and is hence slightly less than the 60% of a typical distance, the distance between the closest neighbouring facets. The 100 best hypotheses throughout the 150 test runs are hence closely gathered around the true hypothesis at a distance which indicates that one finger is in a neighbouring facet. The distribution of the entropy values is shown in figure 4.51. Here the most hits have been achieved at an entropy of 2.2. This corresponds to nine equally probable hypotheses in a test run. From the geometrical consideration above,

we know that there are 14 facets neighbouring the true choice with increasing distance. Hence an entropy value of 2.2 also corresponds to a distinctiveness of the region around the true value. It is to be noted again that, in this examination, the best hypothesis of a single test run is not examined. Instead, the 100 most probable hypotheses are examined with respect to how distinct the best hypothesis is and how different these hypotheses are, i.e. whether they vote for similar grasps. In this context it can be stated that, even in the difficult case of a deformed sphere, the 100 best hypotheses throughout the 150 test runs are closely gathered around the true hypothesis at a distance which indicates that one finger is in a neighbouring facet.

In contrast to the two cases before, the last test case, the deformed tetrahedron, is an example for a body that is extremely good for position estimation. The typical length of a facet in this object is $1.23\mathrm{cm}$. The typical dimension of the object is $3.87\mathrm{cm}$. As shown in figure 4.52, throughout the 150 test runs the expected value of $\bar{d}$ is less than 25% of a typical facet distance. Also the entropy (see figure 4.53) is below 0.2. For this object, regardless of the grasp, as long as it is not completely degenerate, a very distinct choice of the best hypothesis can be made.

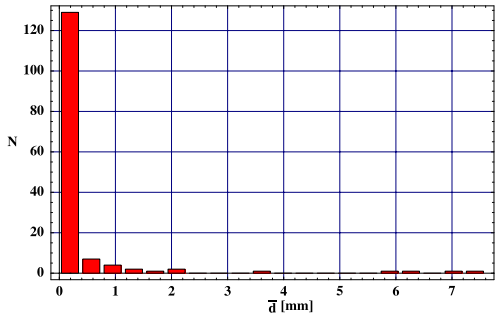

Figure 4.52: Distribution of cumulative distance for a deformed tetrahedron under 0% noise

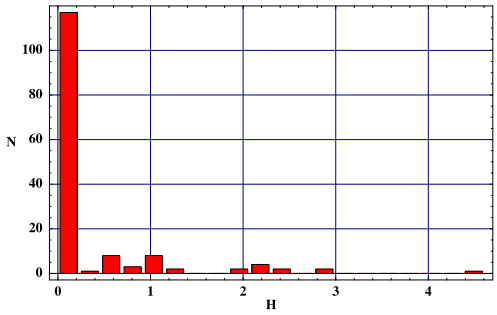

Figure 4.53: Distribution of entropy for a deformed tetrahedron under 0% noise

For all objects and general, not degenerate grasps it can hence be stated that the choice of the best hypothesis as estimate for the true contact locations is meaningful and also the next likely hypotheses vote for similar grasps.

4.4.3 Robustness of Estimate against Noise

Now, after examining the stability of the presented algorithm in general, in this section a conclusion is to be drawn on its robustness against noise in the measurement. In order to simulate an inaccurate model, the position of the model vertices are disturbed by white Gaussian noise with zero mean and a standard deviation

of $\rho \in \{1\%, 2\%, 3\%\}$ of the typical length of edges of the object's facets. In this section, the simulated measurements were taken from the true object model. The disturbed object, however, was given as reference object model to the algorithm. In this simulation, only 50 test runs were performed. In the following plots, the different levels of noise are depicted together, with 1% of noise shown as red, 2% of noise as green and 3% of noise as blue bars.

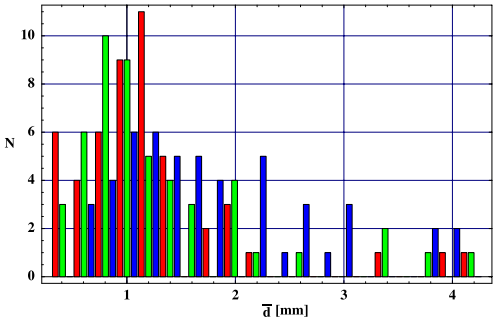

Figure 4.54: Distribution of cumulative distance for a deformed cube under 1%-3% noise

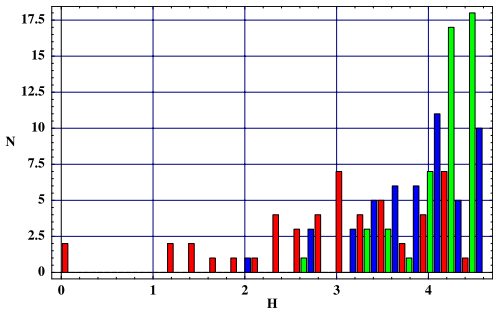

Figure 4.55: Distribution of entropy for a deformed cube under 1%-3% noise

In figures 4.54 and 4.55, the expected values and the entropy of the probability distributions of 50 test runs are depicted for the deformed cube. The cube has a typical facet length of 0.858cm. For the cases of 1% and 2% of noise, most expected values are located around 1cm having only single cases beyond that maximum. This corresponds to a close neighbourhood to the true facet hypothesis with one finger at another facet. A different observation can be made when regarding the associated values of entropy. While in the case of 1% of noise most values of entropy lie in the range between 3 and 4, in the case of 2% of noise those values are narrowly gathered around 4.4 which is very close to the value of 4.6 for an even distribution. So, while in the first case it is still reasonable to consider the best estimate, in the second case all hypotheses are almost equally good. Nevertheless, as the expected values above suggest, in the latter case even when picking any of these equally good hypotheses, the cumulative distance is still small and hence the geometrical location of the 100 best hypotheses is also similar. For the case of 3% of noise, most expected values of cumulative distance are in the range of 1cm to $2.2\text{cm} = 4 \cdot 0.55\text{cm} = 3 \cdot 0.73\text{cm}$. Here, more than one finger is on a neighbouring facet but all fingers still remain in a neighbourhood around the true facet hypothesis. Not surprisingly, here also the value of the entropy is in most cases that of an even distribution. In all cases, despite the noise on the object model, the 100 best facet hypotheses are still closely gathered around the true value although they get less distinguishable with an increasing amount of noise.

In contrast to the previous observation, the contact locations at a deformed tetrahedron can be detected even with higher levels of noise. The typical facet length in the deformed tetrahedron is $1.23\mathrm{cm}$. As figures 4.56 and 4.57 show, most expected cumulative distances $\bar{d}$ are gathered in the range between $1\mathrm{cm}$ and $2\mathrm{cm}$ for all three levels of noise. This corresponds to some hypotheses with one finger at a neighbouring facet and few hypotheses with two fingers in vicinity of the true facet. Also, the distinctiveness of the best hypothesis is still granted: The values of entropy increase with increasing level of noise. Nevertheless they are still below the value of an even distribution.

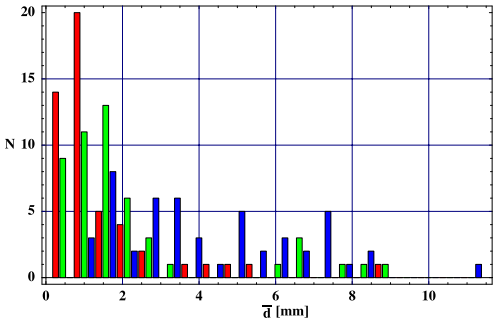

Figure 4.56: Distribution of cumulative distance for a deformed tetrahedron under 1%-3% noise

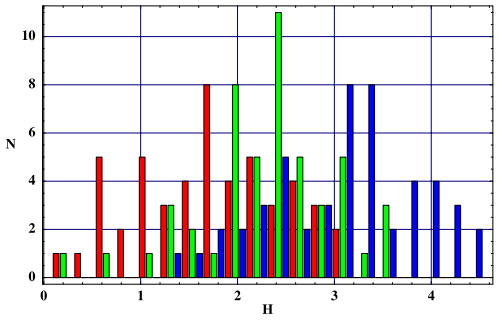

Figure 4.57: Distribution of entropy for a deformed tetrahedron under 1%-3% noise

Summarising the findings of this section, the quality of the estimate depends first of all on the distinctiveness of contact points and secondly on the distinctiveness of the grasped object. Simulations however have shown that the location of contact points on the object can be determined to a close neighbourhood of the true value, including where there is limited measurement noise. The meaning of one single “best” hypothesis decreases however with increasing level of noise. In the case of strong noise and hence a large amount of similarly good estimates, which do not correspond to geometrically-similar contact points at the object, the algorithm presented here has to be extended to include further knowledge, for example about impossible contact locations. This is similar to man picking up for example a cup blindly, knowing to grasp it from the outside, not from the inside.

Concluding this chapter, it can be said that from the knowledge of a geometrical model of a grasped object and from the measurement of contact points and contact normals as seen from the fingers, the positions of the contact as seen from the object and the position of the object can be determined. Numerical evaluations showed that the choice of a particular contact location at the object, i.e. the choice of particular facets of the geometrical model of the object, is meaningful for a variety of objects and levels of noise.

Chapter 5

Experiments with DLR Hand II

In the previous chapters, three algorithms were developed, to detect the point of contact and the position of the object during robotic grasping. These algorithms can improve the robustness of picking up an object by a robot hand in real world scenarios: In contrast to carefully arranged laboratory setups, there, disturbances usually prevent the execution of a task exactly the way it was planned. This section now proves the real world suitability of the presented approaches in experiments with the DLR Hand II (see figure 5.1).

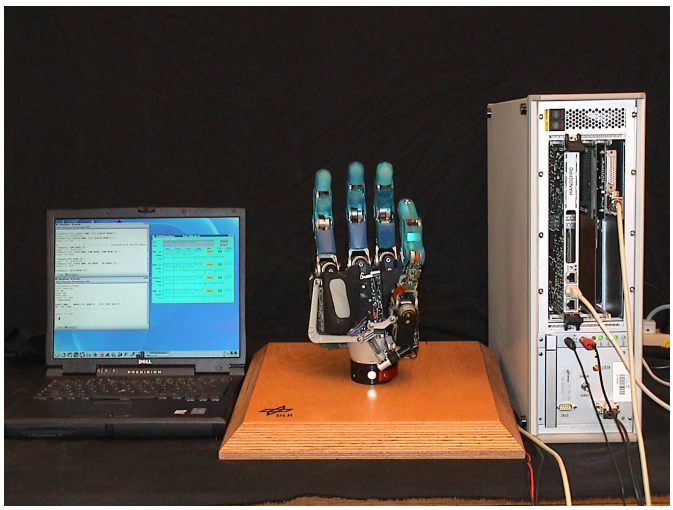

Figure 5.1: Experimental setup of the DLR Hand II

At first, the course of the experiment and the required setup is described in section 5.1. In section 5.2, experiments on the detection of the contact point using kinematic constraints is presented and the performance of computation is evaluated. With the obtained contact points, in section 5.3, the position of the object is determined

5.1 Experimental Setup of the DLR Hand II

In this chapter, the grasping experiments are performed with the DLR Hand II, already described in section 2.1.1. One major design goal for this hand was "modularity", allowing to exchange components on each level of implementation from hardware through actor/sensor electronics and data transmission up to the different levels of control. This modularity allows easy adjustment of the whole system DLR Hand II to different setups as well as the rapid implementation of new features. The concept of modularity requires self contained units for each level: The hand system as a whole is self contained and can thus be operated stand-alone as shown in figure 5.1 and also be mounted on different robot arms (see figure 1.1). Each finger of the hand also represents one module and is hence exchangeable with another finger. Similarly, control systems are plugged together from individual modules in order to rearrange the controller for different tasks.

The data management reflects this modularity of components: Each finger has one FPGA, which collects and bundles the measured data and broadcasts a package of values to a palm control FPGA. This FPGA again collects the data of all fingers and routes it through a serial cable to an external industrial power-pc (in the right of picture 5.1). In this computer low-level control tasks as position control of individual fingers are performed. The hardware unit is interfacing another power-pc in the same rack which is performing higher level controls as motion generation. Low level and task level control are operated at a rate of $1\mathrm{kHz}$. In the experiments, the measurements are transfered to the external user level using a TCP/IP connection to a standard Linux PC for storage. This connection is not time critical. All algorithms are intended for open loop usage and moderate signal delay is hence not an issue. The external user level (laptop in the left of picture 5.1) is not generally required for experiments and is used here for convenience of operation. For a more detailed description of the hard- and software setup, the reader is referred to [HBF+03]. For general applications of the hand see [BFH+03a]. In contrast to these applications, the hand is operated stand-alone without robotic arm to clearly demonstrate the performance of the algorithms presented in this thesis.

In the experiment, the fingers of the DLR Hand II approach a mocca maker (see figure 5.2). No a-priori knowledge about the position of the object or the contact points of the fingers is available. Hence, as the fingers make contact, a heuristically determined grasping motion towards the object is initiated. In order to determine the point of contact, the method exploiting kinematical constraints is chosen. This method evaluates velocity measurements. Therefore, after contacting the object, the fingers perform a generic motion, which moves the object in the hand and the fingers along the surface of the object. In order not to loose contact while moving, the fingers are controlled using an impedance control scheme:

The repositioning force of each finger is proportional to the deviation from it's desired position, the fingers behave like a mechanical spring. Thus, all fingers can, to some extend, perform a motion without coordinating the individual trajectories of each finger. Due to the lack of knowledge about the individual contact positions and contact normals, no coordinated motion can be described yet. As the finger tips of the DLR Hand II are spherical and covered with silicone, translations at the contact point along the surface are inhibited while rolling and twist along the surface normal is possible. From the velocity measurements obtained during the motion, the finger contact position can be estimated by the algorithm presented in section 3.1.

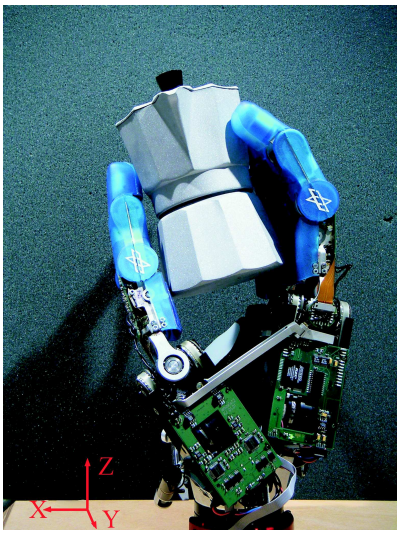

Figure 5.2: DLR Hand II grasping a mocca maker

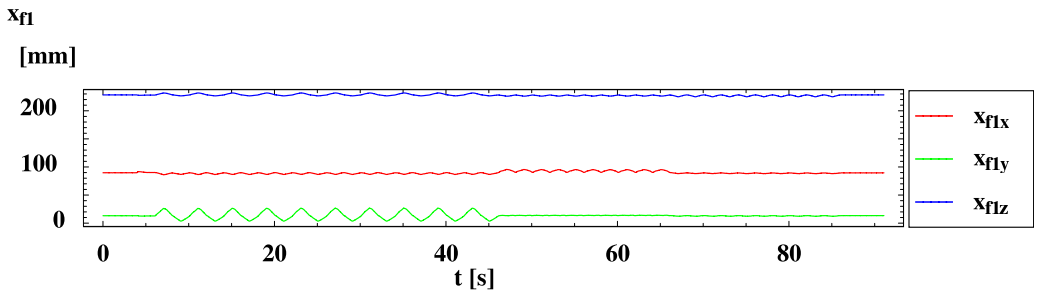

Figure 5.3: Position of the thumb

In this experiment, the thumb has been chosen to lead all exploratory motions. Index, middle and ring finger move mostly in response to these motions as a result of the impedance control law. In only a few instances of the exploratory motion the impedance control is supported by a heuristic, small motion of the three rear fingers in order to guarantee a satisfying contact force. At first, the thumb is moved from left to right for $40s$ also moving slightly towards the other fingers, hence moving along an ellipsoid. Then, from the initial position again, this finger is moved forward and backwards for $20s$ and finally moved up and down for another $20s$ (see figure 5.3). The translational velocities of the centre of the thumb's tip sphere are depicted in figure 5.4. Note, that this motion is caused by a plain *rolling* motion along the contact.

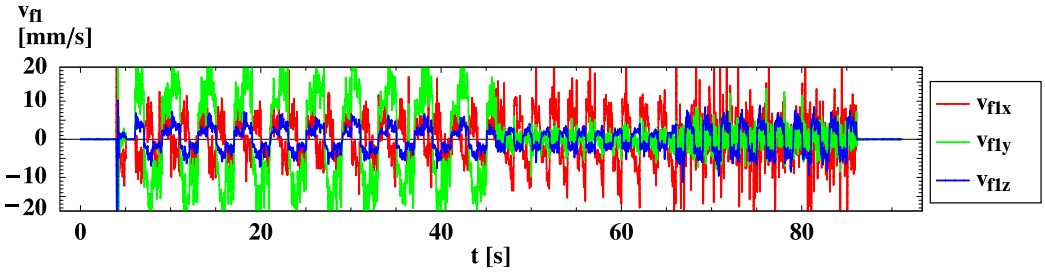

Figure 5.4: Translational velocities of the thumb

5.2 Contact Point from Kinematic Constraints

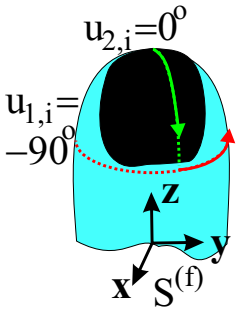

Figure 5.5: Contact parameters

At first, the motion of the fingers is evaluated according to section 3.1: Both, Cartesian position and Cartesian velocity of the finger tip reference is used to estimate the contact location and contact velocity on the surface of the finger tip, which is spherical with radius $12.5\mathrm{mm}$ in the region of interest. The location is described by the two contact joint angles longitude (u_1) and latitude (u_2) as illustrated in figure 5.5. For the evaluation of the experiment, the observer described in section 3.1.4 is applied. Two separate systems are used, each working on groups of three fingers. System *a* estimates the contact position of thumb, index and middle finger. System *b* estimates the contact position of thumb, middle and ring finger. Parting the fingers of the hand shows the applicability of the approach for the minimum amount of fingers working in a grasp, namely three, and also allows a comparison between the two estimates. The initial values for the longitudinal parameters of each finger are set to $0°$ while the latitudes are set to $30°$. The standard deviation for the translational velocities is $20\mathrm{mm/s}$ and for the angular velocities $11°/\mathrm{s}$. The initial standard deviation of estimate is $81°/\mathrm{s}$ for the contact velocities and $18°$ for the contact joint angles. After each step, the state covariance is updated and system uncertainty is added. This system uncertainty is velocity dependent for the contact joint angles and acceleration dependent for the contact velocities. An uncertainty of 100% of the last change in contact position and 200% of the last change in contact velocity is used. The result of the estimate for the longitudinal parameters of system *a* and *b* are shown in figures 5.6 and 5.7. The latitudinal parameters are depicted in figures 5.8 and 5.9. Figure 5.10 depicts the square root of the diagonal entries of the covariance matrix of the contact states of system *a*, solid for latitudes and dashed for longitudes. Provided, the assumption on noise in the measurement and on uncertainty in the dynamics of the states is properly chosen, these numbers represent the standard deviation of the estimates of the re-

spective states. In any case, however, the values indicate the range of uncertainty within the estimates. In order to relate the development of the standard deviation of estimates to the motion of the fingers, the velocity of both contact parameters at the thumb is also sketched in these figures. For comparison, absolute values of the velocity are irrelevant. Thus, lines are scaled by the factor of three and shifted by 2 and -1 respectively to improve visibility in the plot. In figure 5.11, the curvature of the first, estimation correction part of χ is depicted in both directions of surface parameters, u_{11} (red) and u_{12} (green), of the thumb. For comparison, again the respective parameter velocities are also depicted scaled and shifted in the same colours.

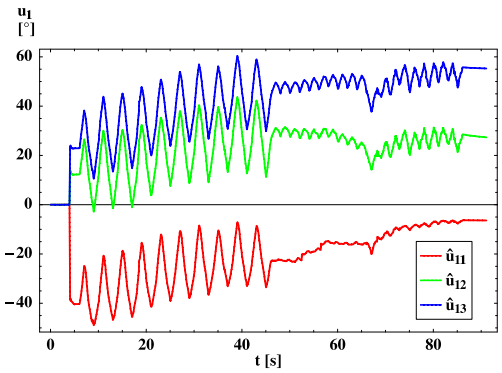

Figure 5.6: Longitudinal angles of thumb, index and middle finger

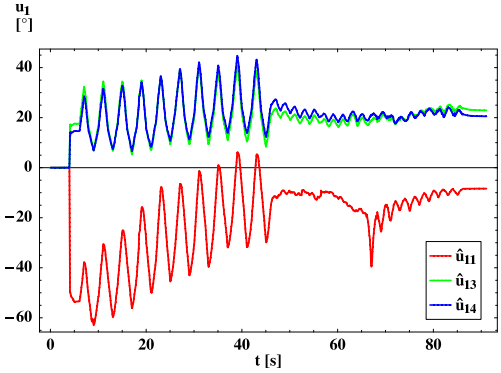

Figure 5.7: Longitudinal angles of thumb, middle and ring finger

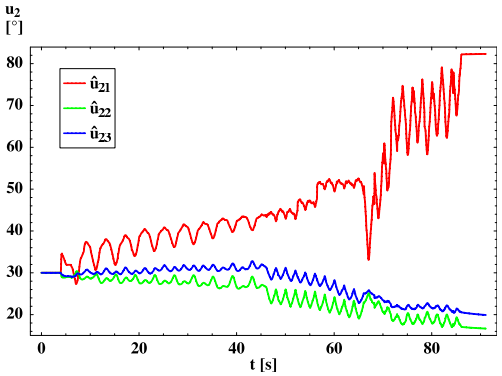

Figure 5.8: Latitudinal angles of thumb, index and middle finger

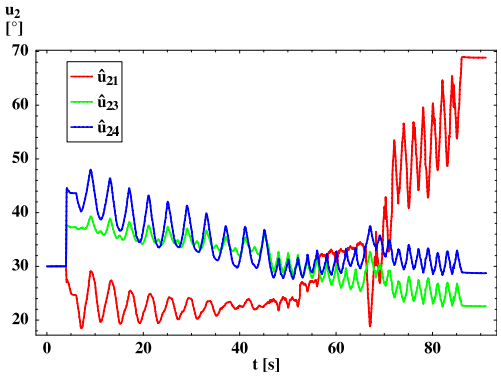

Figure 5.9: Latitudinal angles of thumb, middle and ring finger

Throughout all four plots of contact parameters, the velocity of the finger is clearly visible also in a motion of the contact angles. For the first 40s, during the

ellipsoidal left/right motion of the thumb, the estimated longitude of the contact points changes significantly, while the latitude varies only little. For the next 20s, while the finger is moving back and forth, the change is generally smaller. However, more change is seen in the latitudes than in longitudes. Finally, during the last 20s the change in latitudes is significant, while the change in longitudes is small. Also obvious is the steady behaviour in the beginning and the end of the experiment, where the fingers did not move. Here, no information about a possible error in the estimated contact angles can be obtained. The observer hence maintains its actual value.

Comparing the longitude of the thumb in system *a* and *b* it can bee seen, that after 40s both longitudes converged to close values of $-20°$ and $-10°$. On the other hand, the latitudes differ more. The left/right ellipsoidal motion causes a rolling across longitudes and somewhat across latitudes. Hence, in principle, the curvature of the first, estimate correcting part of χ is higher in the direction of latitudes and lower for longitudes (see figure 5.11). Nevertheless, the uncertainty inflicted through motion is lower in the direction of latitudes. Thus, the second, memory term in χ keeps the values of latitude changing slower than the longitudes. This can also be observed in the plot of standard deviation 5.10. The uncertainty on the thumb's longitudinal parameter decreases from $19°$ right after the start of the motion to $15°$ in system *a*. On the other hand, the uncertainty in latitudes decreases to $7°$.

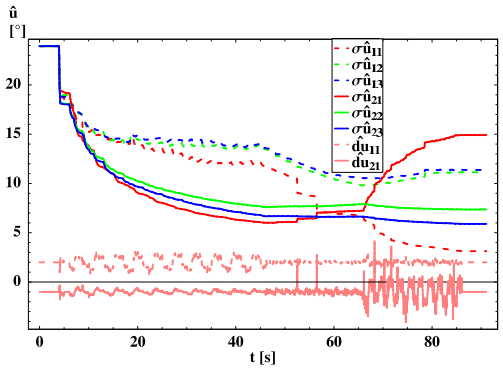

Figure 5.10: Standard deviation of thumb, index and middle finger

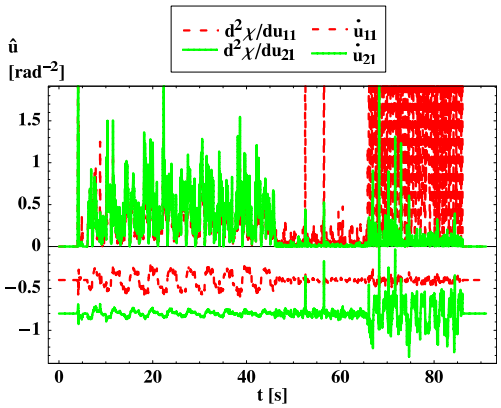

Figure 5.11: Curvature of correction part of χ for thumb in sys. *a*

During the following two phases of motion for the thumb, the motion travels more along latitudes, hence the uncertainty in latitudes increases due to system noise(see figure 5.10) while the curvature is lower (see figure 5.11). Still, the difference between both systems decreases in the last two sequences of motion to about $10°$.

In general, a similar behaviour can be recognised for the other two fingers in both systems with one exception: The information on longitudes increases very slightly in the last phase for index and middle finger of system *a* although not a significant increase, this corresponds to visible motion across longitudes in figure 5.6.

For one instant in time, at $t = 89.632\text{s}$, the estimated position of contact and the associated surface normals are depicted in figure 5.12 as contact frame with the normal drawn in blue as one coordinate axis and two tangential vectors as remaining axes.

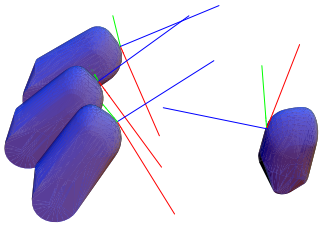

Figure 5.12: Estimate of contact location and surface normal

Concluding this section, the experiment proved the applicability of the approach presented in this thesis: When multiple fingers are grasping and moving an object, velocity measurements subject to kinematic constraints may be used to estimate the point of contact between the fingers and an object. This is also true in the presence of a significant amount of measurement noise in both the position and velocity of the finger tip as presented here. It has also been shown, that this approach will work reliable with the smallest possible number of three fingers in contact. A comparison has been made for two different groupings of three fingers out of four.

5.3 Detection of the Position of Objects

In the previous section, the points of contact between the fingers and the object together with the surface normals at that point have been estimated. These values are given as location and direction on the surface of the *finger*. In this section, continuing the experiment from above, a demonstration of the algorithms proposed in chapter 4 is presented: From the estimated points of contact at the finger tips, the points of contact on the *mocca maker* and the position of the mocca maker relative to the hand reference system are estimated. At first, a geometric model of the mocca maker from figure 5.2 is obtained using the DLR range scanner [Sup02]. The process of obtaining a geometrical model of the surface of the mocca maker has been described in section 2.2.3. Using these algorithms, a triangulated model is obtained as depicted in figure 5.13. In order to reduce the effort of estimation, those parts which cannot be contacted by the finger tips can be cut out of the object description. Also, the mocca maker is obviously symmetric with respect to its longitudinal axis. The fingers are unable to feel any difference, when the mocca maker is rotated around this axis. Hence, an estimation of the object position would result in several equally likely hypotheses. In terms of the usage

of object position in other algorithms, this poses no problem as all positions are also indistinguishable for them. However, in order to reduce computational effort these ambiguous hypotheses do not have to be considered further. Without loss of generality, one side of the mocca maker can be chosen as contact region for the thumb. Now, again those regions unreachable for index middle and ring-finger can be pruned (see figure 5.14). Finally, the accuracy of the model can be adjusted to the accuracy of measurements. As the point of contact at the finger tip can only be estimated with a precision of about $2\mathrm{mm}$ due to noisy measurements, also the object model is required to have only a precision of this magnitude. Here, a large advantage of the presented algorithm becomes clear: The surface description does not have to be continuous. The algorithm works on individual facets rather than on continuous surfaces. This can be used for model reduction: In order to keep that information which remains in the model accurate while nevertheless reducing its spatial density, some facets are removed. Others are left untouched. The model will become perforated this way (see figure 5.15). This method is in contrast to the application of model reduction algorithms, which decrease the number of facets, preserve a continuous surface but consequently reduce the precision of the remaining facets.

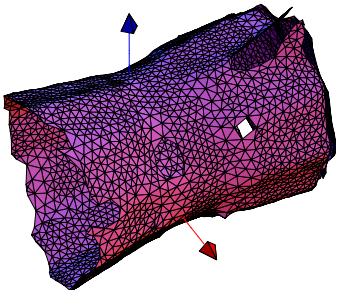

Figure 5.13: Model of a mocca maker

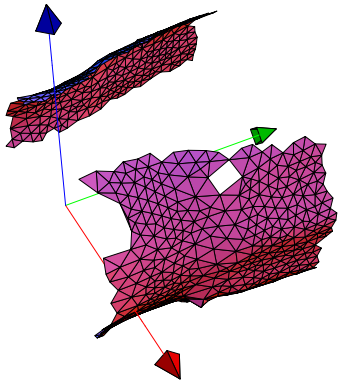

Figure 5.14: Reduced model

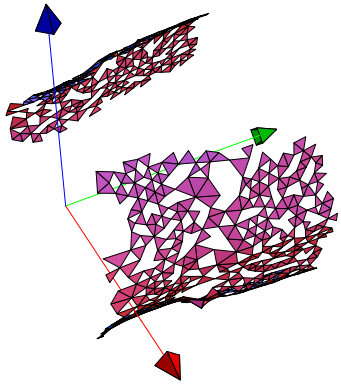

Figure 5.15: Perforated model

For the estimation of object position and *object* contact locations, the *finger* contact points and surface normals obtained in the previous section are used at $t = 89.632\mathrm{s}$ (see figure 5.12). From an a-priori knowledge of how a mocca maker is usually grasped, an initial guess for its location and orientation can be obtained: The origin of the model as depicted in figure 5.13 is most likely located near the weighted centre of the contact points $\vec{x}_o^{(w)} \approx 1/6 \left(3 * \vec{x}_{fc1}^{(w)} + \vec{x}_{fc2}^{(w)} + \vec{x}_{fc3}^{(w)} + \vec{x}_{fc4}^{(w)}\right)$. The weighting balances the importance of the index, middle and ring finger on the one side with that of the thumb on the other side. The orientation of the object can

similarly be guessed as initial value. This initial guess is depicted in 5.18 as red spheres for contact points of thumb, index and middle finger. The contact point of the ring finger is depicted in yellow to illustrate the orientation of the hand.

As seen in the previous section, due to noise on the measurement of finger velocities and finger positions, the estimate of contact position is also subject to uncertainty. This uncertainty allows a relatively accurate determination of the point of contact. The direction of the normal however depends on the point of contact on a sphere of $12.5\mathrm{mm}$ radius and changes noticeably with changing contact points. Hence, the accuracy of the estimated point of contact is higher than the accuracy of the estimated surface normal. During the determination of possible facet hypotheses, when facets are read from the hash table H_2 (see section 4.2.2), according to equation (4.10), the measurement uncertainty can be taken into account. This uncertainty has been set to $\pm 30^\circ$ for the relative angle between two surface normals and to $\pm 1\mathrm{mm}$ for the relative distance between two contact points. During the test of hypotheses, the standard deviation of the lateral distance (see equation (4.15)) has been set to also $1\mathrm{mm}$, the standard deviation of the surface normal (see equation (4.13)) has been set to $0.68\mathrm{mm}$ per component of the vector. The distance d_{fc} along the surface normal in the remaining part χ_2^2 (see equation (4.14)) depends not only on the precise knowledge of the contact position but also on the surface normal. However, in this particular setup, the knowledge of the contact normal is much worse than the precision of the contact position. During the optimisation of χ^2, the compensation of this contribution of surface normals to χ_2^2 leads to an undesired deviation of the translation estimate of object position. As mentioned, this only occurs in situations with a large difference in accuracy between position and normal of contact. To overcome this situation, another term $\chi_4^2 = 1/2 \left(n_{oc,k}^{(o)} \boldsymbol{T}_{(o)}^{(w)} x_{fc,k}^{(w)} + d_{oc,k}^{(o)} \right)^2$ has been introduced. This part penalises the distance of the point of contact on the finger tip from the plane of the facet k. The part χ_2^2 has been weighted little by setting the respective standard deviation to $4\mathrm{mm}$.

The location of the mocca maker during the experiment is depicted in figure 5.16. The estimation of the object position from the contact points and normals as obtained in the previous section is shown in figure 5.17. In this figure, the full model of the mocca maker has been overlayed by the working mesh, depicted as black wire frame. It can be seen, that both, contact points on the object and position of the object are adequately estimated.

For the working model alone, the estimated facets of contact and the corresponding position of the mocca maker relative to the fingers are depicted in figure 5.18. The position of the contact point on the finger is marked with a blue sphere with the respective surface normals attached to it. The contact point of the ring finger is marked by a cyan sphere for better illustration of the hand orientation.

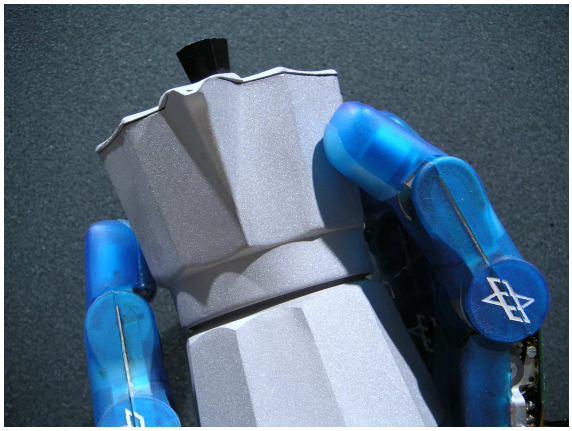

Figure 5.16: Experimental situation

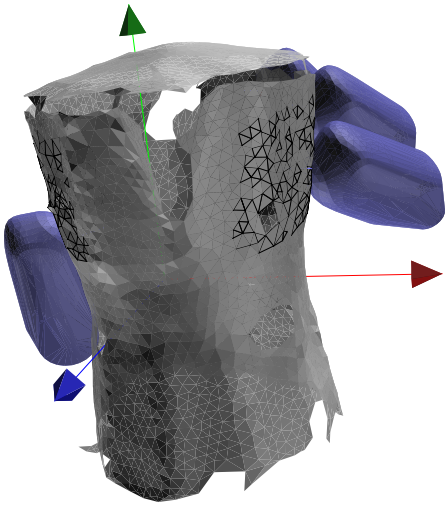

Figure 5.17: Estimated position of a mocca maker

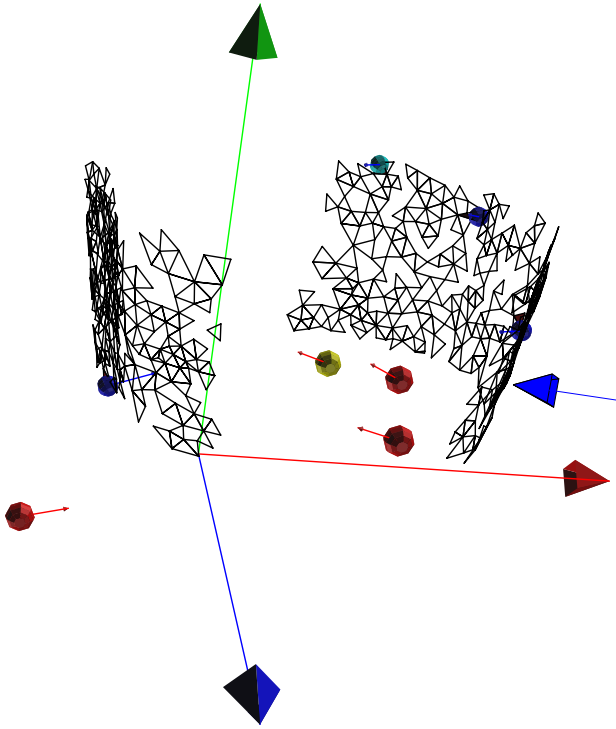

Figure 5.18: Estimated and initial contact locations

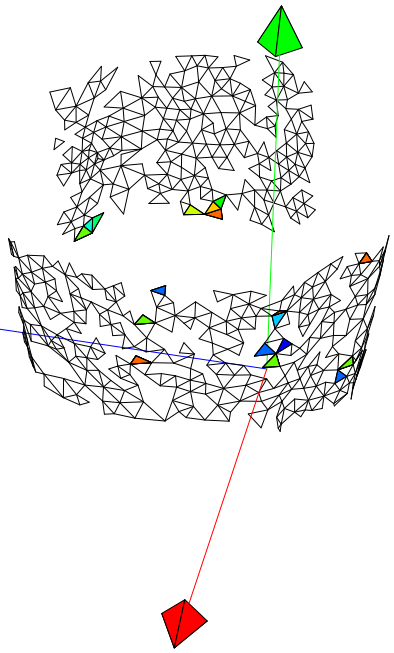

Figure 5.19: Location of best 10 estimated contact points

The spheres totally cover the respective contact facet. It can be seen, that the fit of position is accurate while the surface normals are somewhat misaligned. A proper choice of the standard deviations of the individual parts of χ^2 guarantees a satisfying estimation of object position despite some inaccuracies of measurement.

The robustness of the estimate can also be seen in figure 5.19. The ten best hypotheses of contact facet tuples have been shaded from red to blue, with red being rated as the best of the ten. All hypotheses refer to similar contact locations, some facets are common through nine out of ten hypotheses. This observation confirms the choice of these regions as the most likely regions for each finger.

Concluding this section, it can be stated that the proposed method of estimating the location of contact on the object and the position of the object succeeds in the experiments. The position of the object has been estimated from the point of contact and the surface normal obtained from four fingers grasping a mocca maker. The presented algorithm is suitable for enhancing the sensing capabilities in robotic grasping systems as the DLR Hand II.

Chapter 6

Conclusion

6.1 Results of this Work

This work addresses a problem of robotic applications in realistic, natural environments. In such environments, it is desirable to perform a large variety of different tasks most of which require grasping or manipulation of objects. In order to keep the effort of equipping the robot small, the robot used in these scenarios should only use one single, generic tool. It was argued that the most appropriate generic tools in humanoid environments are robotic hands. It has been explained that in order to properly grasp and manipulate objects with these robotic hands, the location of the contact point between the object and the surfaces of the fingers is required. Besides, before and also during grasping, the location and motion of the object is necessary for proper handling. In previous work, this information has been obtained from vision or tactile sensors. However, tactile sensing is not available in all robot hands and during grasping, situations may occur where vision is not feasible. Nevertheless, usual robotic hands are equipped with force/torque or at least position sensors that can be used as substitute to obtain the same information. In order to tackle the problem of contact point detection without tactile sensing, two different types of algorithms have been developed.

A method for contact detection has been proposed which is based on velocity readings for all fingers: The relative velocity of different pairings of fingers in a multi-fingered grasp are compared. Hereby, constraints on the motion of the object along the surfaces of the respective finger tips occur, e.g. in some cases of contact, the two bodies may only roll on each other but not slide. Knowledge about both, motion constraints and relative finger velocity allows the determination of the position of the contact point along with its evolution over time. Additionally, also the motion of the object over time can be tracked. Two methods have been proposed to obtain this information. The first method is based on a strict geomet-

ric interpretation of a system of equations whereas the other method proposes an information filter, dual to a Kalman filter. Both algorithms involve the minimisation of a merit function, each of which has been numerically examined, using the kinematic description of DLR Hand II as example. Additionally, a kinematic simulation of a moving object with varying levels of measurement disturbance has been performed to point out the tracking abilities of the algorithm introduced here. The examinations have been performed for an observation of three fingers, which is the minimum number required for a secure grasp. The use of only three fingers in the evaluation also ensures the feasibility of the proposal in the case of finger gaiting and regrasping. As the quality of the estimate increases with the number of fingers included, this examination can be considered a worst case scenario.

A second section presents a generalised method to evaluate force and torque information in the tip and in the body of the individual fingers, e.g. joint torques, to determine the contact position between an object and the respective finger. This method produces the point of contact as parameter values of a parameterised description of the finger surface. Also, the contact forces and torques transmitted at the point of contact are returned. This approach is valid for all common models of contact. The method has been formulated as an optimisation problem. Results of numerical examinations and simulations have been reported using a description of the DLR Hand II as example environment. The DLR Hand II is equipped with three joint torque sensors and a six dimensional force/torque sensor. The surface of the tip has been modeled as a sphere. It was shown that in this simulation example, the longitude and latitude of the contact on the finger tip and the transmitted forces and torques could be identified. The quality and robustness of the merit function has been examined. With moderate disturbances, very accurate localisation of the contact point could be achieved.

Both of the above methods estimate the point of contact on a geometrically known finger tip in different ways. The kinematical method presented first requires a motion of the objects which the individual fingers follow. It can be used when several fingers are in contact with an object and requires only position or velocity sensors which are present in any robot hand for position control. It is particularly feasible for the tracking of the motion of the contact points on the finger tips. The second method, called intrinsic, also uses force/torque sensors demanding more sensory equipment, but can also be used for individual fingers and when no motion of the object is desired.

Having obtained the point of contact for example by either of the above methods, the position of the object in the workspace as well as the contact positions of the fingers on the object can be determined. This thesis presents a method to obtain both from the point of contact and the surface normal at this point of contact. In order to define the position of an object, a geometrical description of the surface of the object is required. Here, a polygonal description has been identified

as the most suitable object model. A pre-processing of the object model has been suggested: Relative measures between individual polygons of the surface description can be computed and stored in an extended object model. This work presents a quick method to search this extended model for feasible hypotheses of contact locations of the finger tips on the object. The rapid handling of this search is essential, as a complete search would be of combinatorial complexity and the number of polygons in a realistic object model is high. The hypotheses are tested for their match with the measurements minimising a merit function. Statistical interpretation of the algorithm in the sense of a maximum likelihood estimate is given. The algorithm is examined with respect to the properties of the merit function using several object models and a statistical evaluation of the position estimation has been presented.

Contact point detection and object position estimation have both been implemented for and tested using the DLR Hand II in a continuous experiment: Using the kinematic algorithm, points of contact of a mocca maker at the finger tips have been estimated. From these, the position of the mocca maker in the hand was reconstructed. The suitability for real-world applications has been proven.

6.2 Perspective

This work made no particular assumptions on how a robotic hand grasps an object, and hence did not make any restrictions about a particular type of contact or grasp. Nevertheless, for the simplicity and clearness of presentation, for the numerical examinations and experiments described in this thesis, a mathematical description of precision grasps with soft finger contact have been applied. As this is not an actual restriction to the algorithms presented here, further research should explicitly concentrate on other types of contact and grasp such as pinch grasps and evaluate the behaviour of the given proposals. It may even be possible to extend both approaches of contact point detection to multi contact grasps, when an appropriate contact model is guaranteed. For the detection by kinematic constraints this contact model may include sliding for some fingers. This examination will extend the impact of the proposed algorithms to both fine and precise handling of objects, as well as strong and secure fixing of tools.

The kinematic approach to determine the position of contact relies on the measurement of the redundant motion of several fingers and can hence, to some extend, handle also heavy noise or even systematic measurement errors as miscalibration. The intrinsic algorithm comes to its limit when force/torque sensor readings are heavily disturbed as its redundancy depends on the number of sensors actually implemented in a finger but generally is low. However, the latter approach is also applicable for individual finger contacts. When combining both

kinematic and intrinsic, approaches a more robust algorithm would arise, which allows both tracking contact points while manipulating an object in the hand and also while statically grasping the object or initiating a grasp with not all fingers yet in contact.

Reversing the flow of information, the ideas which are the basis of both algorithms can also be used to calibrate the respective sensors. Instead of obtaining the location of contact and the object position, a sample object can be grasped by the hand. The location of which can be obtained by other means as e.g. a special position tracking system [Art03]. With these measurements and the raw values from position and force/torque sensors, these sensors can be calibrated.

Regarding the detection of object position, a lot of work has already been undergone to detect the position of an object in the shortest possible time. Nevertheless the algorithms can further be accelerated when a multi-resolution object model is applied. Instead of searching all the object description for hypotheses of contact positions in a high resolution, a coarse model could be searched for the general regions of contact first. Only these regions have subsequently to be examined at a high resolution for accuracy.

All presented work on small details will strengthen the robustness of a robotic hand. By joining the work presented here with other results of research published in literature, e.g. the proper choice of grasps on generic objects [BFH03b], the optimisation of force exerted on the contact points [Sch01], the path to a "black box" grasping system can be struck. This black box grasping system consists of a robotic hand and a library of abilities which can be selected and executed to perform more complex tasks without dealing with low level grasp activities. The grasping system will in turn provide information about the environment it collected during operation. In a more general scenario, perception by touch will not be enough. In order to grasp an object, it has to be located by other means as e.g. vision. Then coordinated movement of arm and hand in closed loop with vision based perception is required. An approach of biologically inspired hand/eye coordination during grasping with a parallel jaw gripper was proposed in [HPS+00]. Vision for grasping was examined in [RSL+02] and an initial setup of a larger grasp system combining vision and grasping was presented in [HBBH04]. A black box grasping system would reduce the effort and increase the robustness of such a coordinated eye / arm / hand system by far leaving room for delicate manipulation and handling activities. As the survey of this thesis showed, simple easy-to-use hands are already available. A more sophisticated system should follow now which takes advantage of the achievements of most recent results of research on grasping and robotic hand developments.

The idea of an autonomous robot assistant motivated this thesis. The work presented here contributed its part but the vision continues to persist. With a highly sophisticated grasping system fusion with the results of other projects of

humanoid and service robotics is the natural consequence and will lead to robots which are able to obtain orders, autonomously deduct the necessary steps to perform the task, can simultaneously navigate in and learn about its surroundings, discover and locate known and unknown objects and finally handle these. Research can and will show and prepare the path to a robotic assistant and maybe companion in the very near future. Society will decide how far the development may walk along this path to increasingly humanoid robots and how much autonomy may be granted to them. As for all new developments in science, there have always been advocates and, sometimes also for a good reason, adversaries. It is the natural duty of research to show the possibilities and advantages of a development, but also consider the drawbacks and risks. So let's continue this research while keeping Aesop in mind : *Si quid agis, prudenter agas et respice finem*.

Bibliography

[ACF02] David L. Akin, Craig R. Carrigan, and Anthony W. Foster. Development of a Four-Fingered Dexterous Robot End Effector For Space Operations. In *Proc. of IEEE Conf. on Robotics and Automation*, pages 2302 – 2308, Washington, DC, USA, May 2002.

[AMD02] Pierre Alliez, Mark Meyer, and Mathieu Desbrun. Interactive geometric remeshing. In *SIGGRAPH 2002 Conference Proceedings*, 2002.

[AMOL97] Peter K. Allen, Andrew T. Miller, Paul Y. Oh, and Brian S. Leibowitz. Using tactile and visual sensing with a robotic hand. In *Proc. of the IEEE Intl. Conf. on Robotics and Automation, Albuquerque, New Mexico*, April 1997.

[AMOL99] Peter K. Allen, Andrew T. Miller, Paul Y. Oh, and Brian S. Leibowitz. Integration of vision, force and tactile sensing for grasping. *International Journal of Intelligent Mechatronics*, 4(1):129–149, January 1999.

[Art03] Art-tracking system GmbH. http://www.ar-tracking.de/, 2003.

[Bar03a] Details of the Barrett Hand. http://www.barretttechnology.com/ /robot/index.htm, 2003.

[Bar03b] Image of the Barrett Hand. http://www.barretttechnology.com/ /robot/products/hand/empty.jpg, 2003.

[Bau75] Bruce G. Baumgart. Winged-edge polyhedron representation for computer vision. Technical report, Stanford University, National Computer Conference, Stanford, California, May 1975.

[BBEC01] F. Blais, J.-A. Beraldin, S. El-Hakim, and L. Cournoyer. Comparison of pose estimation methods for a 3D laser tracking system using triangulation and programmetry techniques. In *Proceedings of the SPIE Electronic Imaging, San Jose, USA*, January 2001.

[Ben03] Ömer S. Benli. The branch-and-bound approach. International Journal of Industrial Engineering, http://www.csulb.edu/~obenli/Research/IE-encyc/bb.html, 2003.

[BFH99] Christoph Borst, Max Fischer, and Gerd Hirzinger. A fast and robust grasp planner for arbitrary 3D objects. In *Proc. of the IEEE Intl. Conf. on Robotics and Automation, Detroit, Michigan*, pages 1890–1896, May 1999.

[BFH+03a] Christoph Borst, Max Fischer, Steffen Haidacher, Hong Liu, and Gerd Hirzinger. DLR Hand II: Experiments and experiences with an anthropomorphic hand. In *Proc. of the IEEE Intl. Conf. on Robotics and Automation, Taipei, Taiwan*, September 2003.

[BFH03b] Christoph Borst, Max Fischer, and Gerd Hirzinger. Grasping the Dice by Dicing the Grasp. In *Proceedings of the IEEE/RSJ Int. Conference on Intelligent Robots and Systems*, pages 3692 – 3697, Las Vegas, Nevada, USA, October 2003.

[BFV91] Claudio Bonivento, Eugenio Faldella, and Gabriele Vassura. The University of Bologna Robotic Hand Project: Current State and Future Developments. In *Intl. Conf. on Advanced Robotics ICAR*, volume 1, pages 349 – 356, Pisa, Italy, June 1991.

[BGLH01] J. Butterfaß, M. Grebenstein, H. Liu, and G. Hirzinger. DLR-Hand II: Next Generation of Dextrous Robot Hand. In *Proc. IEEE Conf. on Robotics and Automation*, pages 109 – 114, Seoul, Korea, May 2001.

[BHKL98] J. Butterfaß, G. Hirzinger, S. Knoch, and H. Liu. DLR's Multisensory Articulated Hand. part I: Hard- and software architecture. In *Proc. IEEE Conf. on Robotics and Automation*, pages 2081 – 2086, Leuven, 1998.

[Bic90] Antonio Bicchi. Intrinsic contact sensing for soft fingers. In *Proc. of the IEEE Intl. Conf. on Robotics and Automation, Cincinati, Ohio*, pages 968 – 973, 1990.

[Bic93] Antonio Bicchi. Force distribution in multiple whole-limb manipulation. In *Proc. of the IEEE Intl. Conf. on Robotics and Automation, Atlanta, Georgia*, May 1993.

[Bic94] Antonio Bicchi. On the problem of decomposing grasp and manipulation forces in multiple whole-limb manipulation. *Intl. Journal of Robotics and Autonomous Systems*, 13, 1994. Elsevier Science.

[Bic95] Antonio Bicchi. On the closure properties of robotic grasping. *The Int. Journal of Robotics Research*, 14(4), 1995.

[BK00] Antonio Bicchi and Vijay Kumar. Robotic grasping and contact: A review. In *Proc. of the IEEE Intl. Conf. on Robotics and Automation, San Francisco, California*, pages 348 – 353, April 2000.

[BM02] Luigi Biagiotti and Claudio Melchiorri. Design aspects for advanced robot hands: Sensory system. In *Tutorial T1, Proc. of the IEEE/RSJ Intl. Conf. on Intelligent Robots and Systems, Lausanne, Swiss*, September 2002.

[BMG00] Francois Berry, Phillipe Martinet, and Jean Gallice. Real time visual servoing around a complex object. *IEICE Transactions on Informations and Systems*, E83-D(7):1358 – 1368, July 2000.

[BMP99] Antonio Bicchi, Alessia Marigo, and Domenico Prattichizzo. Dexterity through rolling: Manipulation of unknown objects. In *Proc. of the IEEE Intl. Conf. on Robotics and Automation, Detroit, Michigan*, pages 1583 – 1588, May 1999.

[Bro90] R. W. Brocket. Some mathematical aspects of robotics. In *Proceedings of Symposia in Applied Mathematics*, volume 41, Providence, RI, 1990. American Mathematical Society.

[BS97] Martin Buss and Thomas Schlegl. Multi-fingered regrasping using on-line grasping force optimization. In *Proc. of the IEEE Intl. Conf. on Robotics and Automation, Albuquerque, New Mexico*, pages 998 – 1003, April 1997.

[BS99] C. Breazeal and B. Scassellati. A context-dependent attention system for a social robot. In *International Joint Conference on Artificial Intelligence (IJCAI99), Stockholm, Sweden*, pages 1146–1151, 1999.

[BSB93] Antonio Bicchi, J. Kenneth Salisbury, and David L. Brock. Contact sensing from force measurements. *Intl. Journal of Robotics Research*, 12(3), 1993.

[BTZ90] George A. Bekey, Rajko Tomovic, and Ilija Zeljkovic. *Control Architecture for the Belgrade/USC*, chapter 7. Springer Verlag, 1990.

[Bur72] Rainer E. Burkard. *Methoden der Ganzzahligen Optimierung*. Springer Verlag, Wien, 1972.

[But99] Jörg Butterfaß. *Eine hochintegrierte multisensorielle Vier-Finger-Hand für Anwendungen in der Servicerobotik*. PhD thesis, Fachbereich für Elektrotechnik und Informationstechnik der Technischen Universität Darmstadt, 1999.

[CC98] Andrea Caffaz and Giorgio Cannata. The Design and Development of the DIST-Hand Dextrous Gripper. In *Proc. IEEE Int. Conf. on Robotics and Automation*, pages 2075 – 2080, Leuven, Belgium, May 1998.

[CGP96] M. Charlebois, K. Gupta, and S. Payandeh. Curvature based shape estimation using tactile sensing. In *Proc. of the IEEE Intl. Conf. on Robotics and Automation, Minneapolis, Minnesota*, pages 3502 – 3507, April 1996.

[CGP99] M. Charlebois, K. Gupta, and S. Payandeh. Shape description of curved sufaces from contact sensing using surface normals. *Intl. Journal of Robotics Research*, 18(8):779–787, August 1999.

[CJL98] K. K. Choi, S. L. Jiang, and Z. Li. Multifingered robotic hands: Contact experiments using tactile sensors. In *Proc. of the IEEE Intl. Conf. on Robotics and Automation, Leuven, Belgium*, May 1998.

[CMM+01] M. C. Carrozza, B. Massa, S. Micera, M. Zecca, and P. Dario. A "Wearable" Artificial Hand for Prosthetics and Humanoid Robotics Applications. In *Proc. IEEE-RAS International Conference on Humanoid Robots HUMANOIDS 2001*, Waseda University International Conference Center, Tokyo, Japan, November 2001.

[CMZ95] Stefano Caselli, Corrado Magnanini, and Francesco Zanichelli. On the robustness of haptic object recognition based on polyhedral shape representations. In *Proc. of the IEEE/RSJ Intl. Conf. on Intelligent Robots and Systems*, 1995.

[CMZC96] Stefano Caselli, Corrado Magnanini, Francesco Zanichelli, and Enrico Caraffi. Efficient exploration and recognition of convex objects based on haptic perception. In *Proc. of the IEEE Intl. Conf. on Robotics and Automation, Minneapolis, Minnesota*, April 1996.

[CRZ96] Ning Chen, Ray Rink, and Hong Zhang. Local object shape from tactile sensing. In *Proc. of the IEEE Intl. Conf. on Robotics and Automation, Minneapolis, Minnesota*, pages 3496 – 3501, April 1996.

[Cut89] Mark R. Cutkosky. On Grasp Choice, Grasp Models, and the Design of Hands for Manufacturing Tasks. *IEEE Transactions on Robotics and Automation*, 5(3):269 – 279, June 1989.

[Cyb03] Details of the immersion cyberglove. http://www.immersion.com/ /3d/products/cyber_glove.php, 2003.

[DA99] Zoe Doulgeri and Suguru Arimoto. A force commanded impedance control for a robotic finger with uncertain kinematics. *Intl. Journal of Robotics Research*, 18(10):1013 – 1029, October 1999.

[DBDD97] S. Dutré, H Bruyninckx, S. Dmey, and J. De Schutter. Solving redundant contact and grasp uncertainties. In *Proc. of the IEEE/RSJ Intl. Conf. on Intelligent Robots and Systems, Grenoble, France*, 1997.

[DDH00] Thomas Debus, Pierre Dupont, and Robert Howe. Automatic identification of local geometric properties during teleoperation. In *Proc. of the IEEE Intl. Conf. on Robotics and Automation, San Francisco, California*, April 2000.

[Dio03] Alexander Dionisius. Ins Leere gegriffen. *Süddeutsche Zeitung*, May 27th, 2003.

[DSMH99] Pierre E. Dupont, Capt Timothy M. Schulteis, Paul A. Millman, and Robert D. Howe. Automatic identification of environment haptic properties. *Presence: Teleoperators and Virtual Environments*, 8(4):392–409, August 1999.

[Erd98] Michael Erdmann. Shape recovery from passive locally dense tactile data. In *Workshop on the Algorithmic Foundation of Robotics*, 1998.

[FBH+01] Udo Frese, Berthold Bäuml, Steffen Haidacher, Günter Schreiber, Ingo Schäfer, Matthias Hähnle, and Gerd Hirzinger. Off-the-shelf vision for a robotic ball catcher. In *Proc. of the IEEE/RSJ Intl. Conf. on Intelligent Robots and Systems, Maui, Hawaii, USA*, Oktober 2001.

[Fea90a] R. S. Fearing. Tactile sensing mechanisms. *Intl. Journal of Robotics Research*, 9(3):3–23, June 1990.

[Fea90b] Ronald S. Fearing. Tactile sensing for shape interpretation. In S. Venkataraman and T. Iberall, editors, *Dextrous Robot Manipulation*, chapter 10. Springer-Verlag, 1990.

[FH86] O. D. Faugeras and M. Hebert. The representation, recognition, and locating of 3-D objects. *Intl. Journal of Robotics Research*, 5(3):27–52, 1986.

[Flu03] Image of the Karlsruhe Fluid Hand. http://www.sfb588.uni-karlsruhe.de/BilddateienSFB/greifhand-r3.gif, 2003.

[FTAD00] Naoki Fukaya, Shigeki Toyama, Tamim Asfour, and Rüdiger Dillmann. Design of the TUAT/Karlsruhe Humanoid Hand. In *Proc. IEEE/RSJ Intl. Conf. on Intelligent Robots and Systems*, volume 3, pages 1754 – 1759, Takamatsu, Japan, October 2000.

[FW98] Th. Fischer and H. Wörn. Structure of a robot system: Karlsruhe Dextrous Hand II. In *Proc. of Mediteranean Conf. on Control and Systems*, 1998.

[GBSD96] Jan De Geeter, H. Van Brussel, J. De Schutter, and M. Decréton. Recognizing and locating objects with local sensors. In *Proc. of the IEEE Intl. Conf. on Robotics and Automation, Minneapolis, Minnesota*, April 1996.

[GH93] Roderic A. Grupen and Manfred Huber. 2-D contact detection and localization using proprioceptive information. In *Proc. of the IEEE Intl. Conf. on Robotics and Automation, Atlanta, Georgia*, May 1993.

[GHP+97] Perry Gray, William Hart, Laura Painton, Cindy Phillips, Mike Trahan, and John Wagner. A survey of global optimization methods. http://www.cs.sandia.gov/opt/survey/main.html, Sandia national Laboratories, 1997.

[GL84] W. Eric L. Grimson and Tomás Lozano-Pérez. Model-based recognition and localization from sparse range or tactile data. *Intl. Journal of Robotics Research*, 3(3):3–35, 1984.

[GZAL01] J. P. Gazeau, S. Zeghloul, M. Arsicault, and J. P. Lallemand. The LMS hand: force and position controls in the aim of the fine manipulation of objects. In *Proc. of the IEEE Intl. Conf. on Robotics and Automation, Seoul, Korea*, pages 2642–2648, May 2001.

[Hai98] Steffen Haidacher. Stabilitätsuntersuchung hybrider (diskret-kontinuierlicher) Umgreifregler für mehrfingrige Roboterhände. Master's thesis, Fakultät für Elektro- und Informationstechnik, TU München, 1998.

[HBBH04] Ulrich Hillenbrand, Bernhard Brunner, Christoph Borst, and Gerd Hirzinger. Towards Service Robotics for the Human Enviroment: the Robutler. In *Proc. of the International Symposium on Robotics*, Paris, France, March 2004. to appear.

[HBF+03] Steffen Haidacher, Jörg Butterfaß, Max Fischer, Markus Grebenstein, Klaus Jöhl, Klaus Kunze, Matthias Nickl, Nikolaus Seitz, and Gerd Hirzinger. DLR Hand II: Hard- and software architecture for information processing. In *Proc. of the IEEE Intl. Conf. on Robotics and Automation, Taipei, Taiwan*, September 2003.

[HK93] W. Stamps Howard and Vijay Kumar. A minimum principle for the dynamic analysis of systems with frictional contacts. In *Proc. of the IEEE Intl. Conf. on Robotics and Automation, Atlanta, Georgia*, May 1993.

[HK95] W. Stamps Howard and Vijay Kumar. Modeling and analysis of the compliance and stability of enveloping grasps. In *Proc. of the IEEE Intl. Conf. on Robotics and Automation, Nagoya, Japan*, May 1995.

[Hon03] Details of the Honda P3 humanoid robot. http://www.honda-robots.com, 2003.

[HPS+00] Alexa Hauck, Georg Passig, Thomas Schenk, Micheal Sorg, and Georg Färber. On the performance of a biologically motivated visual control strategy for robotic hand-eye coordination. In *Proc. of the IEEE/RSJ Intl. Conf. on Intelligent Robots and Systems, Takamatsu, Japan*, Oktober 2000.

[HSA+02] Gerd Hirzinger, Norbert Sporer, Alin Albu-Schäffer, Matthias Hähnle, Rainer Krenn, et al. DLR's torque-controlled Light Weight robot III - are we reaching the technological limits now? In *Proc. of the IEEE Intl. Conf. on Robotics and Automation, Washington, DC, USA*, May 2002.

[HSB99] Steffen Haidacher, Thomas Schlegl, and Martin Buss. Grasp evaluation based on unilateral force closure. In *Proc. of the IEEE/RSJ Intl. Conf. on Intelligent Robots and Systems, Kyongju, Korea*, pages 424 –429, Oktober 1999.

[HTL99] Li Han, Jeffrey C. Trinkle, and Zexiang Li. Grasp analysis as linear matrix inequality problems. In *Proc. of the IEEE Intl. Conf. on Robotics and Automation, Detroit, Michigan*, pages 1261 – 1268, May 1999.

[JCX01] Guowu Jia, Gunag Chen, and Ming Xie. Design of a Novel Compact Dexterous Hand for Teleoperation. In *Proc. IEEE Intl. Symposium on Computational Intelligence in Robotics and Automation*, pages 5–10, Banff, Alberta, Canada, July 29 - August 1 2001.

[JE98] Yan Bin Jia and Michael Erdmann. Observing pose and motion through contact. In *Proc. of the IEEE Intl. Conf. on Robotics and Automation, Leuven, Belgium*, May 1998.

[JE99] Yan Bin Jia and Michael Erdmann. Pose and motion from contact. *Intl. Journal of Robotics Research*, 18(5):466 – 490, May 1999.

[JH98] Andrew E. Johnson and Martial Hebert. Surface matching for object recognition in complex 3-D scenes. *Image and Vision Computing*, 1998.

[JL00] Matjaz Jogan and Ales Leonardis. Robust localization using panoramic view-based recognition. In *Proceedings of the 15th International Conference on Pattern Recognition, Barcelona, Spain*, 2000.

[JWKB84] S.C. Jacobsen, J. E. Wood, D. F. Knutti, and K. B. Biggers. The UTAH/M.I.T. Dextrous Hand: Work in Progress. *Int. Journal of Robotics Research*, 3(4):21 – 50, Winter 1984.

[JWR97] Jan Jokusch, Jörg Walter, and Helge Ritter. A tactile sensor system for a three-fingered robot manipulator. In *Proc. of the IEEE Intl. Conf. on Robotics and Automation, Albuquerque, New Mexico*, April 1997.

[KL90] R. L. Klatzky and S. Lederman. Intelligent exploration by the human hand. In S. Venkataraman and T. Iberall, editors, *Dextrous Robot Manipulation*, chapter 4. Springer-Verlag, 1990.

[KLC+01] Peter J. Kyberd, Colin Light, Paul H. Chappell, Jim M. Nightingale, Dave Whatley, and Mervyn Evans. The design of anthropomorphic prosthetic hands: A study of the Southampton Hand. *Robotica*, 19:593 – 600, 2001.

[KMT92] Makoto Kaneko, Hitishi Maekawa, and Kazuo Tanie. Active tactile sensing by robotic fingers based on minimum-external-sensor-realization. In *Proc. of the IEEE Intl. Conf. on Robotics and Automation, Nice, France*, pages 1289–1294, May 1992.

[Kre91] Ulrich Krengel. *Einführung in die Wahrscheinlichkeitstheorie und Statistik*. Vieweg Studium, Braunschweig, 3 edition, 1991.

[KSS01] Haruhisa Kawasaki, Hisayuki Shimomura, and Yuuji Shimizu. Educational-industrial complex development of an athropomorphic robot hand 'Gifu Hand'. *Advanced Robotics*, 15(3):357 – 363, June 2001.

[KT90] Makoto Kaneko and K. Tanie. Contact point detection for grasping of an unknown object using self-posture changeability (spc). In *Proc. of the IEEE Intl. Conf. on Robotics and Automation, Cincinati, Ohio*, May 1990.

[LB96] Ales Leonardis and Horst Bischof. Dealing with occlusions in the Eigenspace approach. In *Proceedings of the IEEE Conference on Computer Vision and Pattern Recognition, San Francisco, USA*, 1996.

[LD99] C. S. Lovchik and M. A. Diftler. The Robonaut Hand: A dextrous robot hand for space. In *Proc. IEEE Conf. on Robotics and Automation*, pages 907 – 912, Detroit, Michigan, USA, May 1999.

[LGP02] Klaus Löffler, M. Gienger, and Friedrich Pfeiffer. Concept of jogging Johnnie. In *Proc. of the IEEE Intl. Conf. on Robotics and Automation, Washington, DC, USA*, May 2002.

[LH99] Hong Liu and Gerd Hirzinger. Cartesian impedance control for the DLR Hand. In *Proc. of the IEEE/RSJ Intl. Conf. on Intelligent Robots and Systems, Kyongju, Korea*, pages 106 – 112, Oktober 1999.

[Liu03] Hong Liu. The HIT/DLR Dexterous Hand: Work in progress. In *Proc. of the IEEE Intl. Conf. on Robotics and Automation, Taipei, Taiwan*, September 2003.

[LMBH98] H. Liu, P. Meusel, J. Butterfaß, and G. Hirzinger. DLR's Multisensory Articulated Hand. part II: The parallel torque/position control system. In *Proc. IEEE Conf. on Robotics and Automation*, pages 2087 – 2093, Leuven, 1998.

[LMH95] Hong Liu, Peter Meusel, and Gerd Hirzinger. A tactile sensing system for the DLR three-finger robot hand. In *Proceedings of the International Conference on Measurement and Control in Robotics, Swolenice Castle, Slovakia*, 1995.

[LN99] M. H. Lee and H. R. Nicholls. Tactile sensing for mechatronics - a state of the art survey. *Mechatronics*, 9:1–31, 1999.

[LV02] F. Lotti and G. Vassura. Design aspects for advanced robot hands: Mechanical design. In *Tutorial T1, Proc. of the IEEE/RSJ Intl. Conf. on Intelligent Robots and Systems, Lausanne, Swiss*, September 2002.

[LW98] Yun Hui Liu and Mei Wang. Qualitative test and force optimization of 3D frictional force-closure grasps using linear programming. In *Proc. of the IEEE Intl. Conf. on Robotics and Automation, Leuven, Belgium*, pages 3335 – 3340, May 1998.

[Mag02] Marcus A. Magnor. Geometry-based automatic object localization and 3-D pose detection. In *Proceedings of the IEEE Southwest Symposium on Image Analysis and Interpretation, Santa Fe, USA*, April 2002.

[Mal02] Ezio Malis. Survey of vision-based robot control. European Naval Ship Design, Short Course, Brest, France, Ensieta, April 2002.

[MF93] Nobuharu Mimura and Yasuyuki Funahashi. Parameter identification in the grasp of an inner link mechanism. In *Proc. of the IEEE Intl. Conf. on Robotics and Automation, Atlanta, Georgia*, May 1993.

[MJ90] Ian D. McCammon and Steve C. Jacobsen. Tactile sensing and control for the Utah/MIT Hand. In S. Venkataraman and T. Iberall, editors, *Dextrous Robot Manipulation*, chapter 11. Springer-Verlag, 1990.

[MK92] Raju S. Mattikalli and Pradeep K. Khosla. Motion constraints from contact geometry: Representation and analysis. In *Proc. of the IEEE Intl. Conf. on Robotics and Automation, Nice, France*, May 1992.

[MLS94] Richard M. Murray, Zexiang Li, and S. Shankar Sastry. *A Mathematical Introduction to Robotic Manipulation*. CRC Press, Boca Raton, Fl, 1994.

[Mon88] David J. Montana. The Kinematics of Contact and Grasp. *The International Journal of Robotics Research*, 7(3):17 – 32, June 1988.

[Mon95] David J. Montana. The kinematics of multi-fingered manipulation. *IEEE Transactions on Robotics and Automation*, 11(4):491 – 503, August 1995.

[MS86] Matthew T. Mason and J. Kenneth Salisbury. *Robot Hands and the Mechanics of Manipulation*. The MIT Press, Cambridge, MA, 2 edition, 1986.

[MS93] Shin-Yo Muto and Ken-Ichiro Shimokura. Accurate contact point detecting using force and velocity information complementary. In *Proc. of the IEEE Intl. Conf. on Robotics and Automation, Atlanta, Georgia*, pages 738 – 744, May 1993.

[MSS87] B. Mishra, Jacob T. Schwartz, and Micha Sharir. On the existence and synthesis of multifinger positive grips. *Algorithmica*, 2, 1987.

[MTK95] H. Maekawa, K. Tanie, and K. Komoriya. Tactile sensor based manipulation of an unknown object by a multifingered hand with rolling contact. In *Proc. of the IEEE Intl. Conf. on Robotics and Automation, Nagoya, Japan*, pages 743 – 750, May 1995.

[Mur02] Robin Murphy. Human-robot interaction in robot-assisted urban search and rescue. In *Workshop W1, Proc. of the IEEE Intl. Conf. on Robotics and Automation, Washington, DC, USA*, May 2002.

[NAS03] Image of the NASA Robonaut Hand. http://quest.arc.nasa.gov / /people/journals/space/keith /robohand2.gif, 2003.

[NL89] Howard R. Nicholls and Mark H. Lee. A survey of robot tactile sensing technology. *Intl. Journal of Robotics Research*, 8(3):3–30, June 1989.

[OC99] Allison M. Okamura and Mark R. Cutkosky. Haptic exploration of fine surface features. In *Proc. of the IEEE Intl. Conf. on Robotics and Automation, Detroit, Michigan*, May 1999.

[OCT+00] Allison M. Okamura, Michael A. Costa, Michael L. Turner, Christopher Richard, and Mark R. Cutkosky. *Experimental Robotics VI*, volume 250 of *Lecture Notes in Control and Information Science*, chapter Haptic Surface Exploration, pages 423–432. Springer Verlag, 2000.

[Oka90] Tokuji Okada. A new tactile sensor design based on suspension-shells. In S. Venkataraman and T. Iberall, editors, *Dextrous Robot Manipulation*, chapter 12. Springer-Verlag, 1990.

[OM00] Agata Opalach and Steve Maddock. An overview of implicit surfaces. The University of Sheffield, UK, 2000. Department of Computer Science.

[OSC00] Allison M. Okamura, Niels Smaby, and Mark R. Cutkosky. An overview of dexterous manipulation. In *Proc. of the IEEE Intl. Conf. on Robotics and Automation, San Francisco, California*, pages 255 – 262, April 2000.

[OTC97] Allison M. Okamura, M. L. Turner, and Mark R. Cutkosky. Haptic exploration of objects with rolling and sliding. In *Proc. of the IEEE Intl. Conf. on Robotics and Automation, Albuquerque, New Mexico*, April 1997.

[Ott03a] Details of the prosthesis by Otto Bock. http://www.ottobock.de/, 2003.

[Ott03b] Otto Bock Austria Ges.m.b.H., Kaiserstraße 39, A-1070 Wien, Austria. *Patienteninformation für Otto Bock^{tm} System Elektrohände*, 01.03/14 - internet edition, 2003.

[Pap96] Markos Papageorgiou. *Optimierung*. R. Oldenbourg Verlag, München, 2 edition, 1996.

[PJT+02] L. Petersson, P. Jensfelt, D. Tell, M. Strandberg, D. Kragic, and H. I. Christensen. Systems integration for real-world manipulation tasks. In *Proc. of the IEEE Intl. Conf. on Robotics and Automation, Washington, DC, USA*, May 2002.

[PTVF92] William H. Press, Saul A. Teukolsky, William T. Vetterling, and Brian P. Flannery. *Numerical Recipes in C*. Cambridge University Press, Cambridge, 2 edition, 1992.

[RB95a] E. Rimon and J. Burdick. A configuration space analysis of bodies in contact–part I: 1st order mobility. *Mechanism and Machine Theory*, 30(6), 1995.

[RB95b] E. Rimon and J. Burdick. A configuration space analysis of bodies in contact–part II: 2nd order mobility. *Mechanism and Machine Theory*, 30(6), 1995.

[RB96] E. Rimon and J. Burdick. On force and form closure for multiple finger grasps. In *Proc. of the IEEE Intl. Conf. on Robotics and Automation, Minneapolis, Minnesota*, April 1996.

[RB98a] E. Rimon and J. Burdick. Mobility of bodies in contact–I: A 2nd order mobility index for multiple-finger grasps. *IEEE Transactions on Robotics and Automation*, 14(5), 1998.

[RB98b] E. Rimon and J. Burdick. Mobility of bodies in contact–II: How forces are generated by curvature effects. *IEEE Transactions on Robotics and Automation*, 14(5), 1998.

[RSL+02] Gabriel Recatalà, Michael Sorg, Jan Leupold, Pedro J. Sanz, and Àngel P. del Pobil. Visual grasp determination and tracking in 2D dynamic scenarios. In *Proc. of the IEEE/RSJ Intl. Conf. on Intelligent Robots and Systems, Lausanne, Swiss*, October 2002.

[Sal03] Image of the Salisbury Hand. http://www-robotics.cs.umass.edu/ /images/robots/salisbury.jpg, 2003.

[SB98] Thomas Schlegl and Martin Buss. Hybrid closed-loop control of robotic hand regrasping. In *Proc. of the IEEE Intl. Conf. on Robotics and Automation, Leuven, Belgium*, pages 3026–3031, May 1998.

[Sch01] Thomas Schlegl. *Diskret-kontinuierliche Regelung mehrfingriger Roboterhände zur robusten Manipulation von Objekten*. PhD thesis, Fakultät für Elektro- und Informationstechnik, TU München, 2001.

[SHB+99] Thomas Schlegl, Steffen Haidacher, Martin Buss, Franz Freyberger, Friedrich Pfeiffer, and Günther Schmidt. Compensation of discrete contact state errors in regrasping experiments with the TUM-hand. In *Proc. of the IEEE/RSJ Intl. Conf. on Intelligent Robots and Systems, Kyongju, Korea*, pages 118 – 123, Oktober 1999.

[She02] C. K. Shene. Introduction to computation with geometry notes. http://www.cs.mtu.edu/ ˜shene/COURSES/cs3621/NOTES/ /notes.html, 2002.

[Shi96] K. B. Shimoga. Robot grasp synthesis: A survey. *Intl. Journal of Robotics Research*, 15(3):230–266, June 1996.

[SM92a] Fridtjof Stein and Gérard Medioni. Structural indexing: Efficient 2-D object recognition. *IEEE Transactions on Pattern Analysis and Machine Intelligence*, 14(12), 1992.

[SM92b] Fridtjof Stein and Gérard Medioni. Structural indexing: Efficient 3-D object recognition. *IEEE Transactions on Pattern Analysis and Machine Intelligence*, 14(2), 1992.

[SPB01a] S. Schulz, Ch. Pylatiuk, and G. Bretthauer. A new ultralight anthropomorphic hand. In *Proc. IEEE Conf. on Robotics and Automation*, pages 2437–2441, Seoul, Corea, May 2001.

[SPB01b] Stefan Schulz, Christian Pylatiuk, and Georg Bretthauer. Druckluft in den Fingern. *Spektrum der Wissenschaft*, (5):60 – 66, May 2001.

[Str80] Gilbert Strang. *Linear Algebra and Its Applications*. Academic Press, Inc., London, 2 edition, 1980.

[SUK99] M. M. Svinin, K. Ueda, and M. Kaneko. Analytical conditions for the rotational stability of an object in multifinger grasping. In *Proc. of the IEEE Intl. Conf. on Robotics and Automation, Detroit, Michigan*, pages 257 – 262, May 1999.

[Sup02] Michael Suppa. Miniaturisierter Laserscanner für Robotikanwendungen. *Mechatronik-News, Informationen des Bayrischen Kompetenznetzwerkes fuer Mechatronik*, (1), 2002.

[SW01] Ferdinand Schmoeckel and Heinz Wörn. Remotely controllable mobile microrobots acting as nano positioners and intelligent tweezers in scanning electron microscopes (sems). In *Proc. of the IEEE Intl. Conf. on Robotics and Automation, Seoul, Korea*, pages 3909–3913, May 2001.

[TFS94] J. Trinkle, A. Farahat, and P. Stiller. Second-order stability cells of frictionless rigid-body systems. In *Proc. of the IEEE Intl. Conf. on Robotics and Automation, San Diego, California*, May 1994.

[TFS95] J. Trinkle, A. Farahat, and P. Stiller. First-order stability cells of active multirigid -body systems. *IEEE Transactions on Robotics and Automation*, 11(4), 1995.

[Wim02] Thomas Wimböck. Bestimmung von Kontaktpunkten zwischen einer mehrfingrigen Roboterhand und Objekten unbekannter Geometrie mittels redundanter Sensordaten. Bachelor thesis, Institut für Robotik und Mechatronik, Deutsches Zentrum für Luft- und Raumfahrt, 2002.

[Woe95] Kurt Woelfl. *Planung von Manipulationsvorgängen einer Roboterhand*. PhD thesis, Fakultät für Mechanik, TU München, 1995.

[XK99] Nicholas Xydas and Imin Kao. Modeling of contact mechanics and friction limit surfaces for soft fingers in robotics, with experimental results. *Intl. Journal of Robotics Research*, 18(8), 1999.

[YN90] T. Yoshikawa and K. Nagai. Analysis of multi-fingered grasping and manipulation. In S. Venkataraman and T. Iberall, editors, *Dextrous Robot Manipulation*, chapter 9. Springer-Verlag, 1990.

[Yos90] Tsuneo Yoshikawa. *Foundation of Robotics: Analysis and Control*. The MIT Press, Cambridge, MA, 1990.

[ZMT96] Hong Zhang, Hitoshi Maekawa, and Kazuo Tanie. Sensitivity analysis and experiments of curvature estimation based on rolling contact. In *Proc. of the IEEE Intl. Conf. on Robotics and Automation, Minneapolis, Minnesota*, pages 3514 – 3519, April 1996.

[ZS+00] Denis Zorin, Peter Schröder, et al. Subdivision for modeling and animation. New York University, 2000. SIGGRAPH 2000 Tutorial Proceedings.